VYSOKÉ UČENÍ TECHNICKÉ V BRNĚ

FAKULTA STROJNÍHO INŽENÝRSTVÍ
ÚSTAV MATERIÁLOVÝCH VĚD A INŽENÝRSTVÍ

POKROČILÉ SLINOVACÍ TECHNIKY

HABILITAČNÍ PRÁCE

Ing. VÁCLAV POUCHLÝ, PhD., Ing.Paed.IGIP

BRNO 2022

Obsah

1. Úvod 6
2. Stav současného poznání 8
   2.1. Slinovací proces 8
   2.2. Slinovací modely 9
   2.3. Modely růstu zrn 14
   2.4. Pokročilé slinovací techniky 15
3. Cíle práce 21
4. Experimentální část 22
   4.1. Použité materiály 22
   4.2. Úprava prášků 23
   4.3. Tvarování 23
   4.4. Slinování 24
   4.5. Výpočet aktivační energie slinovacího procesu 26
   4.6. Výpočet aktivační energie růstu zrn 26
   4.7. Analytické metody 25
5. Výsledky a diskuze 27
   5.1. Ovlivnění slinovacího chování pomocí dopantů 27
   5.2. Dlouhodobé slinování na nižších teplotách 33
   5.3. Slinování vysokou rychlostí ohřevu 37
   5.4. Vliv fyzikální aktivace povrchu částic na slinovací chování 40
   5.5. Slinovací chování vrstevnatých kompozitů 44
6. Závěry 47
7. Seznam použité literatury 49

Vybrané práce autora zařazené do souboru práce:

1. **POUCHLÝ, V.,** MACA, K., SHEN, Z. Two-stage master sintering curve applied to two-step sintering of oxide ceramics, *J.Eur.Ceram.Soc.*, 2013, vol. 33, 2275-2283, 39 citací.
2. MACA, K., **POUCHLÝ, V.,** BODIŠOVÁ, K., ŠVANČÁREK, P., GALUSEK, D. Densification of fine-grained alumina ceramics doped by magnesia, yttria and zirconia evaluated by two different sintering models, *J.Eur.Ceram.Soc.*, 2014, vol. 34, 4363-4372, 29 citací.
3. **POUCHLÝ, V.,** MACA, K., Sintering kinetic window for yttria-stabilized cubic zirconia, *J. Eur. Ceram. Soc.*, 2016, vol. 36, 2931-2936, 14 citací.
4. MACA, K., **POUCHLÝ, V.,** DRDLÍK, D., HADRABA, H., CHLUP, Z. Dilatometric study of anisotropic sintering of alumina/zirconia laminates with controlled fracture behaviour, *J. Eur. Ceram. Soc.*, 2017, vol. 37, 4287-4295, 15 citací.
5. **POUCHLÝ, V.,** RAHEĽ, J., SPUSTA, T., ILČÍKOVÁ, M., PAVLIŇÁK, D., MORÁVEK, T., MACA, K., Improved micrtostructure of alumina ceramics prepared form DBD plasma activated powders, *J. Eur. Ceram. Soc.*, 2019, vol. 39, 1297-1303, 5 citací.

Abstrakt

Předkládaná habilitační práce obsahuje ucelený přehled pokroku ve výzkumu pokročilých slinovacích technik, demonstrovaném na slinovacím chování modelových materiálů oxidových keramik Al_2O_3 a Y_2O_3 stabilizovaného ZrO_2 v období 2013-2022. V práci je taktéž uveden rozvoj experimentálních technik v tomto období, obzvláště posun ve vysokoteplotní dilatometrii a z ní odvozených výpočtových modelů využívajících data získaná z vysokoteplotní dilatometrie, jako je např. model Master Sintering Curve a jeho modifikace používané pro porovnání účinnosti jednotlivých slinovacích technik. Experimentální část práce je zaměřena na pět současných směrů pokročilých slinovacích technik: slinování za přítomnosti dopantů, slinování při nízkých teplotách, slinování vysokými rychlostmi ohřevu, slinování částic se změněnou povrchovou energií a slinování vrstevnatých keramických kompozitů.

Abstract

The presented habilitation thesis contains a comprehensive overview of the progress in the field of advanced sintering techniques in the period from 2013 to 2022 year. The advancement of these techniques is demonstrated on the sintering behaviour of two oxide ceramics: Al_2O_3 and yttria stabilized ZrO_2. The thesis also presents the development of experimental techniques in this period, with a special attention to a high-temperature dilatometry and derived computational models using data obtained from high-temperature dilatometry, such as the Master Sintering Curve model and its modifications. The experimental part of the work is focused on five contemporary directions of advanced sintering techniques: sintering at a presence of dopants, sintering at a low temperatures, sintering by high heating rates, sintering of particles with modified surface energy, constrained sintering and sintering in the presence of dopants.

Předmluva

Předkládaná habilitační práce je ucelený soubor mých pěti vybraných vědeckých prací týkajících se pokročilých slinovacích technik. Cílem tohoto souboru je popis jednotlivých slinovacích strategií, jejich vývoj mezi lety 2013-2022 a jejich porovnání s konvenční slinovací strategií.

K tématu slinování keramických materiálů jsem se poprvé dostal před 15 lety, kdy jsem se při studiu oboru Materiálové inženýrství stal technickým pracovníkem Odboru keramiky a polymerů na Ústavu materiálových věd a inženýrství. Multidisciplinární materiálové inženýrství spojuje znalosti různých oborů: chemie, fyziky pevných látek, strojírenské technologie, atd. Právě toto multidisciplinární spojení vědních oborů mi umožnilo naplno se věnovat předloženému tématu. O zvolení správného směru a významnosti tohoto výzkumu svědčí zvolení článku [1], jehož jsem spoluautorem, v roce 2014 excelentním výsledkem dle pilíře II RIV v té době platné metodiky.

Uvedené experimentální výsledky vznikly převážně na půdě Vysokého učení technického v Brně a to v prostorách Fakulty strojního inženýrství (Odboru keramiky a polymerů Ústavu materiálových věd a inženýrství) a od roku 2016 i CEITECu (Inovační technologie v keramice). Velká část práce mohla být také uskutečněna díky spolupráci s jinými zahraničními pracovišti. Převážně se jedná o pracoviště ve Švédsku (prof. James Shen, Stockholm University, Stockholm), Slovinsku (dr. Andraž Kocjan, Jozef Stefan Institute, Ljubljana) a Slovensku (prof. Dušan Galusek, FunGlass Centre of Excellence, Trenčín). Na části práce se také podíleli studenti VUT (řešitelé bakalářských a diplomových prací pod mým vedením), kterým bych chtěl touto cestou rovněž poděkovat.

Experimentální část práce byla vytvořena zejména díky finanční podpoře následujících vědecko-výzkumných projektů:

- Efekt elektro-magnetického pole na slinování pokročilých keramických materiálů, GAČR, 13-08717P, hlavní řešitel: Ing. Václav Pouchlý, Ph.D.
- Využití teoretických a experimentálních přístupů ke slinování pro získání optimální mikrostruktury a vlastností pokročilých keramických materiálů, GAČR, 15-06390S, hlavní řešitel: prof. RNDr. Karel Maca, Dr.

- Fyzikální aktivace povrchu keramických částic jako nástroj pro zlepšení vlastností jemnozrnné pokročilé keramiky, GAČR, 17-05620S, hlavní řešitel: prof. RNDr. Karel Maca, Dr.
- Posilnenie cezhraničného vzdelávacieho potenciálu v oblastiach inovatívnych technológií výroby a charakterizácie sklených a keramických materiálov, Ministerstvo hospodárstva Slovenskej Republiky, 304011U702, hlavní přeshraniční řešitel: Ing. Václav Pouchlý, Ph.D. Ing.Paed.IGIP
- Vývoj funkčních keramických a sklokeramických materiálů ve spolupráci s Centrem excelence FunGlass, MŠMT, LTT18013, hlavní řešitel: prof. RNDr. Karel Maca, Dr.
- Optimalizace mikrostruktury keramických materiálů a kompozitů pro zlepšení jejich mechanických a funkčních vlastností, Fakulta strojního inženýrství VUT, FSI-S-20-6292, hlavní řešitel: prof. RNDr. Karel Maca, Dr.

1. Úvod

Jedním z nejvýznamnějších a nejstarších materiálů vyráběných člověkem je keramika. Keramické materiály jsou z chemického hlediska sloučeniny typu oxidů, karbidů, nitridů, boridů, apod. Tyto materiály se vyznačují silnou kovalentní a iontovou meziatomovou vazbou, přičemž jde většinou o kombinaci těchto vazeb. Díky této vazbě patří k typickým vlastnostem keramických materiálů vysoká pevnost v tlaku, tvrdost, chemická odolnost, odolnost vůči korozi, vysokým teplotám a opotřebení. Na druhou stranu mají tyto materiály také charakteristické nevýhody, např. omezenou možnost plastické deformace a díky tomu nízkou lomovou houževnatost a vysokou křehkost. Díky tomu jsou vlastnosti keramických materiálů velmi citlivé na strukturní defekty. Tato skutečnost má za následek nutnost precizně zvládnout všechny technologické kroky potřebné k přípravě keramických materiálů.

Mezi nejdůležitější technologické kroky přípravy keramických materiálů patří slinování, kdy dochází k přeměně pórovitého polotovaru do finálního (nejčastěji hutného) výrobku s jeho charakteristickými vlastnostmi. Správné zvládnutí kontroly celého slinovacího procesu je klíčové k dosažení bezdefektního (většinou neporézního) výsledného produktu s požadovanou mikrostrukturou a vlastnostmi. I když je slinování velice důležitý technologický krok, nemůže samotné slinování odstranit defekty vzniklé díky předchozím technologickým krokům (výroba a úprava prášků, tvarování, atd.). Kvůli nezbytnosti a důležitosti slinovacího kroku je však potřeba tento technologický krok umět dobře popsat a kontrolovat, a také sledovat nové slinovací trendy. Komplexní popis slinovacího děje je ovšem velice složité z důvodu vysokého počtu interagujících členů. Z tohoto důvodu se práce zabývá nejenom vývojem slinovacích trendů, ale i rozvojem analytických a modelových metod určených k popisu slinování.

V posledních letech se stále objevují nové slinovací techniky, které mají zabezpečit dosažení lepší mikrostruktury výsledného tělesa, nebo vyrobení porovnatelného produktu za podstatně kratší čas pomocí změny teplotního režimu. Precizní zvládnutí, a tedy kontrola nad dosaženou mikrostrukturou, je nutná především ve špičkových technologiích nezbytných např. pro optické [2], piezoelektrické [3], multiferoické [4] a jiné pokročilé keramické materiály.

Jednou z možností, jak ovlivnit výslednou mikrostrukturu keramických materiálů, je využití dopování. Dopování keramických materiálů umožňuje změnit slinovací cyklus např. snížením slinovací teploty, nebo vyplněním pórů nízko tavitelnou složkou (slinování za přítomnosti kapalné fáze). Pomocí dopování lze ale připravit i materiály s vylepšenými původními vlastnostmi, jako jsou např. mechanické [5] či elektromagnetické [6, 7] vlastnosti, ale i novými,

jako je např. luminiscence [8]. Moderním směrem vývoje keramických materiálů je příprava materiálů s kombinací více vlastností jako jsou např. optoelektrické materiály [9].

Další možností, jak dosáhnout zlepšených výsledných vlastností, je modifikace teplotního cyklu slinovacího procesu. Obecně se objevují dvě základní teorie, kdy jednou z možností je pomalé slinování při nízkých teplotách, aby se zabránilo růstu zrn. Druhá možnost spočívá v rychlém slinování, které má velký význam pro průmysl, a to obzvláště kvůli ušetření elektrické energie díky minimalizaci tepelných ztrát [10], zrychlení a zefektivnění výroby a služeb pro zákazníka (např. u bio keramiky) [11] apod.

Další možností, jak ovlivnit slinovací chování a tedy i výslednou mikrostrukturu pokročilých keramických materiálů, je změna kvality povrchu (a tedy i povrchové energie) částic. Této změny lze dosáhnout několika způsoby. Nejjednodušší, a tedy nejrozšířenější, je aktivace povrchu částic za pomocí mletí, kdy dochází k vytváření nových volných povrchů, které mohou vstupovat do chemických reakcí. Při této aktivaci povrchu ovšem dochází zároveň ke zmenšování velikosti částic. Není tedy jednoduché od sebe separovat a posoudit vliv snížené velikosti částic a vliv aktivovaného povrchu. Z tohoto důvodu bylo v rámci této práce rozhodnuto použít aktivování povrchu částic pomocí moderní nízkoteplotní plazmové technologie, která nemění velikost částic, ale pouze ovlivňuje její povrch pomocí vázání funkčních skupin [12].

Jedním z rozvíjejících se odvětví slinování je slinování kompozitních keramických materiálů. Keramické kompozity se využívají nejčastěji pro konstrukční keramiku, kde spojením dvou různých materiálů dochází ke vzniku vnitřního napětí [13], což může vést k odklonům trhliny [14]. Díky tomu dochází k navýšení výsledných mechanických vlastností (obzvláště lomové houževnatosti), ale někdy i k dosažení výjimečných elektrických, magnetických, tepelně izolačních a jiných vlastnosti [15, 16]. Pokročilé slinovací techniky a propracované slinovací modely umožňují řídit vznikající vnitřní napětí a dosahovat zvýšených užitných vlastností výsledného keramického tělesa.

Všemi uvedenými pokročilými slinovacími technikami se budou podrobněji zabývat následující kapitoly. Navíc, pro možnost porovnání jednotlivých slinovacích technik, je v práci kladen důraz na popis a aplikaci kinetických modelů pro porovnání jednotlivých slinovacích technik.

2. Stav současného poznání

Následující kapitola se ve zkratce věnuje slinovacímu procesu pokročilých keramických materiálů, jako důležitou součástí keramické technologie. Tato kapitola také zahrnuje výčet kinetických slinovacích modelů, které jsou důležité pro posouzení přínosu některých pokročilých slinovacích technik.

2.1. Slinovací proces

Slinování je technologický proces, při kterém se z původního pórovitého práškovitého polotovaru stává aplikací tepelné energie hutné těleso [17]. Při slinování dochází k aktivaci difuzních dějů, s cílem minimalizovat energii porézního systému. Ke snížení celkové energie tělesa může přispět jak změna povrchové energie (přechodem z energeticky nevýhodného rozhraní pevná fáze – plynná fáze do energeticky výhodnějšího rozhraní pevná fáze – pevná fáze), tak i změna celkového povrchu (zhrubnutí částic nebo zrn [18]). V průběhu slinování tedy dochází ke změně velikosti a tvaru pórů a částic (zrn), což je spojeno se změnou délkových rozměrů – smrštěním materiálu.

2.1.1. Vysokoteplotní dilatometrie

Vysokoteplotní dilatometrie umožňuje měřit délkové změny materiálu a tím pádem i smrštění způsobené slinovacím procesem. Díky in-situ záznamu smrštění (a jeho závislosti na čase a teplotě) je vysokoteplotní dilatometrie používaná jako základní nástroj pro posouzení jednotlivých slinovacích technik a zároveň dilatometrická měření vstupují do většiny výpočetních kinetických modelů slinování.

Při přípravě keramických materiálů různými technologiemi často dochází ke stavu, kdy mají keramické polotovary (green bodies) různou počáteční hustotu a tedy i různý průběh smrštění, i když díky slinování dosáhnou stejné (ideálně 100 %) konečné relativní hustoty. Samotné smrštění materiálu je silně závislé na metodě přípravy materiálu [1, 12, 19-21] a přítomnosti dopantů [22]. Aby se smršťovací křivky takto různě připravených polotovarů daly porovnávat, je výhodné přepočítat smrštění na zhutňovací křivky (viz Obr. 1). Pro přepočet lze využít následující vztah [23]:

$$\rho(t,T) = \rho_{final} \frac{(100+\varepsilon_{Tmax})^3}{\left(100+\varepsilon(t,T)-CTE(T-T_0)\right)^3} \ , \qquad (1)$$

kde: ρ je aktuální relativní hustota vzorku, T je teplota, ρ_{final} je hustota vzorku dosažená po ukončení slinovacího procesu stanovená metodou dvojího vážení, ε_{Tmax} je smrštění při dosažení ρ_{final}, $\varepsilon(t,T)$ je smrštění změřené dilatometrem, CTE je koeficient teplotní roztažnosti (změřitelný ze smrštění vzorku během chlazení) a t je čas.

Vzorec (1) však platí pouze pro izotropní smrštění. Při neizotropním smrštění je vzorec doplněn o koeficienty anizotropie K_1 a K_2 [23].

$$\rho(t,T) = \rho_f \cdot \frac{(100+\varepsilon_{Tmax})\cdot(100+\varepsilon_{Tmax}\cdot K_1)\cdot(100+\varepsilon_{Tmax}\cdot K_2)}{(100+\varepsilon_{techn}(t,T))\cdot(100+\varepsilon_{techn}(t,T)\cdot K_1)\cdot(100+\varepsilon_{techn}(t,T)\cdot K_2)}. \quad (2)$$

Obr. 1 ukazuje příklad přepočtu smršťovací křivky na křivku zhutnění podle rovnice (1).

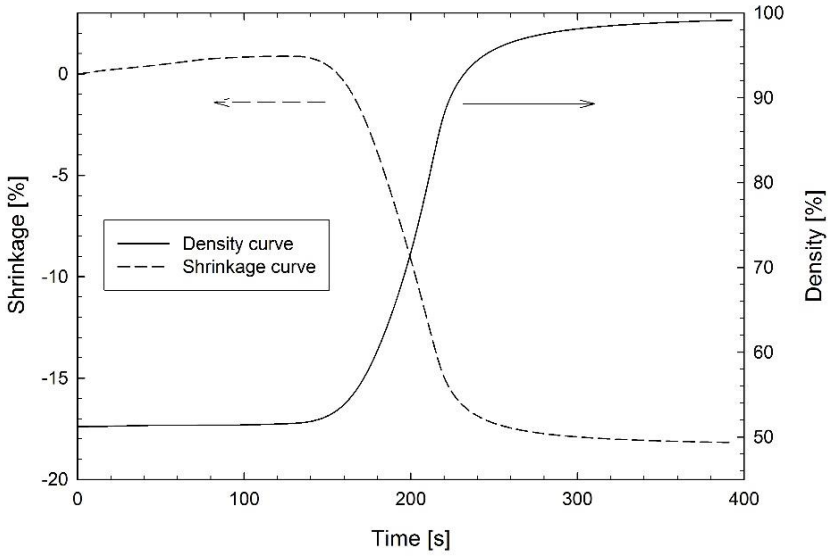

Obr. 1: Výsledek přepočtu křivky smrštění na zhutňovací křivku pro Al_2O_3 [23].

2.2. Slinovací modely

V průběhu slinování dochází k přesunu hmoty v tuhé fázi. Nejčastějším mechanismem přenosu hmoty v tuhé fázi je difuze. Při slinování může ale také dojít k viskóznímu toku, který je častý u slinování s přítomností tekuté fáze či při vysokém tlaku [10]. Dále se při slinování může objevit přenos hmoty založený na vypařování-kondenzaci, ten ale nevyužívá přesun hmoty tuhou fázi, ale využívá přesunu hmotu přes plynnou fázi. Díky tomu je tento děj častý u slinování s přítomností tekuté fáze, slinování iontových keramik [24], nebo v případě nízké volatility prvků (např. slinování pokročilých keramik na bázi $KNaNbO_3$ [25]). Pro zjednodušení se ale často u výpočtových modelů viskózní tok a vypařování/kondenzace zanedbává a počítá se pouze s difuzními pochody [26].

Při slinování se uplatňuje několik druhů difuze a to převážně objemová difuze, difuze mřížkou a pro slinování nejdůležitější difuze po hranicích zrn [27].
Jelikož difuze je tepelně aktivovaný děj, lze na něj aplikovat Arrheniovu rovnici, kde vystupuje aktivační energie daného děje E_A:

$$D = D_0 e^{\frac{-E_A}{RT}}, \tag{3}$$

kde: D je difuzní koeficient, D_0 je pre-exponenciální člen, R je plynová konstanta.
Většina výpočtových modelů založených na datech z vysokoteplotní dilatometrie spočívá v nalezení aktivační energie slinovacího procesu, E_A. Aktivační energii slinování můžeme chápat jako potenciálovou (energetickou) bariéru, kterou je nutné překonat pro uskutečnění daného děje (např. slinování) [28].

2.2.1. Kinetický model výpočtu aktivační energie slinovacího procesu dle Wanga a Raje

Wang a Raj v roce 1990 zformulovali výpočet aktivační energie slinování dle kinetického slinovacího modelu vycházejícího z rovnice pro změnu hustoty v závislosti na čase [29]:

$$\frac{d\rho}{dt} = \mathrm{A}\frac{e^{-E_A/RT}}{T}\frac{f(\rho)}{G^n}, \tag{4}$$

kde:

$$A = \frac{C\gamma V^{\frac{2}{3}}}{R}, \tag{5}$$

kde: C je konstanta závislá na druhu difuze [29], γ je povrchová energie, V je molární objem, G je střední velikost zrn a $f(\rho)$ je funkce hustoty.

Pokud popíšeme vývoj hustoty jako:

$$\frac{d\rho}{dt} = \frac{d\rho}{dT}\frac{dT}{dt}, \tag{6}$$

lze kombinací rovnic (4) a (6) obdržet následující výraz:

$$\ln\left(T\frac{d\rho}{dT}\frac{dT}{dt}\right) = -\frac{E_A}{RT} + \ln\big(f(\rho)\big) + lnA - nlnG. \tag{7}$$

V krátkém časovém úseku lze předpokládat, že ρ a G je konstantní, je tedy možné rovnici 7 zjednodušit na tvar přímky a upravit ji pro výpočet E_A. Podmínka nulového růstu zrn (G = konst.) znamená, že tento model nemůže být aplikován ve finální slinovací části, kde

nastává intenzivní růst zrn. Model umožňuje výpočet aktivační energie slinování vždy v určité hustotě (ρ = konst.) které bylo dosaženo při různých rychlostech slinování *dT/dt*. Je samozřejmě možné tento výpočet provést pro různé hustoty, ale čím více se model blíží finální fázi slinování (kde se projevuje růst zrn) tím dává tento model zkreslenější výsledky [30].

Pro praktický výpočet se jednotlivé vzorky slinou různou rychlou rychlostí ohřevu (např. 2, 5, 10 a 20 °C/min). Poté se pro danou ρ a předpoklad G=0 vyjádří levá strana rovnice (7) v závislosti na 1/T, které bylo dosaženo pro jednotlivé vzorky. Výsledné body se poté proloží přímkou, kde směrnice této přímky je úměrná (konstanta úměrnosti je *1/R*) aktivační energii slinování E_A. Příkladem takto vypočtené aktivační energie slinování pro různé materiály při 70 % relativní hustotě uvádí Obr. 2.

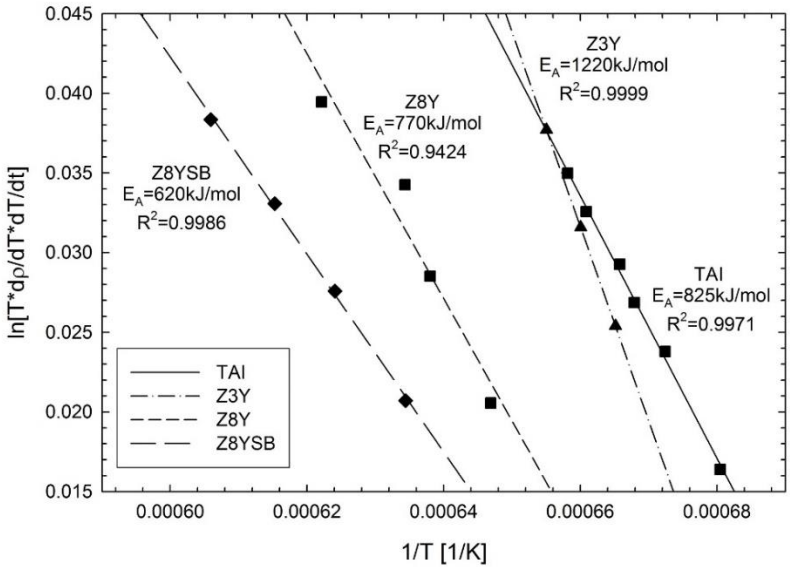

Obr. 2: Vypočtené aktivační energie slinování pro materiály Al_2O_3 (TAI, velikost částic 100 nm), tetragonální ZrO_2 (Z3Y, velikost částic 60 nm) a kubický ZrO_2 (Z8Y s velikostí částic 70nm a Z8YSB s velikostí částic 140 nm) při 70% relativní hustotě (R^2 v popisu grafu je korelační koeficient) [31].

2.2.2. Univerzální slinovací křivka (MSC - Master Sintering Curve)

Slinovací model Master Sintering Curve (MSC) byl vytvořen z kombinovaného slinovacího modelu [27], který zahrnuje dva různé difuzní mechanismy: objemovou difuzi a difuzi po hranicích zrn, viz rovnice 8:

$$-\frac{dL}{Ldt} = \frac{\gamma\Omega}{kT}\left(\frac{\Gamma_v D_v}{G^3} + \frac{\Gamma_b \delta D_b}{G^4}\right), \tag{8}$$

kde: Ω je atomový objem, k je Boltzmannova konstanta, L je délka vzorku, D_v je koeficient objemové difuze, D_b je koeficient difuze po hranicích zrn, δ je šířka hranice zrn a Γ reprezentuje geometrický faktor, tj. hnací sílu slinování [32, 33].

V rovnici (8) je několik proměnných, jejichž skutečnou hodnotu je těžké experimentálně naměřit [32]. Rovnici (8) je ovšem možno zjednodušit při splnění dvou podmínek. První podmínka uvažuje, že jeden z difuzních procesů dominuje celému slinovacímu procesu (ať už objemová difuze, či difuze po hranicích zrn). Tato podmínka je pravděpodobně splněna pro materiály s vysokým poměrem povrch/objem částic, kde převládá difuze po hranicích zrn, což jsou typicky keramické prášky s velikostí částic pod 1 μm [18]. Druhá podmínka je splněna, když vývoj mikrostruktury (popsaný G a Γ) je funkcí pouze hustoty (nezávisle na tepelné historii). Pokud jsou obě podmínky platné, lze rovnici (8) přepsat jako rovnici (9), v níž levá strana je funkcí pouze hustoty a pravá představuje teplotní historii vzorku s parametrem E_A:

$$\frac{k}{\gamma\Omega\delta D_0}\int_{\rho_0}^{\rho}\frac{(G(\rho))^n}{3\rho\Gamma(\rho)}d\rho = \int_0^t \frac{1}{T}exp\left(-\frac{E_A}{RT}\right)dt, \qquad (9)$$

kde: n je parametr, který nabývá hodnotu 3 (pro objemovou difuzi), nebo 4 (pro difuzi na hranicích zrn).

V rovnici (9) je levá strana rovnice funkcí pouze hustoty, a pravá strana vyjadřuje tepelnou historii vzorku. Vztah mezi hustotou ρ a pravou stranou rovnice (9) (označovanou jako Θ) je nazýván univerzální slinovací křivkou (MSC - Master Sintering Curve). MSC je unikátní pro každý keramický prášek připravený danou technologií [32].

Pro praktickou konstrukci MSC je potřeba provést několik dilatometrických měření s různou teplotní historií (typicky různou rychlostí ohřevu). Pokud je koncept MSC správný, existuje pouze jedna (správná) hodnota aktivační energie slinování E_A, pro kterou se všechny teplotní profily $\rho=f(\Theta)$ překrývají a tvoří tak jedinou „Master“ křivku. Výpočet modelu MSC se tedy skládá z opakované numerické integrace pravé strany rovnice (9) pro všechny teplotní profily při odhadnuté E_A. Odhad E_A se mění podle toho, jestli se k sobě jednotlivé funkce $\rho = f(\Theta)$ pro zvolené E_A přibližují, či vzdalují (viz Obr. 3). Výsledné E_A je poté zvoleno dle nejnižší vzdálenosti mezi jednotlivými křivkami $\rho = f(\Theta)$. Pro posouzení vzdálenosti mezi jednotlivými $\rho=f(\Theta)$ křivkami se nejčastěji používají dvě kritéria: střední kolmá vzdálenost mezi křivkami (Mean Perpendicular Curve Distance – MPCD, která byla vyvinuta na pracovišti OKP ÚMVI

FSI, aby dobře vyhovovala sigmoidálnímu tvaru Master křivek) [34] a metoda nejmenších čtverců (Mean Residual Squares - MRS).

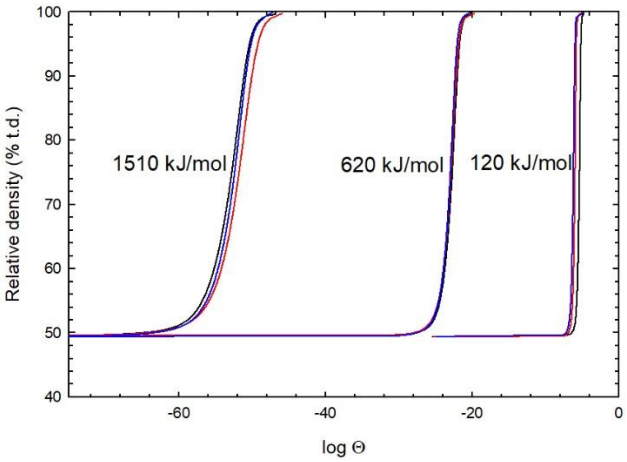

Obr. 3: Schéma odklonu jednotlivých křivek $\rho=f(\Theta)$ podle odhadnuté E_A.

2.2.3. Master Shrinkage Curve

Jednou z podmínek teorie MSC je předpoklad izotropního smrštění, umožňující převod relativního smrštění (ε) na hustotu (ρ) [34]. Pro některé nehomogenně slinující materiály, jako jsou např. kompozitní vrstevnaté materiály, ovšem nelze tento předpoklad splnit. Z tohoto důvodu byla na OKP ÚMVI FSI zformulována teorie Master Shrinkage Curve, která místo objemového zhutnění využívá slinovacího smrštění pouze v jednom vybraném směru [35]. Pomocí modelu Master Shrinkage Curve tedy lze vypočítat aktivační energii slinování v jednotlivých směrech samostatně. Pokud by materiál slinoval izotropně, naměřená aktivační energie slinování by byla ve všech směrech stejná.

Rovnice Master Shrinkage Curve vychází ze stejných předpokladů, jako MSC, ale neuvažuje přepočet smrštění na hustotu [32, 35]. Lze tedy obdobně jako pro MSC odvodit z rovnice 8 rovnici 10:

$$-\frac{k}{\gamma\Omega\delta D_0}\int_0^{\varepsilon_f}\frac{\left(G(\varepsilon)\right)^n}{\Gamma(\varepsilon)}d\varepsilon=\theta=\int_0^t\frac{1}{T}\exp\left(-\frac{E_A}{RT}\right)dt. \qquad (10)$$

Výpočet E_A funguje stejně, jako u základního modelu MSC pomocí dosazování jednotlivých E_A a hledání nejlepšího překryvu. Díky využití relativního smrštění v různých směrech je umožněno vypočítat např. smrštění core-shell kompozitu [36], nebo posoudit jak jednotlivé vrstvy v lamelárním kompozitu ovlivňují slinovací chování celku [35].

2.3. Modely růstu zrn

2.3.1. Kinetický model růstu zrn dle M. Mayo

Obdobně jako je pro slinovací děj definovaná aktivační energie slinovacího procesu E_A, lze definovat i aktivační energii růstu zrn E_{GG} jako energii nutnou pro uskutečnění růstu zrn. Růst zrn v keramických materiálech lze popsat následující rovnicí:

$$G^m - G_0^m = K_0 t \, exp\left(-\frac{E_{GG}}{RT}\right), \tag{11}$$

kde G je průměrná velikost zrn, G_0 je původní velikost zrn, m je exponent růstu zrn nabývající typicky hodnoty mezi 2 a 4 [17], a K_0 je pre-exponenciální faktor. Pro výpočet aktivační energie růstu zrn z rovnice (11) je potřeba provést experimenty při několika různých teplotách T, při níž je aplikováno několik různě dlouhých prodlev. Rovnice (11) je pak převedena do tvaru přímky:

$$G^m = k_0 exp\left(\frac{-\mathrm{E}_{GG}}{RT}\right) t + G_0^m, \tag{12}$$

kde $k_0 exp\left(\frac{-\mathrm{E}_{GG}}{RT}\right)$ je konstanta. Poté je potřeba za n dosadit přirozené číslo od 2 do 4 a pomocí metody nejmenších čtverců zjistit, který zvolený koeficient vykazuje nejmenší chybovost. Tímto postupem zjistíme G_0^m. V následujícím kroku zlogaritmujeme rovnici (12) a opět ji převedeme do tvaru přímky, kde její směrnice udává velikost aktivační energie růstu zrn:

$$\ln\big((G^m - G_0^m) - t\big) \cdot \mathrm{R} = -\frac{E_{GG}}{T} + \ln k_0 R. \tag{13}$$

k_0 lze poté získat dosazením do původní rovnice (11).

2.3.2. Master Grain Growth Curve

Původní koncept MSC vychází z Arrheniova vztahu pro difuzi (rovnice 3). Jelikož se jedná o obecnou rovnici pro tepelně aplikované procesy, lze podobnou konstrukci, jako je MSC, použít i pro jiné tepelně aktivované děje [37]. Jeden z příkladů využití konceptu MSC pro jiný tepelně aktivovaný proces důležitý pro technologii přípravy keramických materiálů koncept Master Grain Growth Curve (MGGC [38]) aplikovaný na růst zrn. Výsledná velikost zrn v materiálu totiž významně ovlivňuje finální mechanické, elektrické a jiné užitné vlastnosti [6]. Obdobně, jako u MSC vycházející z rovnice 9 je E_{GG} nalezena, když všechny vzorky s hodnotami ρ, G padnou do jediné master křivky vytvořené rovnicí 14:

$$f(G) = \int_0^t exp\left(-\frac{E_{gg}}{RT}\right) dt \equiv \Theta_{gg}, \quad (14)$$

kde: Θ_{gg}je označení funkce Master Grain Growth Curve.

2.4. Pokročilé slinovací techniky

V posledních letech se díky zrychlujícímu se rozvoji experimentálních i analytických technik objevují stále častěji nové slinovací techniky, které slibují zjednodušení, zrychlení či optimalizaci slinovacího děje. Těmi nejvýznamnějšími pokročilými slinovacími technikami se budou zabývat následující podkapitoly.

2.4.1. Dopování pokročilých keramických materiálů

Jednou z možností, jak ovlivnit výslednou mikrostrukturu keramických materiálů, je použití dopantů. Obecně není možné dosáhnout absolutní čistoty vstupních surovin, proto studium vlivu dopantů ukazuje i na vliv možných nečistot na slinovací chování. Jedním z nejznámějších příkladů dopování je dopování Al_2O_3 malým množstvím MgO, které zamezí nadměrnému růstu zrn [39]. Pomocí nových výzkumů bylo dokonce zjištěno, že obří zrna v Al_2O_3 (bez příměsi MgO) jsou pravděpodobně způsobena rozpuštěním nečistot (např. SiO_2) na hranicích zrn a tím ovlivňování povrchové energie [40]. Právě dopant MgO umožnil snížit vliv nečistoty SiO_2 na zhoršení mikrostruktury [41].

Dalším známým příkladem dopování je výroba keramik na bázi ZrO_2. Díky fázovým transformacím čistého ZrO_2 (viz Obr. 4) není totiž možné tento materiál připravit konvenční cestou, protože při ochlazování dojde k transformaci tetragonálního ZrO_2 na monoklinické ZrO_2, což je spojeno s nárůstem objemu (o cca 4%), které vede k destrukci materiálu. Z tohoto důvodu se ZrO_2 dopuje Y_2O_3 (nebo i CaO, CeO a jinými oxidy), které posune fázovou transformaci k nižším teplotám [42]. Takovýto materiál se pak dělí na částečně stabilizovaný (tetragonální t-ZrO_2) nebo plně stabilizovaný (kubický c-ZrO_2). U částečně stabilizovaného ZrO_2 dochází při šíření trhliny k dodání dodatečné energie potřebné k transformaci z tetragonálního na monoklinické ZrO_2. Díky zvýšení objemu na ZrO_2 ve špičce trhliny dochází k jejímu uzavírání, což vede k lomové houževnatosti t-ZrO_2 materiálů. Při objevení jevu transformačního zpevnění byl dokonce t-ZrO_2 nazýván termínem „ceramic steel“ [43].

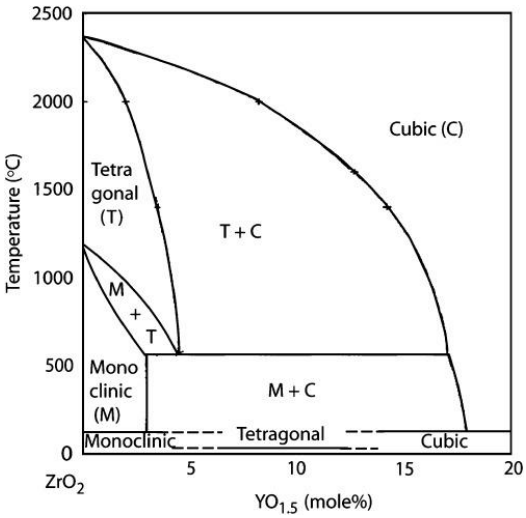

Obr. 4: Část fázového diagramu ZrO_2 – Y_2O_3 [44]

2.4.2. Pomalé slinovací techniky

Pomalé slinovací techniky mají za cíl dosáhnout zlepšené výsledné mikrostruktury oproti konvenčnímu slinování pomocí slinování na nízkých teplotách po dlouhý čas. Tento cíl je obzvláště důležitý pro konstrukční, optické a elektrokeramické materiály. Pomalé slinovací techniky jsou založeny na předpokladu, že aktivační energie slinovacího procesu (E_A) a aktivační energie růstu zrn (E_{GG}) je rozdílná, proto může dojít při nižších teplotách ke zvyšování hustoty bez růstu zrn. Tomuto jevu se také říká kinetické okno slinovacího procesu. Aby toto okno mohlo být „otevřené“, je nutné, aby E_A byla menší, než E_{GG}.

Two step sintering

V roce 2000 I. W. Chen a X. H. Wang uveřejnili v časopise Nature pokročilou slinovací techniku Two Step Sintering (TSS). V této publikaci autoři formulovali předpoklady vzniku tzv. kinetického okna a pro potvrzení této teorie změnou teplotního režimu u Y_2O_3 potlačili růst zrn. Samotná technika TSS se skládá z prvního kroku, kdy materiál je slinut rychlostí např. 5-20 °C/min do stavu 70-90 % teoretické hustoty (dále jen %t.h.), aby došlo k zániku nadkritických pórů, a poté je prudce zchlazen (např. rychlostí 25 °C/min a vyšší) na teplotu o cca 100-200 °C nižší než teplotu dosaženou v prvním kroku. Na této nižší teplotě je vzorek ponechán desítky hodin, kdy dojde k navýšení jeho hustoty (při malém růstu zrn).

V roce 2010 uveřejnili Maca et al. hypotézu, že účinnost TSS se mění v závislosti na symetrii krystalové struktury (viz Obr. 5). Čím vyšší je symetrie krystalické mřížky (např. pro c-ZrO_2), tím je obecně jednodušší pro zrna růst, a proto je potlačení růstu zrn technikou TSS mnohem

a) b)

markantnější než pro materiály s nižší symetrií, které nevykazují velký růst zrn ani při konvenčním slinování (např. t-ZrO_2) [1].

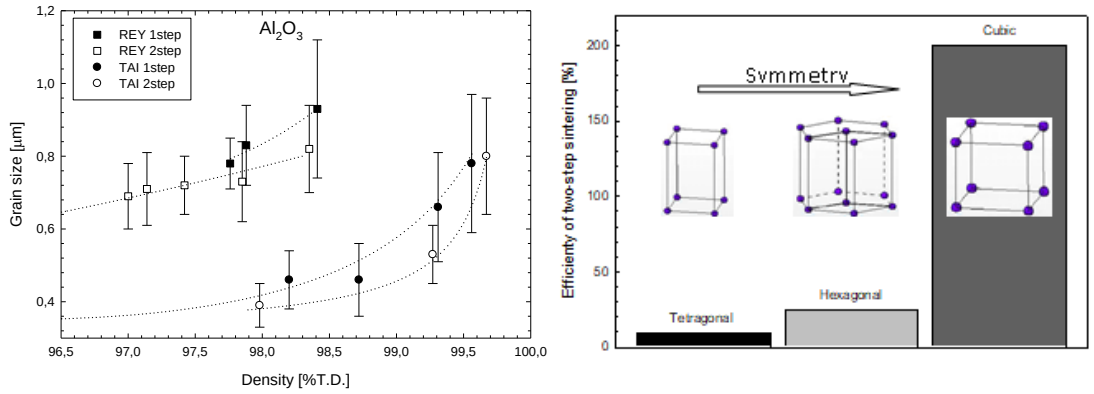

Obr. 5: a) Porovnání dosažené velikosti zrn pro Al_2O_3 s různou velikostí částic
b) zvětšující se účinnost Two Step Sintering se zvyšující se symetrií krystalové mřížky [1].

Pomalé slinování ve Spark Plasma Sintering/Hot Isostatic Pressing

V roce 2015 uveřejnili K. Morita a kol. článek, kde je popsán vliv pomalého slinování na optické vlastnosti Al_2O_3.MgO [45]. Uváděná technika se skládá z rychlého ohřevu na počáteční slinovací teplotu (např. 100 °C/min jako typická rychlost ohřevu pro Spark Plasma Sintering) následovaná velmi pomalým ohřevem (0,5 – 2 °C/min) na cílovou teplotu. Autoři uvedli, že tento postup jim umožnil dosáhnout nižší výsledné velikosti zrn a zároveň potlačit kontaminaci uhlíkem z grafitové formy.

2.4.3. Rychlé slinovací techniky

Rychlé slinovací techniky mají většinou za cíl dosažení stejné výsledné mikrostruktury za kratší výrobní čas. Tím se nejenom ušetří strojní čas, ale také se sníží náklady na energie díky menším tepleným ztrátám v průběhu dlouhých prodlev na vysokých teplotách. Graf potencionálních energetických úspor je schematicky znázorněn na Obr. 6.

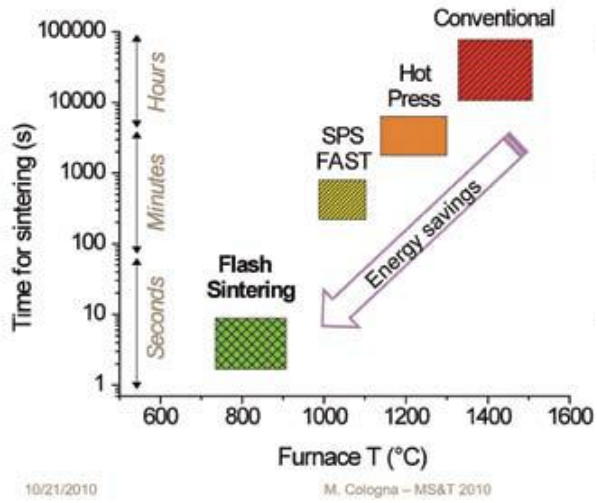

Obr. 6: Schéma znázorňující typické teploty a časy použitých slinovacích technik [46].

Spark Plasma Sintering

Jendou z moderních slinovacích technik je Spark Plasma Sintering (SPS). SPS využívá pro ohřev vzorku pulsní elektrický proud, který prochází elektricky vodivou (grafitovou) formou a případně vzorkem (pokud je elektricky vodivý). Pro zajištění elektrického kontaktu je přístroj vybaven hydraulickým přítlakem, díky kterému tak zároveň při slinování může být na vzorek vyvíjen externí tlak několika desítek kN. Externí tlak poté pomáhá zhutňovacímu procesu a SPS se tak spolu s Hot Pressingem (HP) a Hot Isostatic Pressingem (HIP) řadí mezi nejpoužívanější techniky slinování s využitím tlaku jako další hnací síly slinování.

Slinování metodou SPS je i přes mnoho let výzkumu stále velice debatovanou metodou a o jejím vlivu na mikrostrukturu či míře uhlíkové kontaminace (z grafitových forem) stále nepanuje shoda [47]. Obecně lze ale díky rychlému slinování a vysokému slinovacímu tlaku potlačit růst zrn a díky tomu připravit např. nanokeramické materiály [48].

Flash Sintering

V roce 2010 uveřejnili M. Cologna a R. Raj pokročilou metodu slinování nazvanou Flash Sintering [49]. Tato metoda spočívá v předehřátí vzorku na teplotu cca 850 °C (pro t-ZrO_2) a poté (na předem přichycené elektrody ke vzorku) přivádí elektrického pole v řádech cca 100 V/cm^{-1}. Schéma uspořádání vzorku a zdroje elektřiny je uvedeno na Obr. 7.

Slinovací smrštění nastane při vysokých elektrických polích během několika málo sekund, pravděpodobně díky jevu tzv. thermal runaway tedy Joulovu teplu vznikajícím ve vzorku při

průchodu elektrického Proudu. Vzorek tak během několika sekund dosáhne vysoké slinovací teploty potřebné na rychlé zhutnění [50].

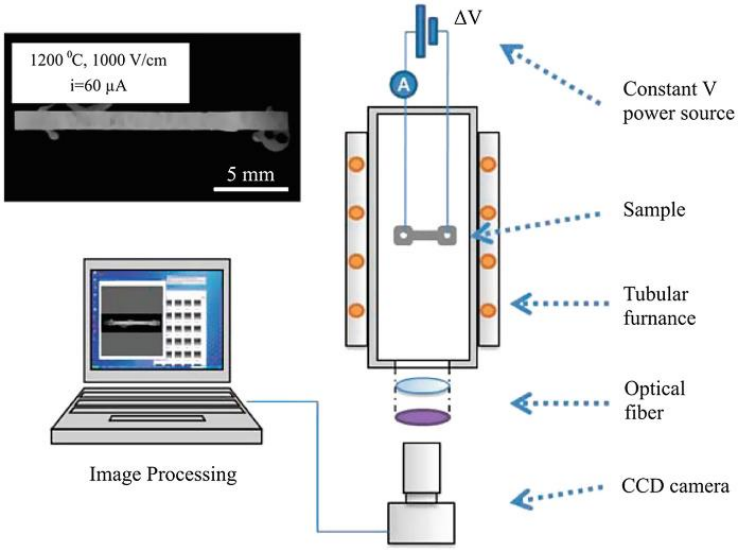

Obr. 7: Schéma experimentu Flash Sintering [49].

2.4.4. Fyzikální aktivace povrchu částic a její vliv na slinování

Vysokoenergetické mletí

Základním a nejpoužívanějším aktivátorem povrchu keramických částic je vysokoenergetické mletí. V průběhu mletí dochází k vytváření nových povrchů, které nejsou znečištěny a tím pádem jsou přístupné novým chemickým vazbám. [51]. Vysokoenergetické mletí se často používá pro syntézu v pevné fázi [20], dopování [52], apod.

Plazmová aktivace

Aktivace povrchů pomocí nízkoteplotní plasmy představuje moderní a dobře zavedenou techniku pro ovlivnění povrchové energie různých materiálů (polymerů, keramiky, kovů apod.) používanou např. pro zlepšení přilnavosti povlaků [53]. Společná interakce vysoko energetických elektronů, iontů, excitovaných molekul, radikálů a UV záření umožňuje vytvoření nových polárních skupin na pevném povrchu. Právě změna povrchu (povrchové energie) ovlivňuje všechny procesy, které jsou řízeny změnami povrchové energie, jako je např. slinovací proces.

2.4.5. Slinování vrstevnatých kompozitních materiálů

Vrstevnaté kompozitní materiály mohou být připraveny různými technikami, jako je např. tape casting, slip casting, elektroforetická depozice (EPD) apod. Při slinování vrstevnatých kompozitů dochází k tvorbě vnitřních napětí, a to má za následek unikátní šíření trhlin v takto připraveném vrstevnatém materiálu [54]. Vnitřní napětí, vnesené v průběhu slinování, způsobuje změny ve slinovacím chování tzv. slinováním pod napětím. Vnitřní napětí ovšem nevznikají pouze při slinování (kde se navíc předpokládá jejich relaxace za vysokých teplot), ale zejména při chlazení, díky rozdílu v koeficientu teplotní roztažnosti (α) mezi jednotlivými materiály [55].

Velikost zbytkových napětí pro kompozit (složený např. z Al_2O_3 a ZrO_2 střídajících se vrstev) může být spočítána pomocí následující rovnice [54, 56]:

$$\sigma_{rZrO_2} = \frac{(\alpha_{ZrO_2} - \alpha_{Al_2O_3}) \cdot \Delta T \cdot E_{ZrO_2}}{1 - \upsilon_{ZrO_2}} \cdot \left(1 + \frac{d_{ZrO_2}}{d_{Al_2O_3}} \cdot \frac{E_{ZrO_2} \cdot (1 - \upsilon_{Al_2O_3})}{E_{Al_2O_3} \cdot (1 - \upsilon_{ZrO_2})} \right)^{-1}, \tag{13}$$

kde d je tloušťka vrstvy, ν je Poissonův poměr, a E je modul elasticity.

3. Cíle práce

Předložená práce má za cíl popsat přínos uchazeče k vývoji pokročilých slinovacích technik v letech 2010-2022. Jako modelové materiály pro popis přínosu jednotlivých slinovacích technik byly zvoleny Al_2O_3 a ZrO_2, jako v praxi nejvíce rozšířené materiály.

Specifické cíle práce je pak možné shrnout následovně:

- Popsat vliv dopantů na slinovací chování
- Prokázat možnosti vzniku tzv. kinetického okna při pomalém slinování
- Prokázat vliv rychlého slinování na aktivační energii slinování
- Prokázat vliv změny povrchové energie na slinovací chování
- Popsat slinovací chování jednotlivých vrstev u vícevrstvých lamelárních kompozitů

4. Experimentální část

4.1. Použité materiály

Pro experimentální práci byly použity čtyři druhy komerčně dostupných oxidových keramických materiálů. Přehled použitých materiálů spolu s jejich značením a orientační velikostí částic udávané výrobcem shrnuje Tabulka 1.

Prášek	Výrobce	Typ	Označení	Velikost částic (nm)
ZrO_2 + 3mol.% Y_2O_3	Tosoh, Japan	TZ-3YS-E	TZ3Y	140
ZrO_2 + 8mol.% Y_2O_3	Tosoh, Japan	TZ8Y	TZ8Y	70
Al_2O_3	Taimei, Japan	TM-DAR	TAI	110
Al_2O_3	Malakoff, USA	HP-DBM	MAL	470

Tabulka 1: Přehled použitých keramických prášků

Dopování prášků

Pro zjištění vlivu dopantů na slinovací chování byl zvolen materiál TAI, díky jeho vysoké čistotě (99,99%). Dopanty (500 ppm Mg, Y, nebo 250 ppm Zr molárních k Al_2O_3) byly přidány do 100 g Al_2O_3 pomocí míchání s příslušným prekurzorem $Mg(NO_3)_2.6H_2O$ (p.a., Lachema Brno, Česká republika), nebo $C_4H_6O_4Zr$ (p.a., Lachema Brno, Česká republika), a $Y(NO_3)_3.6H_2O$ (99,8 % čistota, Sigma Aldrich) rozpuštěným v isopropanolu. Takto připravená směs byla homogenizována kulovým mletím Al_2O_3 mlecími koulemi po dobu 20 h. Výsledná směs byla rozmělněna v achátové misce a přesita přes 200 μm polyethylenové síto a kalcinována na 800 °C/ 1h. Jednotlivé vzorky jsou označeny dle odpovídajícího dopantu AM (MgO), AY (Y_2O_3), AZ (ZrO_2). Stejnou úpravou (kromě přidání dopantu) prošel i referenční prášek označený A.

Z důvodu možnosti ovlivnění vzorků kalcinací, která by mohla zkreslit výsledky [57], byl připraven prášek AMS pomocí smíchání TAI s $MgAl_2O_4$ spinelem a přesit přes 100 a 40 μm polyethylenové síto. Stejně byl přesit i referenční prášek označený AA. Podrobnosti k přípravě jednotlivých prášků jsou uvedeny v [22].

4.2. Úprava prášků

Úprava povrchové energie prášků

Práškové materiály pro kapitolu 5.4. byly předem upraveny dle následujícího postupu: materiály TAI a TZ3Y byly povrchově aktivovány pomocí difuzního koplanárního povrchového výboje (DCSBD). Schéma použitého zařízení je uvedeno na Obr. 8. Postup povrchové plazmové aktivace prášků se skládal z opakovaného nanášení cca 0,25 g prášků na elektrodu. Po nanesení byl prášek aktivován při výkonu generátoru 400 W po dobu 45 s (pro materiál TAI), nebo 500 W po dobu 30 s (pro materiál TZ3Y). Celý proces se opakoval, dokud nebylo získáno asi 40 g prášku pro následné tvarování a slinování. Podrobnosti plazmové aktivace prášku jsou uvedeny v [12].

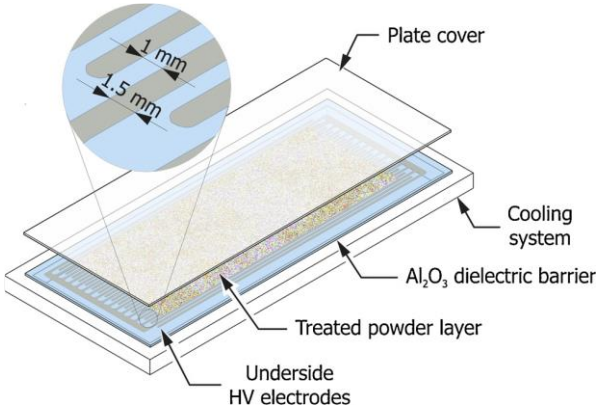

Obr. 8: Schématický nákres DCSBD použitého pro aktivaci prášků [12].

4.3. Tvarování

Lisování

Pro experimenty suchého tvarování bylo z výše uvedených materiálů naváženo 12 g prášku. Navážený prášek byl dán do pryžové formy a vylisován v izostatickém lisu (Autoclave Engineering Inc., USA) tlakem 300 MPa po dobu 5 min. Z takto vyrobených disků byly následně vyřezány hranoly o hmotnosti cca 1 g a rozměrech cca 7x7x12 mm vhodné pro vysokoteplotní dilatometrii.

Odlévání

Z prášku TAI a TZ3Y (upravené dle kap. 4.2.) byly připraveny suspenze určené na odlévání pomocí metody slip casting. Jednotlivé směsi prášků a vody byly připraveny tak, aby se dodrželo 37 % obj. plnění keramickým práškem a bylo získáno 30 g směsi. Pro stabilizaci

suspenze bylo použito 2,2 hm% disperzantu Darvan (Vanderbilt Minerals). Takto připravené směsi poté byly homogenizovány buďto pomocí ultrazvuku (vzorky označené US, Sonoplus, HD2020, Bendelin, Německo) po dobu 1 minuty při atmosférickém tlaku a intenzivního vodního chlazení, nebo za pomocí kulového mletí po dobu 24 hodin (vzorky označené BM). Po dokončení homogenizace byly suspenze odlity do plastových misek a sušeny na vzduchu po dobu 7 dní. Podrobnosti přípravy těchto polotovarů jsou uvedeny v [12] pro nedopované prášky a ve [22] pro dopované prášky.

Elektroforetická depozice

Pro kapitolu 5.5 byly elektroforetickou depozicí z prášků MAL a TZ3Y (viz Tabulka 1) připraveny střídáním cca 100 jednotlivých vrstev monolity MAL a TZ3Y a kombinované kompozity s tloušťkami v poměru Al_2O_3: ZrO_2 2:1 (označené Z33), 1:1 (označené Z50) a 1:2 (označené Z67). Samotná elektroforetická depozice byla prováděna v elektroforetické cele v módu konstantního proudu 5 mA. Vzdálenost mezi korozivzdornými elektrodami s efektivním povrchem 18 cm^2 byla 26 mm. Pro referenci byly také připraveny stejnou cestou monolity z materiálu MAL (označeno A) a TZ3Y (označeno Z). Všechny depozity byly sušeny po dobu alespoň 24 hodin za pokojové teploty a následně byly předžíhány na 800 °C na vzduchu pro získání manipulační pevnosti. Podrobnosti provedené elektroforetické depozice jsou uvedeny v [35].

4.4. Slinování

Konvenční slinování probíhalo ve vysokoteplotní peci Heraeus (K1700/1, Německo) a CLASIC (HT 1780C, Česká Republika). Vysokoteplotní dilatometrie byla provedena v dilatometru Linseis (L70/1700, Německo). Slinování vzorků keramických kompozitů bylo monitorováno pomocí vysokoteplotní dilatometrie jak v podélném, tak v příčném směru při rychlostech ohřevu 2, 5, 10 a 20 °C/min. Schéma uspořádání slinování keramických vzorků v dilatometru je uvedeno na Obr. 9.

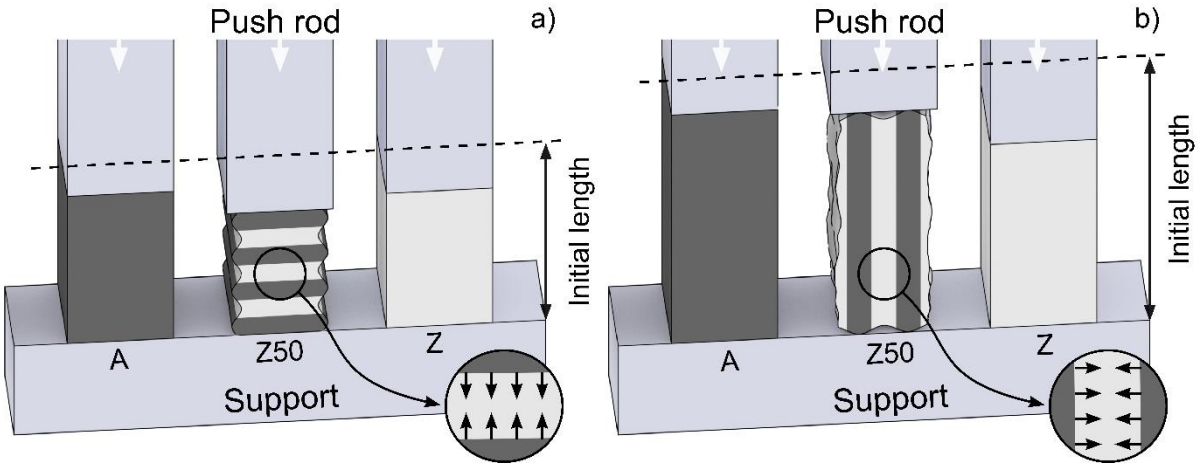

Obr. 9: Schéma slinování kompozitů v a) příčném a b) podélném směru monolitických materiálů A (MAL), Z (TZ3Y) a vrstevnatého kompozitu Z50 [35].

Pro kapitolu 5.3 byly vzorky slinuty v zařízení SPS (SPS625, dr. Sinter JEOL, Japonsko). Do grafitové formy o průměru 12 mm vyložené grafitovým papírem byly nasypány 2 g daného prášku. V průběhu slinování byl udržován konstantní uniaxiální tlak o velikosti 50 MPa. Teplota vzorku byla měřena pomocí optického pyrometru zaměřeného na slepou díru vyvrtanou ve středu formy. Vzorky byly nejdříve předehřáty na 800 °C s 1 minutovou prodlevou na této teplotě pro stabilizaci systému a pak zahřáty různými rychlostmi ohřevu od 50 do 750 °C/min, dokud nebylo dosaženo finální teploty (1450 – 1500 °C).

4.5. Analytické metody

Hustota keramických polotvarů a výsledných těles byla měřena na analytických vahách (Mettler Toledo, XSE 105, U.S.A.) pomocí Archimedova principu metodou trojího vážení (EN 623-3) za použití vody destilované pro analytické účely. Pro výpočet výsledné hustoty materiálů byly použity teoretické hustoty materiálů: 6,08 g/cm^3 pro ZrO_2 s 3mol % Y_2O_3, 5,99 g/cm^3 pro ZrO_2 s 8mol % Y_2O_3 a 3,99 g/cm^3 pro Al_2O_3. U kompozitů byla teoretická hustota určena podle směsného pravidla.

Vzorky byly po měření hustoty rozřezány a vyleštěny pomocí standartních keramografických postupů pro další pozorování pomoci SEM.

Velikost zrn byla spočtena pomocí lineární průsečíkové metody EN 623-3 za použití alespoň pěti SEM fotografií.

4.6. Výpočet aktivační energie slinovacího procesu

Pro konstrukci MSC (kap. 5.1, a 5.5) byly použity čtyři rychlosti ohřevu a to 2, 5, 10 a 20 °C/min. Pro konstrukci MSC pro rychlé slinování (kap. 5.2) byly vzorky slinuty v zařízení SPS za použití rychlostí ohřevu 50, 100, 150, 200, 250, 300, 350, 400, 450, 500, 550, 600, 650, 700, 750 a 800°C/min. Pro konstrukci MSC byly vždy využity tři nejbližší rychlosti ohřevu (např. pro rychlost 500°C/min byly využity rychlosti 450, 500 a 550 °C/min). Pro vytvoření MSC pro kompozitní materiály (kap. 5.3) byla použita modifikace Master Skrinkage Curve (viz kap. 2.2.3.).

Délková roztažnost vzorků byla přepočítána na změnu hustoty za použití vlastního softwaru Density (VUT Brno, [23]). Z takto vytvořených dilatometrických křivek pak byla vypočtena aktivační energie slinování za pomocí softwaru Density MSC [30].

4.7. Výpočet aktivační energie růstu zrn

Pro výpočet aktivační energie růstu zrn byl použit kinetický model popsaný v kapitole 2.3.1 [38] a model Master Grain Growth Curve popsaný v kapitole 2.3.2. Pro stanovení aktivační energie zrn oběma metodami byl materiál TZ8Y slinován na teploty 1400, 1450 a 1500 °C s prodlevami 1, 5, 10, 20, 40 a 60 hodin.

5. Výsledky a diskuze

5.1. Ovlivnění slinovacího chování pomocí dopantů

Vliv dopování na slinovací chování bylo testováno na Al_2O_3 materiálu TAI (vit Tabulka 1). Slinovací trajektorie jednotlivých dopovaných a referenčních vzorků materiálu TAI jsou zobrazeny na Obr. 10. Z výsledků je patrné, že u všech slinovacích režimů (jejichž detaily uvádí publikace [22]) dochází k významnému růstu zrn až nad hustotami 98 %t.h..

Ze slinovacích křivek byla pomocí kinetického slinovacího modelu (kap. 2.2.1) vypočtena E_A až do hustot 95 %t.h.. Aplikace tohoto slinovacího modelu až do takto vysokých relativních hustot může být oprávněná, protože:

- Nedochází k významnému růstu zrn až do 98 %t.h.
- Pro jednotlivé slinovací režimy existuje pouze jedna slinovací trajektorie [58].

Vypočtené E_A dle kinetického modelu jsou uvedeny na Obr. 10 a lze je shrnout do následujících třech oblastí:

- 60-75 %t.h.: oblast konstantní E_A (730 – 890 kJ/mol podle dopantu)
- 75-85 %t.h.: oblast měnící se E_A
- 85-95 %t.h.: oblast snížené E_A (620 – 750 kJ/mol podle dopantu)

Pro ověření těchto výsledků byl použit i model Master Sintering Curve pro zjištění aktivační energie slinovacího procesu pro jednotlivé regiony, tedy pod 75 %t.h. a nad 85 %t.h. (viz Obr. 11).

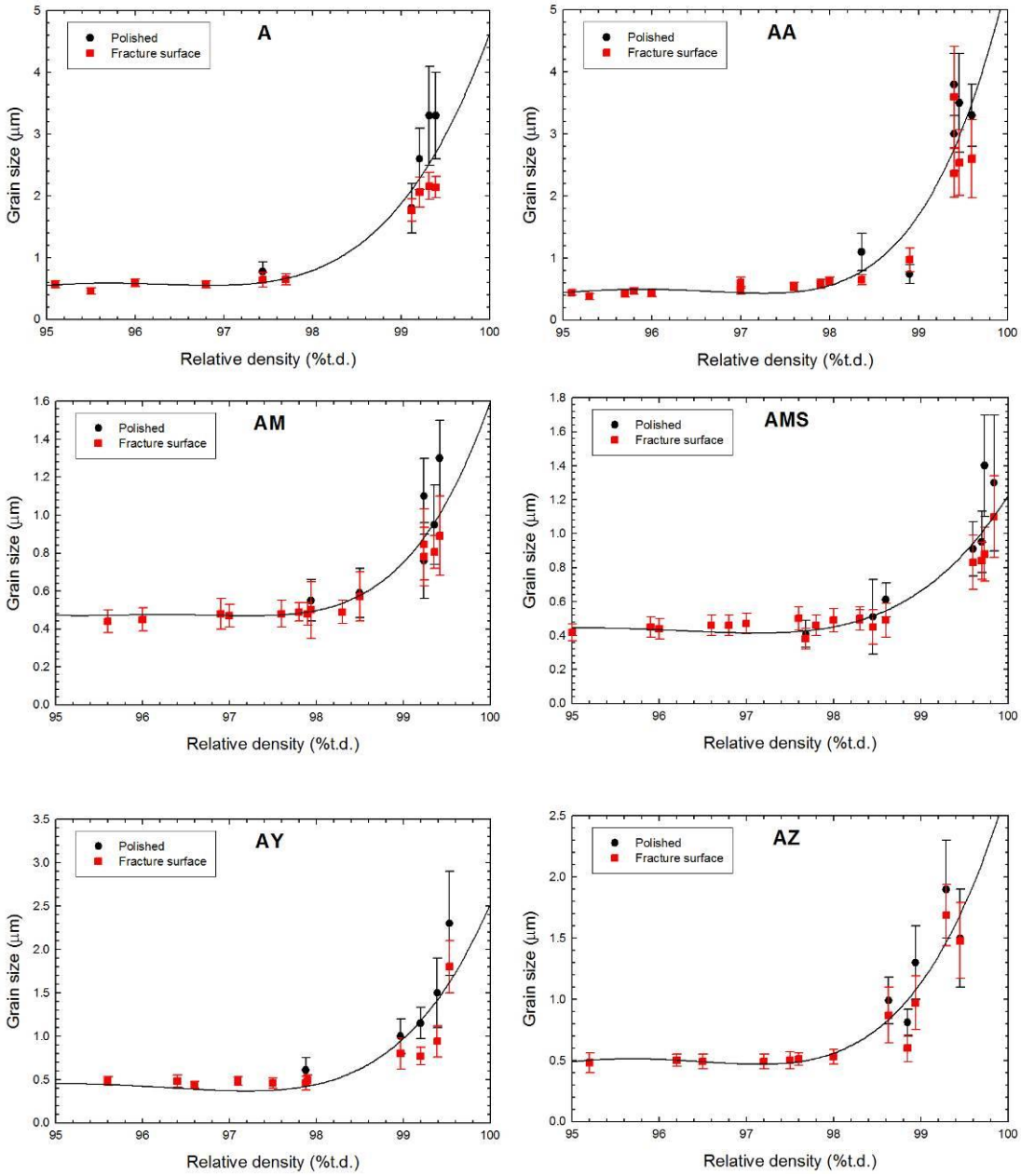

Obr. 10: Slinovací trajektorie dopovaných a nedopovaných prášků TAI (A, AA - nedopované prášky, AM - dopovaný MgO, AMS - dopovaný MgO bez kalcinace, AY - dopovaný Y_2O_3, AZ - dopovaný ZrO_2) [35].

Pro výpočet aktivační energie v jednotlivých fázích slinování je nutné původní model MSC upravit. Nejjednodušší úpravou je rozdělení MSC modelu do několika fází, pro které se určí aktivační energie slinování samostatně dle následující rovnice:

$$\Theta = \int_0^{t<t_1} \frac{1}{T}\exp\left(-\frac{E_{A1}}{RT1}\right)dt + \int_{t_1}^{t} \frac{1}{T}\exp\left(-\frac{E_{A2}}{RT}\right)dt, \qquad (14)$$

kde t_1 je čas, kdy se jednotlivé mechanizmy mění.

S takto upraveným modelem nazvaný Two-Stage Master Sintering Curve (TS-MSC) [31] lze již vypočítat aktivační energii slinování v jednotlivých fázích samostatně (viz Obr. 11).

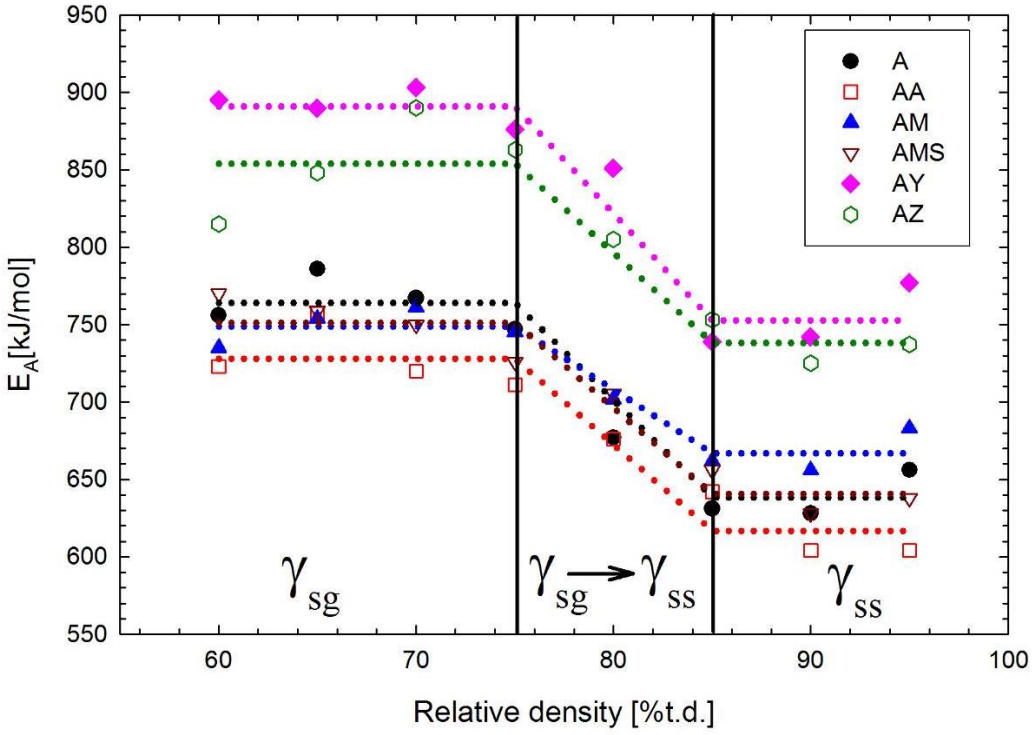

Obr. 11: Aktivační energie slinovacího procesu, vypočtena kinetickou metodou (body) a metodou Master Sintering Curve (křivky), jako funkce relativní hustoty [35].

Vypočtené hodnoty E_A pomocí metody MSC jsou uvedeny na Obr. 12. Z výsledků lze vidět, že E_A stanovené oběma metodami jsou obdobné.

Postupný pokles E_A v průběhu zhutňování ukazuje, že se v průběhu slinování pravděpodobně mění zhutňovací mechanizmus. Při slinování Al_2O_3 jsou nejvýznamnějšími slinovacími mechanizmy difuze po hranicích zrn a mřížková difuze [59]. Podle doposud publikovaných slinovacích diagramů lze očekávat, že difuze po hranicích zrn bude dominovat po celou dobu slinování. Mřížková difuze by měla být dominantní až za extrémně vysokých teplot (cca 2000 °C).

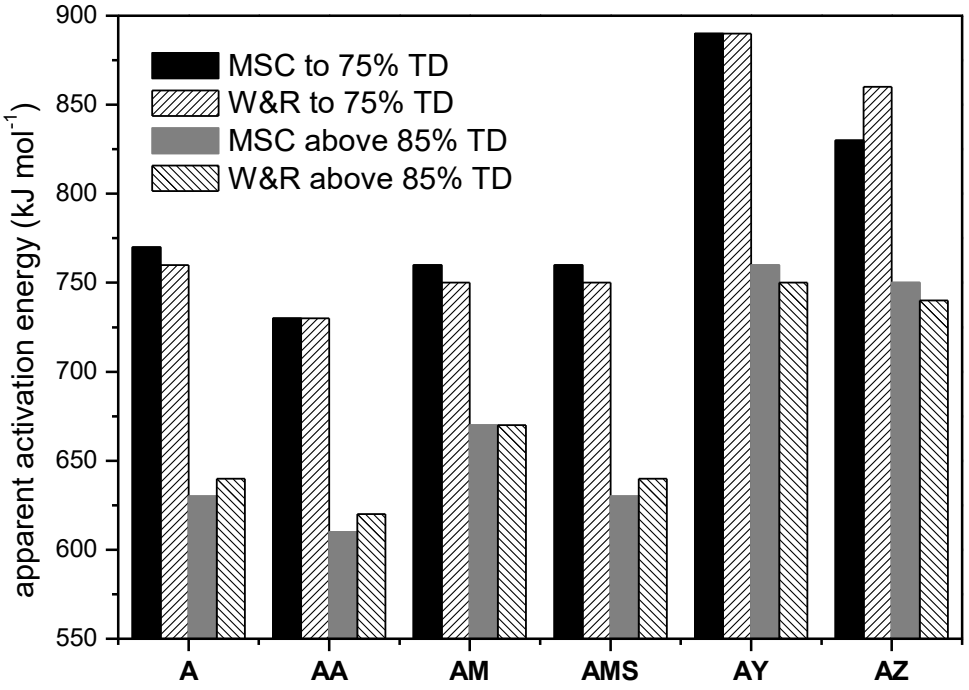

Obr. 12: Porovnání aktivačních energií slinovacího procesu vypočtené kinetickou metodou a metodou Master Sintering Curve pro jednotlivé materiály [35].

Z tohoto důvodu vypadá změna slinovacího mechanizmu velice kontroverzně [18, 60]. S větší pravděpodobností dochází ke zpomalování slinovacích mechanizmů na začátku slinování kvůli započítání povrchové difuze, která nepřispívá ke zhutnění, ale ubírá hnací sílu slinování [61, 62]. Při slinování je potřeba také poukázat na rozdíl v efektivní oblasti, která slouží jako zdroj bodových defektů a také na délku difuzní cesty. Možný pokles E_A u vyšších hustot totiž může být způsoben změnou geometrie pórů a zrn v průběhu slinování. V nízkých hustotách volná energie rozhraní plyn - pevná fáze významně přispívá k celkové volné energii systému a povrchová energie γ_{SG} hraje významnou roli [18]. V této fázi slinování tvoří hranice zrn pouze

malý zlomek celkového aktivního povrchu. Hranice zrn jsou plné dislokací a defektů, jejichž počet určuje rychlost difuze. Při sníženém počtu hranic zrn tím pádem dochází k pomalejšímu přenosu hmoty a tím pádem i ke snížení rychlosti zhutňování [28]. Nižší objem hranic zrn v počáteční a střední fázi slinování zhoršuje přenos hmoty, což se odráží ve vyšší E_A. V průběhu poslední slinovací fáze je již povrch hranic zrn velký, proto k difuzi může dojít snadněji, což vede ke snížení E_A.

V případě dopantů je zhutňování potlačeno obzvláště přidáním 500 ppm Y_2O_3, nebo 250 ppm ZrO_2, což je reflektováno vysokou E_A při nízkých i vysokých hustotách. Oba dopanty silně segregují na Al_2O_3 rozhraních. Díky limitované rozpustnosti v Al_2O_3 krystalu (~10 hmotnostních ppm) Y segreguje na Al_2O_3/Al_2O_3 rozhraních [63, 64], což vede k redukování rychlosti zhutňování. Dopování MgO má na druhou stranu pouze malý efekt na zhutňování. Materiál AM (kalcinovaný) dosáhl nižší počáteční a finální hustoty, pravděpodobně kvůli přítomnosti aglomerátů [17]. Materiály AM i AMS dosahují stejné E_A v nízkých hustotách, nicméně ve vysokých hustotách byla hodnota E_A materiálu AMS nižší. Kalcinace tedy pravděpodobně vedla ke zvětšení počtu superkritických pórů, které se mnohem hůře odstraňují [65].

Závěr kapitoly

Vzorky materiálu TAI byly úspěšně dopovány Y, Zr a MgO a byly slinovány na různé teplotní cykly. Výpočty aktivační energie slinování (E_A) ukázaly, že E_A se může v průběhu slinování zmenšovat. U všech zkoumaných dopantů byl pozorován stejný trend poklesu aktivační energie slinovacího procesu, i když dopanty Y a Zr měli významný vliv na slinování, a dopant MgO měl v dané koncentraci na slinování pouze nevýrazný vliv.

Publikace uchazeče v daném tématu (tučně jsou uvedeny články, které jsou přílohou do této práce):

[21] POUCHLY, V., MACA, K., SHEN, Z. Two-step sintering and spark plasma sintering of Al_2O_3, ZrO_2 and $SrTiO_3$ Ceramics, *Integrated Ferroelectrics*, 2008, vol. 99[1], 114-124.

[66] POUCHLY, V., MACA, K. Master sintering curves of two different alumina powder compacts, *Proc. Appl. Cer.*, 2009, vol. 3[4], 177-180.

[1] MACA, K., POUCHLY, V., ZALUD, P. Two-Step Sintering of Oxide Ceramics with Various Crystal Structures, *J. Eur. Ceram. Soc.*, 2010, vol. 30 [2] 583-89.

[34] POUCHLY, V., MACA, K. Master Sintering Curve – A Practical Approach for Its Construction, *Sci. Sinter.*, 2010, vol. 42[1], 25-32.

[31] MACA, K., POUCHLY, V., SHEN, Z. Two-stage master sintering curve applied to two-step sintering of oxide ceramics, *J. Eur. Ceram. Soc.*, 2013, vol. 33 [12] 2275-2283.

[22] POUCHLY, V., BODISOVA, K., SVANCAREK, P., GALUSEK, D. Densification of fine-grained alumina ceramics doped by magnesia, yttria and zirconia evaluated by two different sintering models, *J. Eur. Ceram. Soc.*, 2014, vol. 34[16], 4363-4372.

[67] BODISOVA, K., GALUSEK, D., SVANCAREK, P. POUCHLY, V., MACA, K. Grain growth suppression in alumina via doping and two-step sintering, *Ceramics International*, 2015, vol. 41, 11795-11983.

5.2. Dlouhodobé slinování na nižších teplotách

Tato kapitola se zabývá experimentálními výsledky získané aplikací slinovací metody dvojstupňového slinování pro tři keramické materiály. U materiálu TZ8Y je dále ukázán postup při hledání tzv. kinetického okna slinování.

Výpočet aktivační energie slinovacího procesu

Aktivační energii slinovacího procesu pro materiál TAI vypočtenou pomocí metody MSC ukazuje Obr. 13. Do grafu je vnesena E_A vypočtená z klasických dilatometrických dat, s rychlostí ohřevu 2, 5, 10 a 20 °C/min, ale také křivka Θ_i (viz rovnice 10) vypočtená ze slinovacího režimu metodou TSS (podrobnosti slinovacího režimu jsou uvedeny v literatuře [30]). Z Obr. 13 lze vypozorovat, že při slinování pomocí metody TSS dochází k odklonu Θ_i křivky k nižším E_A.

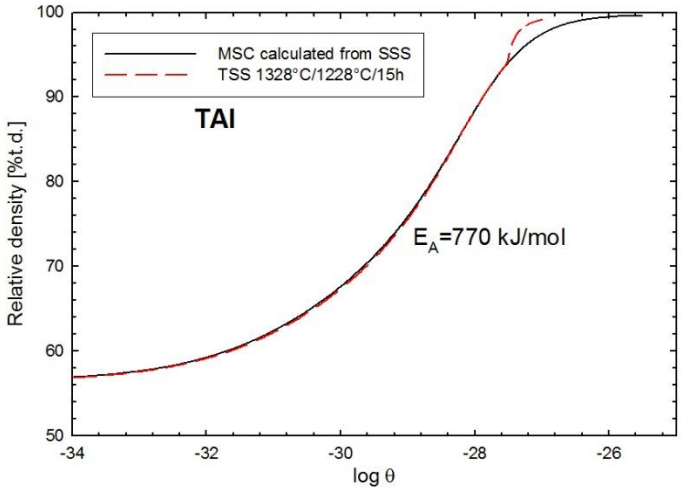

Obr. 13: Odklon experimentu dvojstupňového slinování (TSS) od původní MSC zkonstruované z běžných, jednostupňových slinovacích režimů (SSS) [31].

Základní model MSC vychází z předpokladu, že jeden difuzní mechanizmus dominuje celému slinovacímu procesu. Slinovací proces je ovšem složen z několika fází, přičemž každá fáze slinovacího procesu závisí na jiných parametrech. V tomhle případě bylo ale nutné aplikovat opět rozdělení MSC na více fází, stejné jako v kapitole 5.1. Díky rozdělení aktivační energie slinování na dva samostatné úseky bylo zjištěno, že aktivační energie slinování se pro některé materiály v poslední fázi slinování zmenšuje, což je v souladu s výpočtem aktivační energie i pomocí Wang&Rajova modelu, což ukazuje např. pro materiál TZ8Y Obr. 14 [31, 58]. Toto

snížení aktivační energie slinovacího procesu lze pozorovat u všech použitých materiálů (Obr. 15).

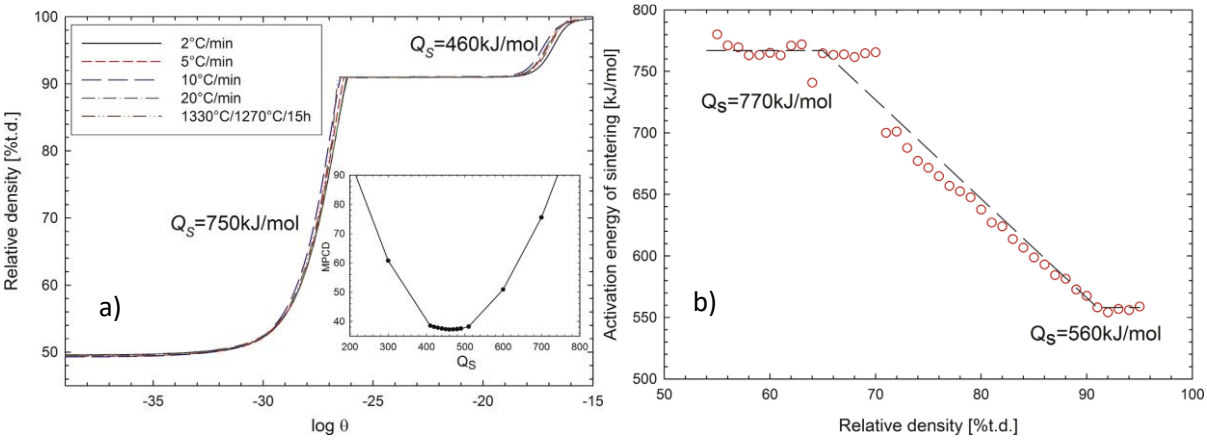

Obr. 14: a) Výpočet aktivační energie slinovacího procesu materiálu TZ8Y metodou two-stage MSC b) Výpočet aktivační energie slinovacího procesu kinetickou metodou [68].

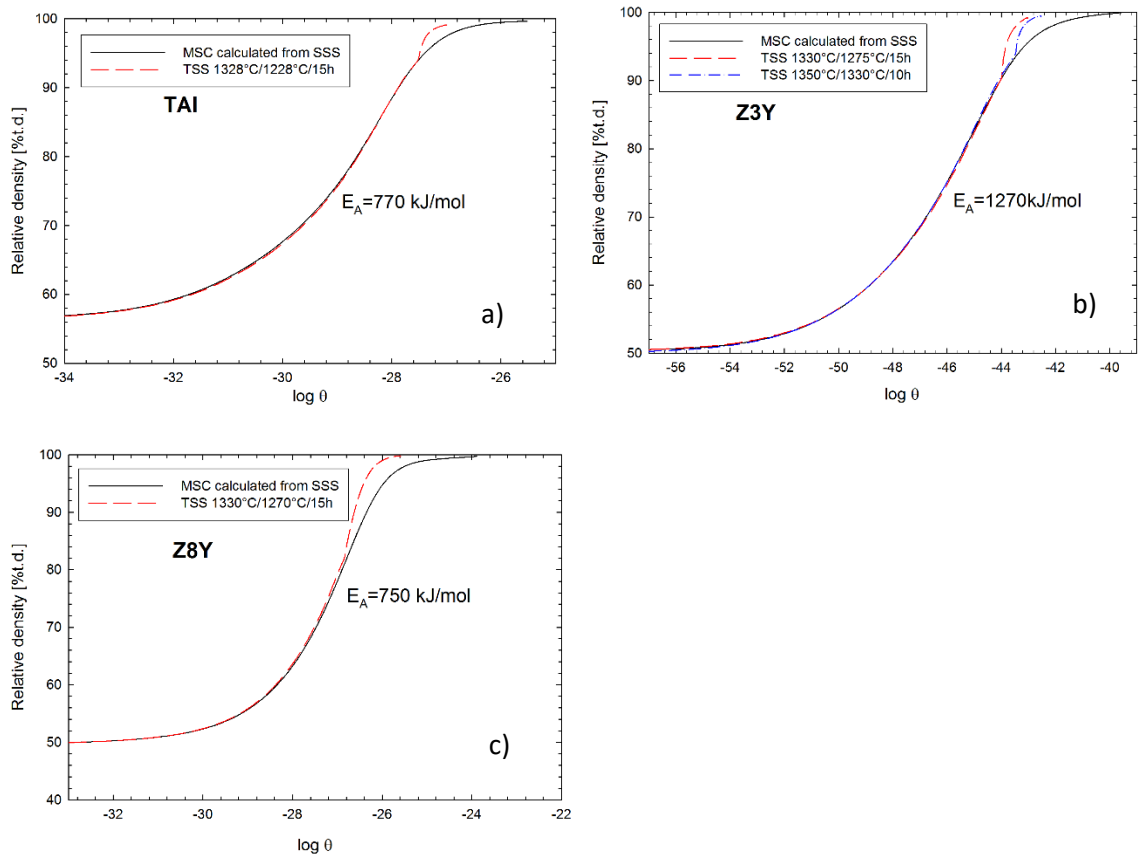

Obr. 15: Odklon MSC křivky pro materiály a) TAI, b) TZ3Y a c) TZ8Y v průběhu slinování [31].

Výpočet aktivační energie růstu zrn

Pro ověření možnosti existence kinetického okna slinování je nutné vypočítat i aktivační energii růstu zrn a porovnat ji s velikostí E_A. Pro výpočet aktivační energie růstu zrn byly zvoleny dvě výpočtové metody (viz Kap. 2.3.1 a 2.3.2), jejichž výsledky ukazuje Obr. 16. Podle kinetické metody výpočtu (Obr. 16a) je aktivační energie růstu zrn rovna 645 kJ/mol, přičemž pomocí metody Master Grain Growth Curve (Obr. 16b) 590 kJ/mol. Hodnoty vypočtené aktivační energie růstu zrn jsou v porovnání s průměrnou aktivační energií slinování E_A nižší (770 kJ/mol – viz Obr. 14a), což znamená, že by nemělo docházet ke zhutňován bez růstu zrn. Dle výsledků této práce ovšem dochází v poslední fázi slinovacího procesu (kde dochází k největšímu růstu zrn) ke snižování E_A a E_A je tedy menší, než E_{GG}. Tento výsledek ukazuje na možnost slinování v tzv. kinetickém okně, tedy možnosti, že při správně zvolené teplotě lze slinovat bez růstu zrn. Možnosti takovéhoto slinování jsou poté uvedeny v literatuře [68] a [69].

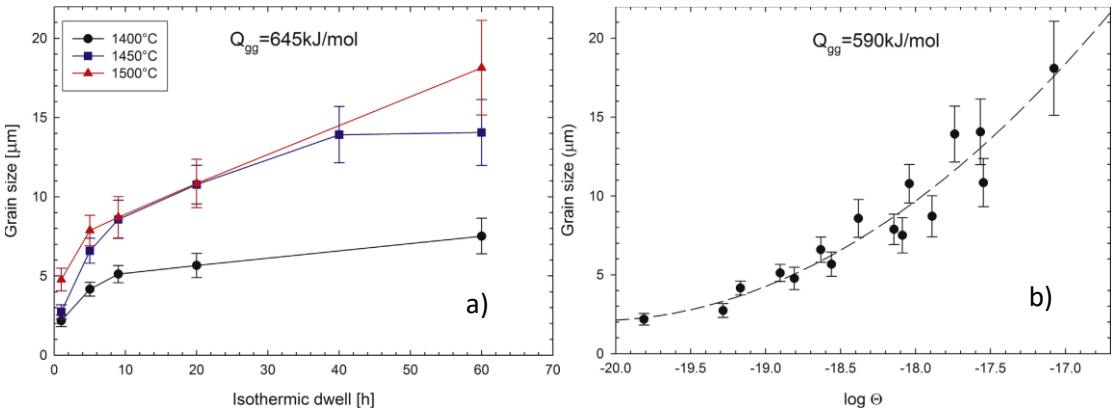

Obr. 16: a) Vývoj průměrné velikosti zrn pro materiál TZ8Y b) Výpočet aktivační energii růstu zrn metodou Master Grain Growth Curve [68].

Závěry kapitoly:

V této kapitole bylo ukázáno, že aktivační energie slinování materiálů TAI, TZ3Y a TZ8Y se v poslední fázi slinování snižuje. Dále bylo pro materiál TZ8Y zjištěno, že v poslední fázi slinování (kdy dochází k růstu zrn) je aktivační energie růstu zrn vyšší než aktivační energie slinovacího procesu, je tedy teoreticky možné nalézt kinetické okno slinování a slinovat bez růstu zrn.

Publikace uchazeče v daném tématu (tučně jsou uvedeny články, které jsou přílohou této kapitoly):

[31] POUCHLY, V., MACA, K., SHEN, Z. Two-stage master sintering curve applied to two-step sintering of oxide ceramics, *J. Eur. Ceram. Soc.*, 2013, vol. 33 [12] 2275-2283.

[70] WANG, L., POUCHLY, V., MACA, K., SHEN, Z. J. Intensive particle rearrangement in the early stage of spark plasma sintering proces, *Journal of Asian Ceramic Societies*, 2015, vol. 3, 183-187.

[68] POUCHLY, V., MACA, K., Sintering kinetic window for yttria-stabilized cubic zirconia, *J. Eur. Ceram. Soc.*,vol. 2016, 36, 2931-2936.

5.3. Slinování vysokou rychlostí ohřevu

Obr. 17 ukazuje dilatometrická měření pro obvyklé rychlosti ohřevu při slinování materiálu TZ8Y (viz Tabulka 1). Z grafu je patrné, že při použití nižších rychlostí ohřevu jsou stejné hustoty (např. 90 a 95 %t.h. vyznačené v grafu) dosažené při nižší teplotě. Tato skutečnost je dána delší dobou, po které těleso setrvává v určitém teplotním intervalu, což je typické chování pozorované i u jiných materiálů.

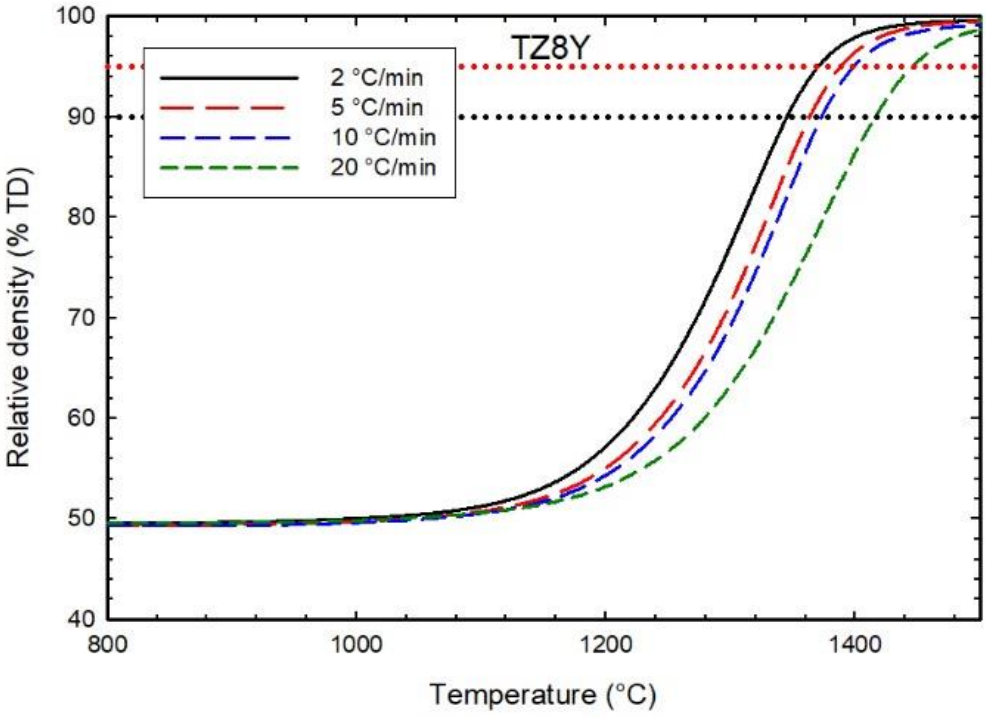

Obr. 17: Zhutňovací křivky pro materiál TZ8Y slinovaný konvenčními rychlostmi ohřevu 2, 5, 10 and 20 °C/min. Tečkované čáry uvádějí dosažení 90 a 95 %t.h..

Pokud se ovšem začne rychlost ohřevu zvyšovat více (viz Obr. 18), tak se teplota, při které u vzorků dojde k dosažení stejné relativní hustoty (v grafu vyznačeno 90 a 95 %t.h.), začíná chovat rozdílně. Při rychlostech ohřevu cca 50 – 450 °C/min již nemá zvětšující se rychlost ohřevu při které je dosaženo 90 a 95 %t.h., žádný vliv a od rychlostí ohřevu 450 °C/min se dokonce začíná tato teplota snižovat. Vyšší rychlost ohřevu tedy urychluje slinovací proces. Jak naznačují mnohé studie, při rychlosti ohřevu vyšší, než je 450 °C/min, může docházet k preferenčnímu ohřevu hranic zrn [71, 72]. Při vyšší lokální teplotě dochází ke zrychlení difuze po hranicích zrn a ke zhutnění vzorku tak dochází na nižší vnější teplotě [71].

Pro jednotlivé rychlosti ohřevu byla pomocí metody MSC stanovena E_A. Výsledky vypočtené E_A jsou ukázány na Obr. 19. Z grafu lze pozorovat, že při zvyšující se rychlosti ohřevu dochází

k poklesu E_A. Na Obr. 19 je také ukázána extrapolace E_A slinování za přítomnosti tlaku metodou SPS, která se při nízkých rychlostech ohřevu blíží k E_A stanovené pro konvenčně slinované prášky.

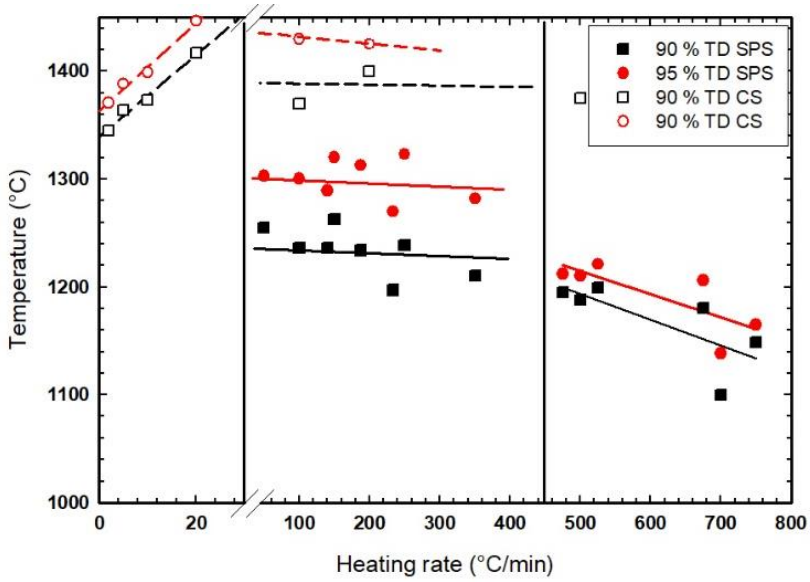

Obr. 18: Graf závislosti, dosažení 90 (nebo 95) %t.h. pomocí konvenčního (CS), nebo SPS slinování v závislosti na rychlosti ohřevu pro materiál TZ8Y.

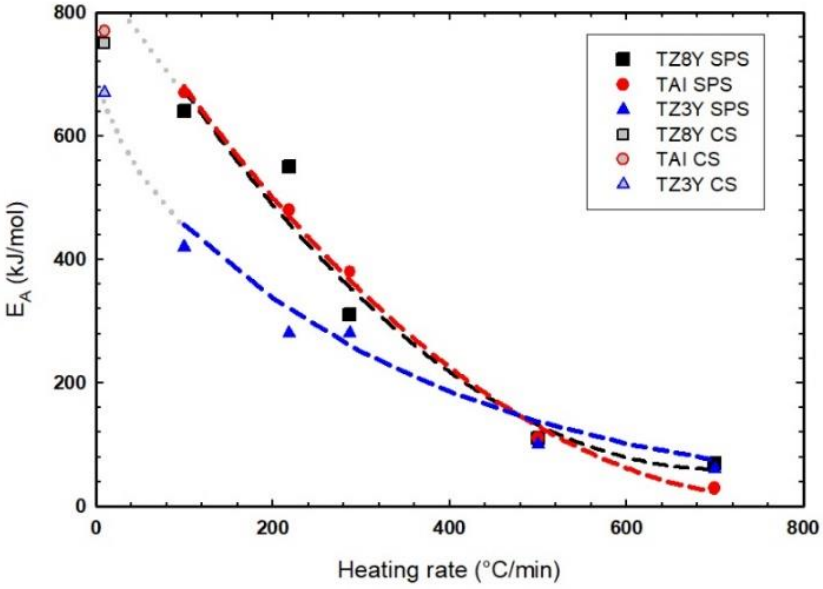

Obr. 19: Závislost vypočtené aktivační energie slinovacího procesu (E_A) na rychlosti ohřevu pro konvenční slinování (CS) a Spark Plasma Sintering (SPS) [34].

Závěry kapitoly:

Vzorky TAI, TZ3Y a TZ8Y byly slinuty rychlostmi ohřevu 2 – 750 °C/min a byla z nich vypočítané aktivační energie slinovacího procesu pro jednotlivé slinovací rychlosti. Výsledky ukazují, že při nižších rychlostech ohřevu (5 – 20 °C/min) dochází ke slinování při vyšších teplotách. Při vyšších rychlostech ohřevu (450 – 750 °C/min) dochází ke snižování slinovací teploty pravděpodobně díky lokálnímu ohřevu hranic zrn a tím pádem dochází ke zhutnění na nižší celkové teplotě Při rychlostech ohřevu (50 – 450 °C/min) pravděpodobně dochází k superpozici obou výše uvedených dějů a proto zde nemá rychlost ohřevu na slinovací teplotu významný vliv.

Publikace uchazeče v daném tématu:

[48] KOCJAN, A., POUCHLY, V., SHEN, Z. Processing of zirconia nanoceramics from a coarse powder, *J. Eur. Ceram. Soc.*, 2015, vol. 35, 1285-1295.

[70] WANG, L., POUCHLY, V., MACA, K., SHEN, Z. J. Intensive particle rearrangement in the early stage of spark plasma sintering proces, *Journal of Asian Ceramic Societies*, 2015, vol. 3, 183-187.

[33] DONG, J., POUCHLY, V., BIESUZ, M., TYRPEKL, V., VILEMOVA, M., KERMANI, M., REECE, M., HU, C. F.,GRASSO, S. Thermally-insulated ultra-fast high temperature sintering (UHS) of zirconia: A master sintering curve analysis, *Scripta Materialia*, 2021, vol. 203, pp.114076.

POUCHLY, V., SPUSTA, T., KALOUSEK, R., MACA., K. Densification behaviour of oxide ceramics at high heating rates, *in preparation.*

5.4. Vliv fyzikální aktivace povrchu částic na slinovací chování

Na Obr. 20 jsou uvedeny výsledky porozimetrie keramických polotovarů připravených lisováním (CIP), nebo odléváním (SC) s plazmou aktivovaným povrchem částic materiálu TAI (A), nebo původního TAI prášku (R). Výsledky ukazují, že plazmová aktivace vedla ke zmenšení pórů a změně jejich distribuce uvnitř keramického polotovaru v případě vlhkého tvarování (SC), viz Obr. 20a..

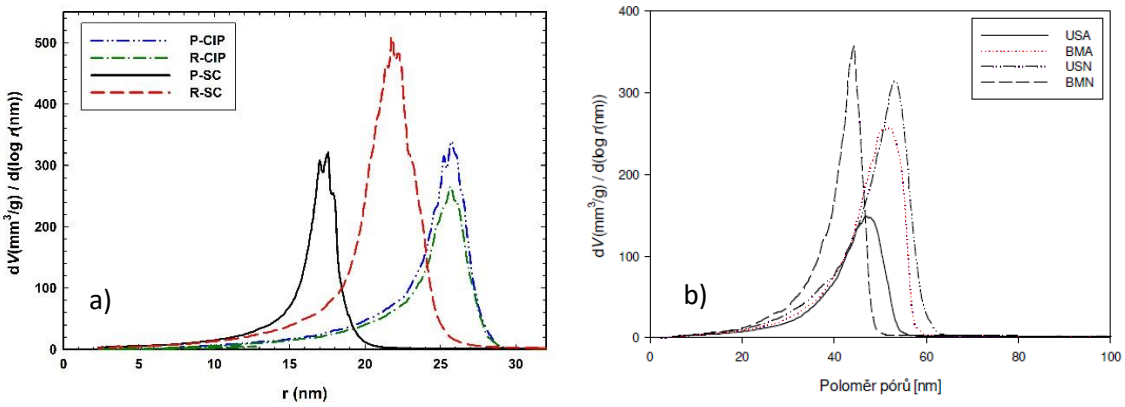

Obr. 20: Průměrná velikost a distribuce pórů pro materiál a) TAI (P-plasmou aktivované, R-referenční, CIP – lisované, SC-odlévané vzorky) b) TZ3Y (A-aktivované, N-neaktivované, US- stabilizované ultrazvukem, BM – mleté vzorky [12, 73]).

Vysokoteplotní dilatometrie TAI plazmou aktivovaných i neaktivovaných keramik je zobrazena na Obr. 21. Z výsledků je patrné, že pro materiál TAI nedošlo při tvrování pomocí izostatického lisování k významnému posunu slinovací křivky (viz Obr. 21a), což je zřejmě důsledkem nezměněné mikrostruktury keramického polotovaru (viz Obr. 20b). Při lisování fyzikálně aktivovaného prášku tedy nedošlo k žádnému zlepšení slinovatelnosti. Na druhou stranu ale nedošlo ani k žádnému zhoršení, materiál tedy nebyl průběhem plazmování negativně ovlivněn, či dokonce znehodnocen. Jednou z možností negativního ovlivnění je např. tzv. iontový vítr, který v průběhu aktivace dovede posouvat s částicemi aktivovaného prášku a může tak dojít k odstranění nejjemnější frakce, což by mělo za následek horší slinovací vlastnosti [18]. Na základě tohoto zjištění nebyly dále prováděny slinovací experimenty suchou cestou tvarovaného TZ8Y.

Na slinovací křivce pro odlévané vzorky TAI (Obr. 21b) lze vidět posun slinovací křivky aktitvovaného prášku směrem k nižším slinovacím teplotám. Toto snížení je o cca 60 °C, což

odpovídá menší velikosti pórů v keramických polotovarech připravených z tohoto prášku (Obr. 20a).

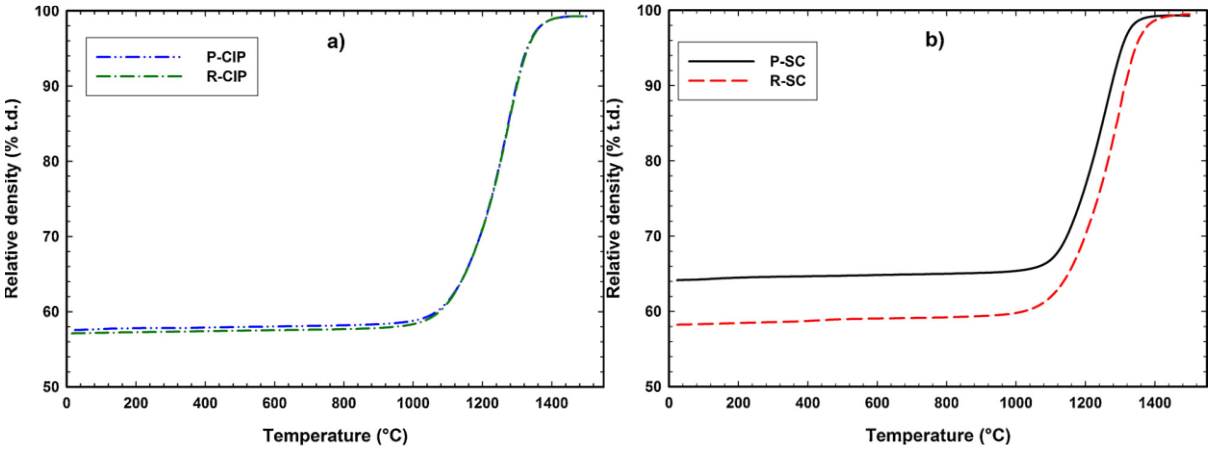

Obr. 21: Slinovací křivka referenčních (R) a fyzikálně aktivovaných (P) TAI prášků tvarovanými (a) lisováním (b) odléváním [12].

Porozimetrie plazmou aktivovaných a neaktivovaných odlévaných polotovarů materiálu TZ3Y stabilizovaných ultrazvukem (USA, USN) a kulovým mletím (BMA, BMN) je uvedena na Obr. 20b. Vysokoteplotní dilatometrie je uvedena na Obr. 22. Ze zhutňovacích křivkek lze vypozorovat, že keramické polotovary připravené z plazmou aktivovaných prášků dosahují vyšší počáteční hustoty, ale ve vysokých teplotách se již zhutňovací křivky překrývají.

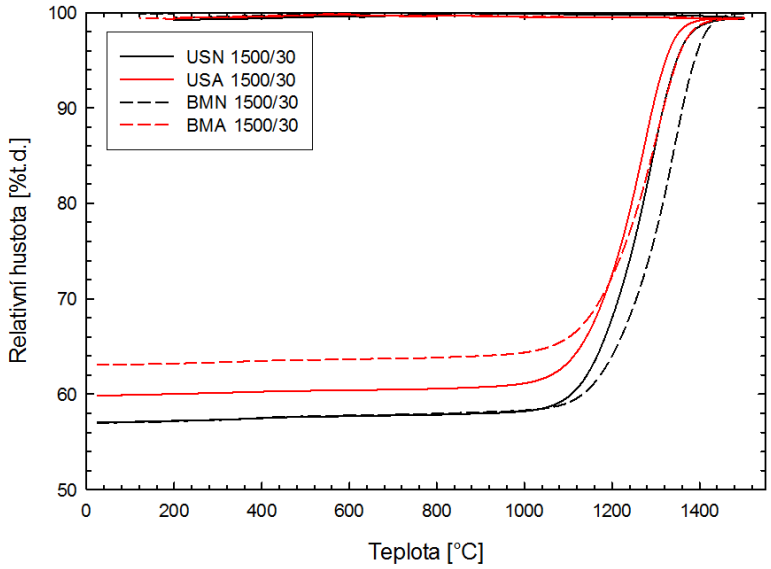

Obr. 22: Slinovací křivky pro materiál TZ3Y plazmou aktivovaný (A) i neaktivovaný (N), stabilizovaný ultrazvukem (US), nebo kulovým mletím (BM) [73].

Obr. 23 uvádí slinovací trajektorii odlévaného TAI za použití referenčního a oplazmovaného prášku. Z grafu lze pozorovat, že i když jednotlivé slinovací trajektorie začínají spolu v nižších husotách, tak od hodnot cca 98,5 %t.h. se začínají jednotlivé trajektorie od sebe odklánět. Zatímco u plazmou aktivovaných materiálů se průměrná velikost zrn zvětšuje jen pozvolna, u referenčních vzorků dochází k výraznému zvětšení průměrné velikosti zrn. Při porovnání vzorků s hutotou 99,5 %t.h., vzorek R dosahuje referenční vzorek velikosti zrn 1,15 μm a plazmou upravený vzorek 0,68 μm. Fyzikální aktivace TAI pomocí plazmové aktivace tedy vedla ke snížení výsledné velikosti zrn při hustotě 99,5 %t.h. o faktor 1,7 [12].

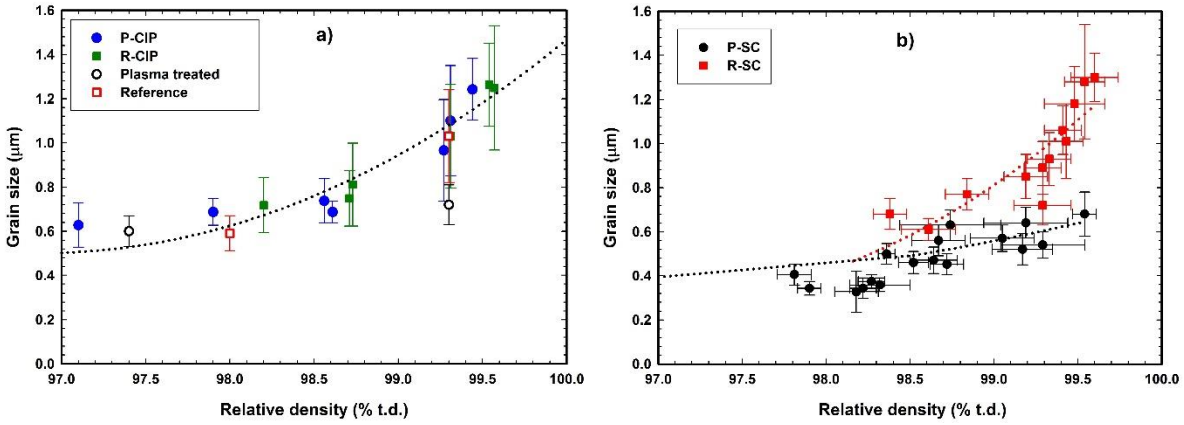

Obr. 23: Slinovací trajektorie pro plazmou aktivovaný (P) i referenční (R) materiál TAI připravený a) lisováním a b) odléváním s vloženou referenční hodnotou z literatury [23].

Obr. 24 uvádí výsledné slinovací trajektorie pro materiál TZ3Y. U obou druhů stabilizace (ultrazvukem i mletím) lze pozorovat pouze malé rozdíly mezi velikostí zrn plazmou aktivovaných a neaktivovaných vzorků. Jednotlivé směrodatné odchylky se dokonce překrývají, není tedy možno statisticky významně prokázat pozitivní vliv plazmové aktivace na výslednou mikrostrukturu materiálu TZ3Y [12].

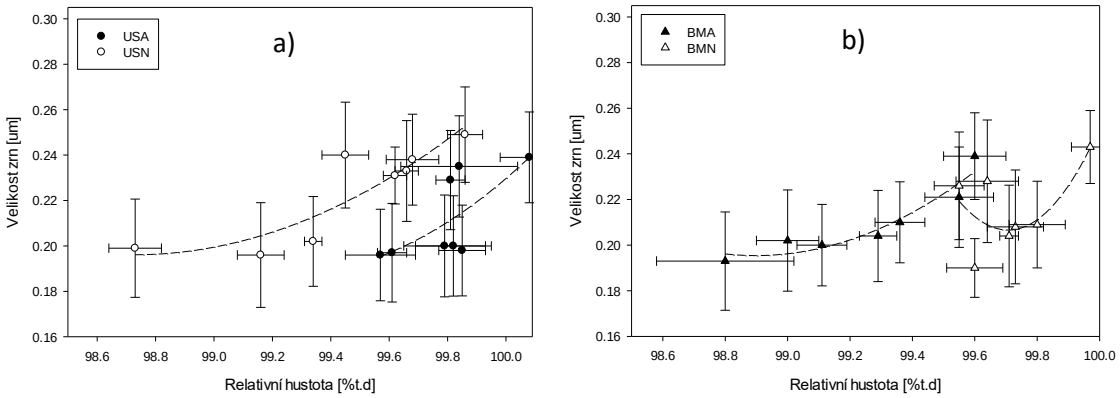

Obr. 24: Slinovací trajektorie pro plazmou aktivovaný (A) a referenční (N) materiál Z3Y a) stabilizovaný ultrazvukem, b) kulově mletý.

Závěr kapitoly

Aktivace keramických prášků nízkoteplotní plazmou neukázala při slinování lisováných prášků (tedy při suchém tvarování) TAI žádný vliv na slinovací chování. U prášků TAI a TZ3Y tvarovaných mokrou cestou již lze ovšem pozorovat vliv plazmové aktivace na pórovitost a hustotu připraveného keramického polotovaru. Takto připravená tělesa z materiálu TAI slinovala rychleji a výsledná velikost zrn při stejné relativní hustotě (99,5 %t.h.) byla menší o faktor 1,7. U materiálu TZ3Y nedošlo k prokázání vlivu plazmové aktivace na výslednou velikost velikosti.

Publikace uchazeče v daném tématu (tučně jsou uvedeny články, které jsou přílohou této kapitoly):

[12] POUCHLÝ, V., RAHEĽ, J., SPUSTA, T., ILČÍKOVÁ, M., PAVLIŇÁK, D., MORÁVEK, T., MACA, K., Improved micrtostructure of alumina ceramics prepared form DBD plasma activated powders*, J. Eur. Cer. Soc.*, 2019, vol. 39, 1297-1303.

[23] MACA, K., POUCHLY, V., BOCCACCINI, A. R. Sintering densification curve – a practical approach for its construction from dilatometric shrinkage data, *Sci. Sinter.*, 2008, vol. 40[2], 117-122.

5.5. Slinovací chování vrstevnatých kompozitů

Výslednou mikrostrukturu všech připravených vrstevnatých kompozitů Al_2O_3/ZrO_2 shrnuje Obr. 25. Hustota všech výsledných kompozitů přesáhla 98 %t.h.. Fotografie mikrostruktury také ukazují, že rozhraní mezi jednotlivými vrstvami je hladké, a neobsahuje žádnou významnou porozitu.

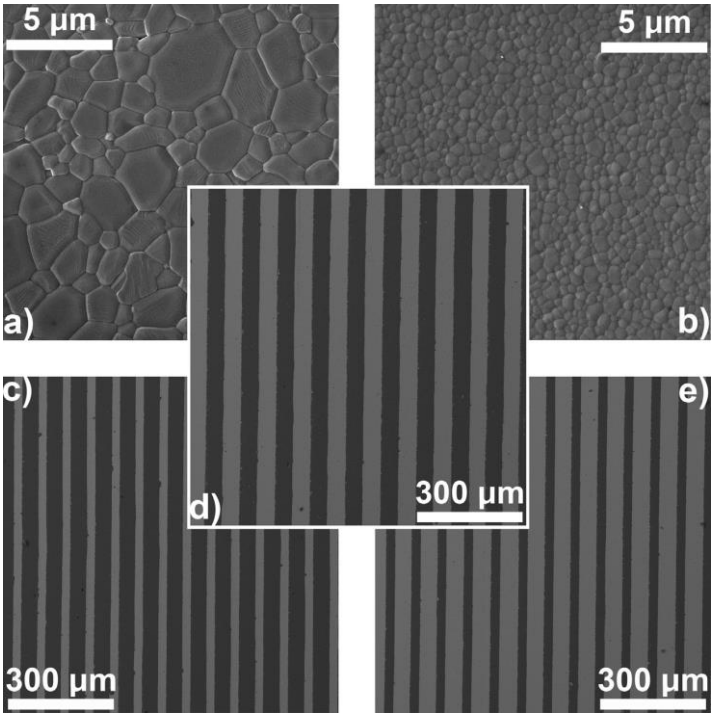

Obr. 25: Mikrostruktura jednotlivých slinutých monolitů a kompozitů: a) MAL, b) TZ3Y c) Z33 d) Z50 e) Z67 [35].

Obr. 26 ukazuje výsledky slinovacího chování monolitů materiálů A a Z a vrstevnatých kompozitů Z33, Z50 a Z67. Vzorky byly v dilatometru umístěny jak v podélném (longitudiálním), tak v příčném (transverzálním) směru (schéma měření viz. Obr. 9). Z celkového smrštění jednotlivých materiálů lze pozorovat, že v podélném směru se kompozity řídí převážně smrštěním vrstvy Al_2O_3, protože dochází k tzv. propadání vrstvy Z dovnitř kompozitu. Také příčné slinování je řízeno vrstvou A, v tomto případě díky generovanému vnitřnímu napětí. Na slinování pod napětím (tzv. constrained sintering [74]) také odkazují rychlosti smrštění (Obr. 27), kdy lze pozorovat rychlejší slinování materiálu Z oproti Al_2O_3 a silné vzájemné ovlivnění slinovacích křivek jednotlivých kompozitů.

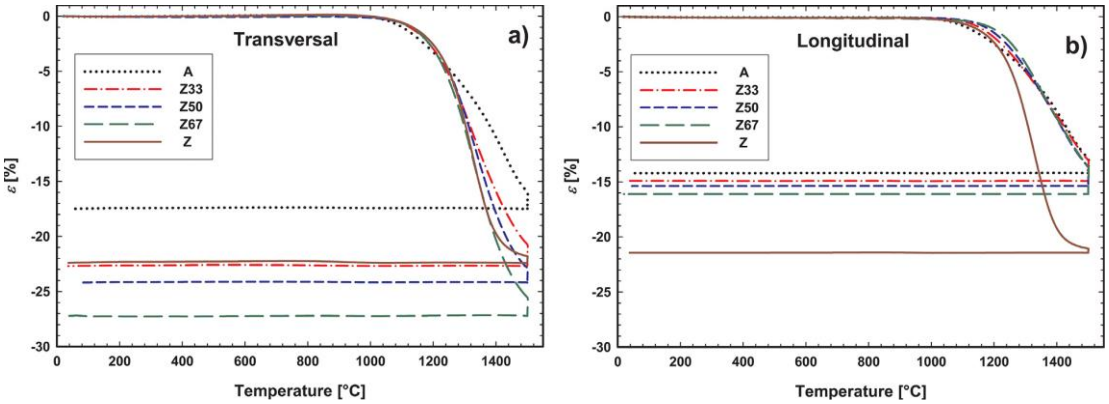

Obr. 26: Slinovací křivky v a) transversálním a b) podélném směru pro materiály A, Z, Z33, Z50 a Z67 [35].

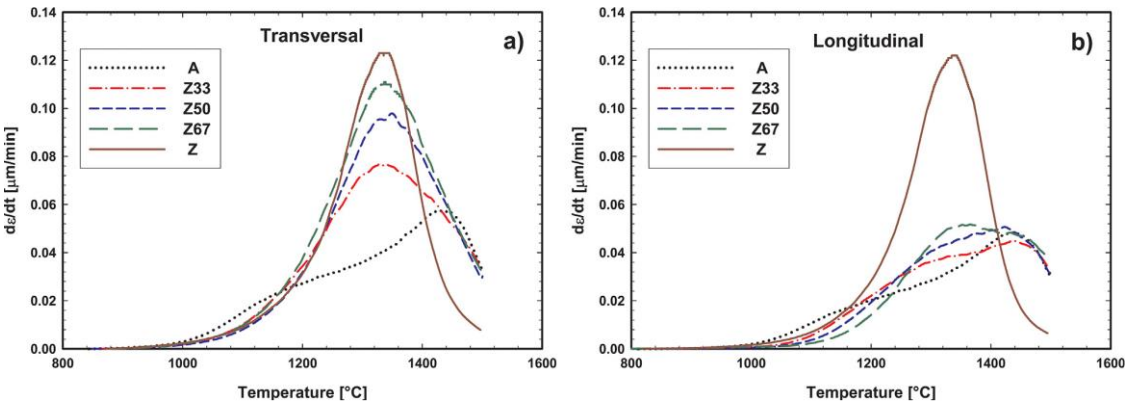

Obr. 27: Rychlost slinovacího smrštění v a) transversálním a b) podélném směru pro materiály A, Z, Z33, Z50 a Z67 [35].

Vypočtené E_A pomocí modelu Master Shrinkage Curve (rovnice 10) pro jednotlivé kompozity v příčném i podélném směru jsou zobrazeny na Obr. 28. Z výsledků vyplývá, že aktivační energie slinování kompozitu (Z50) v podélném směru je téměř dvakrát větší (960 kJ/mol), než při použití pouhého průměru aktivačních energií slinování použitých materiálů (A 672 kJ/mol, Z 564 kJ/mol). V příčném směru je ovšem aktivační energie slinování porovnatelná (A 630 kJ/mol, Z50 640 kJ/mol, Z 562 kJ/mol). V průběhu slinování tohoto kompozitu tedy docházelo k přednostnímu slinování Z vrstvy v příčném směru, která slinula dříve a nutila slinovat vrstvu A pod napětím. V příčném směru ovšem materiál napětí vyrelaxoval rozdílným smrštěním v příčném a podélném směru, což potvrdila měření slinovacích smrštění v různých směrech a fotky mikrostruktury obsahující prodloužené póry v příčném směru [35].

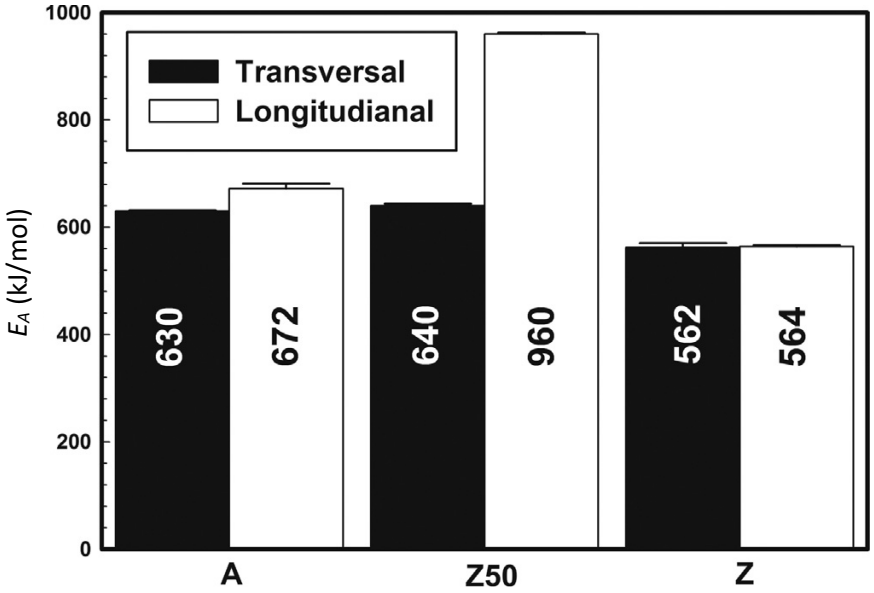

Obr. 28: Porovnání velikosti vypočtené E_A pro jednotlivé kompozity [35].

Závěr kapitoly

Al_2O_3 a ZrO_2 monolity, stejně jako jejich kompozity se třemi různými konfiguracemi, byly připraveny elektroforetickou depozicí a slinovány různými rychlostmi ohřevu v příčném i podélném směru. Analýza rychlosti slinování ukázala, že u vzorků docházelo ke slinování pod napětím, což mělo za výsledek potlačování slinování v podélném směru, kde materiál A byl slinut na vyšších teplotách, než materiál Z. Jako následek tohoto napětí poté bylo slinování materiálu Z v příčném směru urychleno. Model Master Shrinkage Curve byl aplikován na výpočet aktivační energie slinovacího procesu pro jednotlivé kompozity v obou směrech.

Publikace uchazeče v daném tématu (tučně jsou uvedeny články, které jsou přílohou této kapitoly):

[35] MACA, K., POUCHLY, V., DRDLIK, D., HADRABA, H., CHLUP, Z. Dilatometric study of anisotropic sintering of alumina/zirconia laminates with controlled fracture behaviour, *J. Eur. Ceram. Soc,* 2017, vol. 37, 4287-4295.

[34] POUCHLY, V., MACA, K. Master Sintering Curve – A Practical Approach for Its Construction, *Sci. Sinter.*, 2010, vol. 42[1], 25-32.

[23] MACA, K., POUCHLY, V., BOCCACCINI, A. R. Sintering densification curve – a practical approach for its construction from dilatometric shrinkage data, *Sci. Sinter.*, 2008, vol. 40[2], 117-122.

6. Závěry

Tato práce shrnuje poznatky o vývoji pokročilých slinovacích technik v období 2010-2022. Získané poznatky a vývojové trendy jsou popsány v jednotlivých kapitolách a vybrané články autora k těmto tématům jsou přidány jako přílohy. Samotné pokročilé slinovací techniky jsou rozděleny na popis změny slinování pomocí dopování, dále na pomalé slinovací techniky, rychlé slinovací techniky, ovlivnění slinování za pomocí změny povrchové energie a slinování vrstevnatých kompozitů. Práce taktéž obsahuje popis modelu slinování Master Sintering Curve, pro který habilitant vyvinul výpočetní software. Model MSC byl poté na OKP ÚMVI dále rozvíjen a modifikován pro popis nekonvenčních slinovacích technik: pro dvojstupňové slinování model Two-Stage Master Sintering Curve (TS-MSC), a pro slinování anizotropních materiálů, jako jsou např. vrstevnaté keramické kompozity model Master Shrinkage Curve. Jednotlivé dílčí závěry lze shrnout do následujících poznatků:

- Dopování materiálu TAI pomocí Y a Zr významně ovlivnilo slinovací proces, ale dopant MgO měl v dané koncentraci pouze nepatrný vliv na růst zrn.
- Výpočty aktivační energie slinování (E_A) ukázaly, že E_A se u materiálů TAI (dopovaného i nedopovaného), TZ3Y i TZ8Y v průběhu slinování zmenšuje. Toto snížení může být způsobeno změnou difuzního mechanizmu, nebo snížením množství mezifázových rozhraní (délky hranic zrn) v první fázi slinování, které poté brání difuzi po hranicích zrn.
- U materiálu TZ8Y bylo experimentálně a aplikací kinetických modelů smršťování a růstu zrn zjištěno, že aktivační energie růstu zrn je vyšší než aktivační energie slinovacího procesu, je tedy teoreticky možné slinovat bez růstu zrn v tzv. kinetickém okně.
- Výsledky slinování rychlostmi ohřevu 2 – 750 °C/min (realizováno v zařízení SPS, tedy za použití tlaku 50 MPa) ukazují, že při slinování rychlostí ohřevu do 50 °C/min dochází k dosažení stejné relativní hustoty (v oblasti hustoto 90%t.h. a vyšší) na nižších teplotách pro pomalejší rychlosti ohřevu, což je způsobeno delší dobou, po kterou je vzorek vystaven vyšším teplotě. U rychlostí ohřevu 50 – 450 °C/min nemá vliv rychlosti ohřevu vliv na to, při jaké teplotě dosáhne vzorek dané hustoty. Naopak při rychlosti ohřevu větší než je 450 °C/min bylo zjištěno, že vyšší rychlosti ohřevu vedou ke zhutnění při nižší teplotě vzorku, pravděpodobně kvůli preferenčnímu ohřevu hranice zrn. V přechodové oblasti rychlostí ohřevu 50 – 450 °C/min dochází zřejmě

k superpozici obou výše zmíněných jevů a vliv rychlosti ohřevu zde nemá významný vliv na to, při jaké teplotě dosáhne vzorek dané hustoty.

- Aktivace keramických prášků nízkoteplotní plazmou neukázala při slinování lisovaných (tedy při suchém tvarování) prášků TAI žádný vliv na slinovací chování. U keramických prášků tvarovaných mokrou cestou již lze ovšem pozorovat vliv plazmové aktivace na pórovitost a hustotu připraveného keramického polotovaru. Takto připravená tělesa materiálu TAI slinovala lépe a výsledná velikost zrn při stejné relativní hustotě (99,5 %t.h.) byla menší o faktor 1,7. U materiálu TZ3Y došlo k poklesu výsledné velikosti zrn při použití plazmové aktivace prášků, ale snížení bylo pouze v rámci směrodatné odchylky.
- Analýza rychlosti slinování Al_2O_3/ZrO_2 kompozitů ukázala, že u vzorků docházelo ke slinování pod napětím, což mělo za výsledek potlačování slinování v podélném směru.
- Model Master Shrinkage Curve byl aplikován na výpočet aktivační energie slinovacího procesu pro jednotlivé kompozity v obou směrech. Model potvrdil přítomnost slinovacího napětí v kompozitech.

7. Seznam použité literatury

[1] MACA, K., POUCHLY, V.,ZALUD, P. Two-Step Sintering of oxide ceramics with various crystal structures, *Journal of the European Ceramic Society,* 2010, vol. 30, pp. 583.

[2] APETZ, R.,VAN BRUGGEN, M. P. B. Transparent alumina: A light-scattering model, *Journal of the American Ceramic Society,* 2003, vol. 86, pp. 480.

[3] BAI, Y., MATOUSEK, A., TOFEL, P., BIJALWAN, V., NAN, B., HUGHES, H.,BUTTON, T. W. (Ba,Ca)(Zr,Ti)O-3 lead-free piezoelectric ceramics-The critical role of processing on properties, *Journal of the European Ceramic Society,* 2015, vol. 35, pp. 3445.

[4] CORRAL-FLORES, V., BUENO-BAQUÉS, D.,ZIOLO, R. F. Synthesis and characterization of novel $CoFe_2O_4$–$BaTiO_3$ multiferroic core–shell-type nanostructures, *Acta Materialia,* 2010, vol. 58, pp. 764.

[5] CHLUP, Z., HADRABA, H., SLABAKOVA, L., DRDLIK, D.,DLOUHY, I. Fracture behaviour of alumina and zirconia thin layered laminate, *Journal of the European Ceramic Society,* 2012, vol. 32, pp. 2057.

[6] DRDLIK, D., DRDLIKOVA, K., HADRABA, H.,MACA, K. Optical, mechanical and fractographic response of transparent alumina ceramics on erbium doping, *Journal of the European Ceramic Society* 2017, vol. 37, pp. 4265.

[7] BUCUR, R. A., BADEA, I., BUCUR, A. I.,NOVACONI, S. Dielectric, ferroelectric and piezoelectric proprieties of $GdCoO_3$ doped $(K_{0.5}Na_{0.5})NbO_3$, *Journal of Alloys and Compounds,* 2015, vol. 630, pp. 43.

[8] DRDLIKOVA, K., KLEMENT, R., HADRABA, H., DRDLIK, D., GALUSEK, D.,MACA, K. Luminescent Eu3+-doped transparent alumina ceramics with high hardness, *Journal of the European Ceramic Society,* 2017, vol. 37, pp. 4217.

[9] BOTERO, Y. L., LOPEZ-RENDON, J. E., RAMIREZ, D., ZAPATA, D. M.,JARAMILLO, F. From Clay Minerals to Al_2O_3 Nanoparticles: Synthesis and Colloidal Stabilization for Optoelectronic Applications, *Minerals-Basel,* 2020, vol. 10.

[10] GRASSO, S., SAKKA, Y.,MAIZZA, G. Electric current activated/assisted sintering (ECAS): a review of patents 1906-2008, *Sci. Technol. Adv. Mater.,* 2009, vol. 10, pp. 1.

[11] XIONG, Y., FU, Z. Y., POUCHLY, V., MACA, K.,SHEN, Z. J. Preparation of Transparent 3Y-TZP Nanoceramics with No Low-Temperature Degradation, *Journal of the American Ceramic Society,* 2014, vol. 97, pp. 1402.

[12] POUCHLY, V., RAHEL, J., SPUSTA, T., ILCIKOVA, M., PAVLINAK, D., MORAVEK, T.,MACA, K. Improved microstructure of alumina ceramics prepared from DBD plasma activated powders, *Journal of the European Ceramic Society,* 2019, vol. 39, pp. 1297.

[13] BJORK, R., FRANDSEN, H. L.,PRYDS, N. Modeling the Microstructural Evolution During Constrained Sintering, *Journal of the American Ceramic Society,* 2015, vol. 98, pp. 3490.

[14] DAVIS, J. B., KRISTOFFERSSON, A., CARLSTROM, E.,CLEGG, W. J. Fabrication and crack deflection in ceramic laminates with porous interlayers, *Journal of the American Ceramic Society,* 2000, vol. 83, pp. 2369.

[15] DRDLIK, D., SLAMA, M., HADRABA, H.,CIHLAR, J. Hydroxyapatite/zirconia-microfibre composites with controlled microporosity and fracture properties prepared by electrophoretic deposition, *Ceramics International,* 2015, vol. 41, pp. 11202.

[16] JIA, C., LI, L., LIU, Y., FANG, B., DING, H., SONG, J. N., LIU, Y. B., XIANG, K. J., LIN, S., LI, Z. W., SI, W. J., LI, B., SHENG, X., WANG, D. Z., WEI, X. D.,WU, H. Highly compressible and anisotropic lamellar ceramic sponges with superior thermal insulation and acoustic absorption performances, *Nat Commun,* 2020, vol. 11.
[17] MAYO, M. J. Processing of nanocrystalline ceramics from ultrafine particles, *International Materials Reviews,* 1996, vol. 41, pp. 85.
[18] KANG, S.-J. L. *Sintering, Densification, Grain Growth & Microstructure*; Elsevier Butterwoth-Heinemann, 2005.
[19] TRUNEC, M.,POUCHLY, V. Colloidal processing of low-concentrated zirconia nanosuspension using osmotic consolidation, *Ceramics International,* 2016, vol. 42, pp. 11838.
[20] FILIPOVIC, S., OBRADOVIC, N., PAVLOVIC, V. B., KOSANOVIC, D., MITRIC, M., MITROVIC, N., POUCHLY, V., KACHLIK, M.,MACA, K. Advantages of Combined Sintering Compared to Conventional Sintering of Mechanically Activated Magnesium Titanate, *Sci Sinter,* 2014, vol. 46, pp. 283.
[21] MACA, K., POUCHLY, V.,SHEN, Z. J. Two-Step Sintering and Spark Plasma Sintering of Al_2O_3, ZrO_2 and $SrTiO_3$ ceramics, *Integr Ferroelectr,* 2008, vol. 99, pp. 114.
[22] MACA, K., POUCHLY, V., BODISOVA, K., SVANCAREK, P.,GALUSEK, D. Densification of fine-grained alumina ceramics doped by magnesia, yttria and zirconia evaluated by two different sintering models, *Journal of the European Ceramic Society,* 2014, vol. 34, pp. 4363.
[23] MACA, K., POUCHLY, V.,BOCCACCINI, A. R. Sintering densification curve - a practical approach for its construction from dilatometric shrinkage data, *Sci Sinter,* 2008, vol. 40, pp. 117.
[24] LI, S., WEI, C. C., ZHOU, L. J., WANG, P.,XIE, Z. P. Evaporation-condensation derived silicon carbide membrane from silicon carbide particles with different sizes, *Journal of the European Ceramic Society,* 2019, vol. 39, pp. 1781.
[25] LI, J. F., WANG, K., ZHU, F. Y., CHENG, L. Q.,YAO, F. Z. (K, Na) NbO3-Based Lead-Free Piezoceramics: Fundamental Aspects, Processing Technologies, and Remaining Challenges, *Journal of the American Ceramic Society,* 2013, vol. 96, pp. 3677.
[26] WAKAI, F. Modeling and simulation of elementary processes in ideal sintering, *Journal of the American Ceramic Society,* 2006, vol. 89, pp. 1471.
[27] HANSEN, J. D., RUSIN, R. P., TENG, M. H.,JOHNSON, D. L. Combined-Stage Sintering Model, *Journal of the American Ceramic Society,* 1992, vol. 75, pp. 1129.
[28] RAHAMANN, M. N. *Sintering of Ceramics*; Taylor & Francis Group, 2008.
[29] WANG, J. D.,RAJ, R. Estimate of the Activation-Energies for Boundary Diffusion from Rate-Controlled Sintering of Pure Alumina, and Alumina Doped with Zirconia or Titania, *Journal of the American Ceramic Society,* 1990, vol. 73, pp. 1172.
[30] POUCHLY, V., HRUBY, J.,MACA, K. A Practical Approach for the Calculation of the Activation Energy of the Sintering, *Sci Sinter,* 2016, vol. 48, pp. 317.
[31] POUCHLY, V., MACA, K.,SHEN, Z. Two-stage master sintering curve applied to two-step sintering of oxide ceramics, *Journal of the European Ceramic Society,* 2013, vol. 33, pp. 2275.
[32] SU, H. H.,JOHNSON, D. L. Master sintering curve: A practical approach to sintering, *Journal of the American Ceramic Society,* 1996, vol. 79, pp. 3211.
[33] DONG, J., POUCHLY, V., BIESUZ, M., TYRPEKL, V., VILEMOVA, M., KERMANI, M., REECE, M., HU, C. F.,GRASSO, S. Thermally-insulated ultra-fast

high temperature sintering (UHS) of zirconia: A master sintering curve analysis, *Scripta Mater,* 2021, vol. 203.
[34] POUCHLY, V.,MACA, K. Master Sintering Curve - A Practical Approach to its Construction, *Sci Sinter,* 2010, vol. 42, pp. 25.
[35] MACA, K., POUCHLY, V., DRDLIK, D., HADRABA, H.,CHLUP, Z. Dilatometric study of anisotropic sintering of alumina/zirconia laminates with controlled fracture behaviour, *Journal of the European Ceramic Society,* 2017, vol. 37, pp. 4287.
[36] KASTYL, J., POUCHLY, V.,TRUNEC, M. Co-extrusion of zirconia core-shell rods with controlled porosity in the core, *Processing and Application of Ceramics,* 2018, vol. 12, pp. 231.
[37] DIANTONIO, C. B., EWSUK, K. G.,BENCOE, D. Extension of master sintering curve theory to organic decomposition, *Journal of the American Ceramic Society,* 2005, vol. 88, pp. 2722.
[38] NI, D. W., SCHMIDT, C. G., TEOCOLI, F., KAISER, A., ANDERSEN, K. B., RAMOUSSE, S.,ESPOSITO, V. Densification and grain growth during sintering of porous $Ce_{0.9}Gd_{0.1}O_{1.95}$ tape cast layers: A comprehensive study on heuristic methods, *Journal of the European Ceramic Society,* 2013, vol. 33, pp. 2529.
[39] BENNISON, S. J.,HARMER, M. P. Effect of MgO Solute on the Kinetics of Grain-Growth in Al_2O_3, *Journal of the American Ceramic Society,* 1983, vol. 66, pp. C90.
[40] GAVRILOV, K. L., BENNISON, S. J., MIKESKA, K. R.,LEVI-SETTI, R. Grain boundary chemistry of alumina by high-resolution imaging SIMS, *Acta Materialia,* 1999, vol. 47, pp. 4031.
[41] JO, W., KIM, D. Y.,HWANG, N. M. Effect of interface structure on the microstructural evolution of ceramics, *Journal of the American Ceramic Society,* 2006, vol. 89, pp. 2369.
[42] BINNER, J., VAIDHYANATHAN, B., PAUL, A., ANNAPORANI, K.,RAGHUPATHY, B. Compositional Effects in Nanostructured Yttria Partially Stabilized Zirconia, *Int J Appl Ceram Tec,* 2011, vol. 8, pp. 766.
[43] GARVIE, R. C., HANNINK, R. H.,PASCOE, R. T. Ceramic Steel, *Nature,* 1975, vol. 258, pp. 703.
[44] WITZ, G., SHKLOVER, V., STEURER, W., BACHEGOWDA, S.,BOSSMANN, H. P. Phase evolution in yttria-stabilized zirconia thermal barrier coatings studied by rietveld refinement of X-ray powder diffraction patterns, *Journal of the American Ceramic Society,* 2007, vol. 90, pp. 2935.
[45] MORITA, K., KIM, B. N., YOSHIDA, H., HIRAGA, K.,SAKKA, Y. Assessment of carbon contamination in MgAl2O4 spinel during spark-plasma-sintering (SPS) processing, *Journal of the Ceramic Society of Japan,* 2015, vol. 123, pp. 983.
[46] COLOGNA, M.,RAJ, R. Ceram building first commercial-scale flash sintering kiln, *Bulletin of American ceramic society,* 2013, vol. 92, pp. 5.
[47] SALAMON, D., MACA, K.,SHEN, Z. J. Rapid sintering of crack-free zirconia ceramics by pressure-less spark plasma sintering, *Scripta Mater,* 2012, vol. 66, pp. 899.
[48] KOCJAN, A., POUCHLY, V.,SHEN, Z. J. Processing of zirconia nanoceramics from a coarse powder, *Journal of the European Ceramic Society,* 2015, vol. 35, pp. 1285.
[49] COLOGNA, M., RASHKOVA, B.,RAJ, R. Flash Sintering of Nanograin Zirconia in < 5 s at 850 degrees C, *Journal of the American Ceramic Society,* 2010, vol. 93, pp. 3556.

[50] TODD, R. I., ZAPATA-SOLVAS, E., BONILLA, R. S., SNEDDON, T.,WILSHAW, P. R. Electrical characteristics of flash sintering: thermal runaway of Joule heating, *Journal of the European Ceramic Society,* 2015, vol. 35, pp. 1865.
[51] CALKA, A.,RADLINSKI, A. P. Universal High-Performance Ball-Milling Device and Its Application for Mechanical Alloying, *Mat Sci Eng a-Struct,* 1991, vol. 134, pp. 1350.
[52] BODISOVA, K., KLEMENT, R., GALUSEK, D., POUCHLY, V., DRDLIK, D.,MACA, K. Luminescent rare-earth-doped transparent alumina ceramics, *Journal of the European Ceramic Society,* 2016, vol. 36, pp. 2975.
[53] FRIDMAN, A. A. *A Plasma Chemistry*; Cambridge University Press, 2008.
[54] HILLMAN, C., SUO, Z. G.,LANGE, F. F. Cracking of laminates subjected to biaxial tensile stresses, *Journal of the American Ceramic Society,* 1996, vol. 79, pp. 2127.
[55] CAI, P. Z., GREEN, D. J.,MESSING, G. L. Constrained densification of alumina/zirconia hybrid laminates .1. Experimental observations of processing defects, *Journal of the American Ceramic Society,* 1997, vol. 80, pp. 1929.
[56] HADRABA, H., KLIMES, J.,MACA, K. Crack propagation in layered Al2O3/ZrO2 composites prepared by electrophoretic deposition, *Journal of Materials Science,* 2007, vol. 42, pp. 6404.
[57] GHILLANYOVA, K., GALUSEK, D., PETRAK, M., MADEJOVA, J., BERTOTI, I., SZEPVOLGYI, J.,SAJGALIK, P. The influence of ageing on consolidation and sinterability of a sub-micron alumina powder, *Powder Technol,* 2011.
[58] BERNARD-GRANGER, G.,GUIZARD, C. Apparent activation energy for the densification of a commercially available granulated zirconia powder, *Journal of the American Ceramic Society,* 2007, vol. 90, pp. 1246.
[59] KANG, S.-J. L.,JUNG, Y.-I. Sintering kinetics at final stage sintering: model calculation and map construction, *Acta Materialia,* 2004, vol. 52, pp. 4573.
[60] SUMITA, S. A historical view of Al2O3 sintering with pore elimination, 1996, vol. 4, pp. 103.
[61] SONG, X. C., LU, J., ZHANG, T. S.,MA, J. Two-Stage Master Sintering Curve Approach to Sintering Kinetics of Undoped and Al(2)O(3)-Doped 8 Mol% Yttria-Stabilized Cubic Zirconia, *Journal of the American Ceramic Society,* 2011, vol. 94, pp. 1053.
[62] SETHI, G., PARK, S. J., JOHNSON, J. L.,GERMAN, R. M. Linking homogenization and densification in W-Ni-Cu alloys through master sintering curve (MSC) concepts, *Int J Refract Met H,* 2009, vol. 27, pp. 688.
[63] MCCUNE, R. C., DONLON, W. T.,KU, R. C. Yttrium Segregation and Yag Precipitation at Surfaces of Yttrium-Doped Alpha-Al_2O_3, *Journal of the American Ceramic Society,* 1986, vol. 69, pp. C196.
[64] CAWLEY, J. D.,HALLORAN, J. W. Dopant Distribution in Nominally Yttrium-Doped Sapphire, *Journal of the American Ceramic Society,* 1986, vol. 69, pp. C195.
[65] CHEN, P. L.,CHEN, I. W. Sintering of fine oxide powders .1. Microstructural evolution, *Journal of the American Ceramic Society,* 1996, vol. 79, pp. 3129.
[66] POUCHLY, V.,MACA, K. Master sintering curves of two different alumina powder compacts, *Processing and Application of Ceramics,* 2009, vol. 3, pp. 4.
[67] BODISOVA, K., GALUSEK, D., SVANCAREK, P., POUCHLY, V.,MACA, K. Grain growth suppression in alumina via doping and two-step sintering, *Ceramics International,* 2015, vol. 41, pp. 11975.
[68] POUCHLY, V.,MACA, K. Sintering kinetic window for yttria-stabilized cubic zirconia, *Journal of the European Ceramic Society,* 2016, vol. 36, pp. 2931.

[69] CHEN, I. W.,WANG, X. H. Sintering dense nanocrystalline ceramics without final-stage grain growth, *Nature,* 2000, vol. 404, pp. 168.
[70] WANG, L., POUCHLY, V., MACA, K., SHEN, Z.,XIONG, Y. Intensive particle rearrangement in the early stage of spark plasma sintering process, *Journal of Asian Ceramic Societies,* 2015, vol. 3, pp. 183.
[71] KOCJAN, A., LOGAR, M.,SHEN, Z. J. The agglomeration, coalescence and sliding of nanoparticles, leading to the rapid sintering of zirconia nanoceramics, *Sci Rep-Uk,* 2017, vol. 7, pp.
[72] KIM, S. W., KIM, S. G., JUNG, J. I., KANG, S. J. L.,CHEN, I. W. Enhanced Grain Boundary Mobility in Yttria-Stabilized Cubic Zirconia under an Electric Current, *Journal of the American Ceramic Society,* 2011, vol. 94, pp. 4231.
[73] KLEVETOVÁ, T. Vliv plazmové aktivace keramických částic na technologii přípravy a vlastnosti pokročilých keramických materiálů, *Diplomová práce,* 2019, vol. vedoucí Václav Pouchlý.
[74] ARIAS-MAYA, L. S. Free and constrained sintering of 3-mol % yttria stabilised zirconia, *Dyna-Colombia,* 2014, vol. 81, pp. 158.

Available online at www.sciencedirect.com

SciVerse ScienceDirect

Journal of the European Ceramic Society 33 (2013) 2275–2283

www.elsevier.com/locate/jeurceramsoc

Two-stage master sintering curve applied to two-step sintering of oxide ceramics

Vaclav Pouchly [a,c], Karel Maca [a,*], Zhijian Shen [b,d]

[a] CEITEC BUT, Brno University of Technology, Technicka 10, 616 00 Brno, Czech Republic

[b] Department of Materials and Environmental Chemistry, Arrhenius Laboratory, Stockholm University, S-106-91 Stockholm, Sweden

Available online 21 February 2013

Abstract

Tetragonal (3 mol% Y_2O_3) and two cubic zirconia (8 mol% Y_2O_3) as well as alumina green bodies were used for the construction of the Master Sintering Curve (MSC) created from sets of constant-rate-of-heating (CRH) sintering experiments. The activation energies calculated according to the MSC theory were 770 kJ/mol for Al_2O_3, 1270 kJ/mol for t-ZrO_2, 620 kJ/mol and 750 kJ/mol for c-ZrO_2. These values were verified by an alternative approach based on an analysis of the densification rate in the intermediate sintering stage. The MSCs established from the Two-Step Sintering (TSS) experiments showed at high densities a significant deflection from those constructed from the CRH experiments. This deflection was explained by lower sintering activation energy in the closed porosity stage. A new two-stage MSC model was developed to reflect the change in sintering activation energy and to describe TSS. The efficiency of TSS of four materials under investigation was correlated with their activation energies during the final sintering stage.

Keywords: Zirconia; Alumina; Sintering; Master sintering curve; Activation energy

1. Introduction

Zirconia is a polymorphic ceramic material with three different crystallographic phases: monoclinic (at room temperature), tetragonal (above 1170 °C) and cubic (above 2370 °C). The transformation of the tetragonal to the monoclinic phase is associated with an increase of volume causing cracking during cooling from the sintering temperature in polycrystalline dense bulks, which disables pure zirconia to be effectively manufactured. Common zirconia is therefore doped with Y_2O_3, CaO, Sc_2O_3 and other oxides to stabilize its tetragonal or cubic phase. Owing to a transformation strengthening mechanism the polycrystalline tetragonal zirconia (t-ZrO_2) reveals the highest fracture toughness among advanced ceramics and has been widely used in structural applications.[1] The stabilization of cubic zirconia (c-ZrO_2) by a higher amount of dopants strongly increases the number of oxygen vacancies in the lattice. Therefore, stabilized polycrystalline c-ZrO_2 is ionic conductive and is often used as oxygen sensor[2,3] and solid electrolyte in fuel cells.[4,5] Alumina exhibits good mechanical, optical, electric-insulating and biologically inert properties. In polycrystalline form it has found many applications, e.g. as refractories, crucibles, spark-plug insulators, hip replacements and transparent armours.[6–8]

To improve the mechanical and optical properties of polycrystalline ceramics, it is desirable to achieve microstructures with nearly full density and fine grains with homogenous distribution. Such microstructure refinement has revealed advantages in increasing of hardness,[9] flexural strength,[10] wear resistance[11] and optical transparency of bulk ceramics.[12]

Along with powder synthesis, consolidation and shaping of the ceramic green bodies, the optimization of the sintering process has been in the focus of attention during the last couple of decades.[13,14]

One of the promising methods for the description and prediction of sintering is the concept of Master Sintering Curve (MSC).[15] The MSC theory is derived from the combined stage sintering model proposed by Hansen and

* Corresponding author. Tel.: +420 541143344; fax: +420 541143202.
E-mail addresses: pouchly@fme.vutbr.cz (V. Pouchly), karel.maca@ceitec.vutbr.cz (K. Maca), shen@mmk.su.se (Z. Shen).
[c] Tel.: +420 541143368; fax: +420 541143202.
[d] Tel.: +46 8 162388.

0955-2219/$ – see front matter © 2013 Elsevier Ltd. All rights reserved.
http://dx.doi.org/10.1016/j.jeurceramsoc.2013.01.020

co-workers.[16] This model relates the linear shrinkage rate of powder compact to microstructural, material and thermodynamic parameters:

$$-\frac{dL}{Ldt} = \frac{\gamma\Omega}{kT}\left(\frac{\Gamma_v D_v}{G^3} + \frac{\Gamma_b \delta D_b}{G^4}\right), \quad (1)$$

where, γ is the surface energy, Ω is the atomic volume, k is the Boltzmann constant, T is the absolute temperature, G is the mean grain size, t is the time, L is the sample length, D_v and D_b are, respectively, the coefficients of volume and grain boundary diffusion, δ is the thickness of grain boundary. Γ_v and Γ_b represents scaling parameters that relate various geometric features, the driving force for sintering, and the mean diffusion distance to the grain size.[17]

Two diffusion mechanisms (grain boundary and volume diffusion) are involved in this model. If only one diffusion mechanism dominates the whole sintering process (grain boundary or volume diffusion) and the microstructure evolution (described by G and Γ) is a function only of density (regardless of thermal history), Eqs. (1) to (2) can then be rearranged:

$$\frac{k}{\gamma\Omega\delta D_0}\int_{\rho_0}^{\rho}\frac{(G(\rho))^n}{3\rho\Gamma(\rho)}\,d\rho = \int_0^t \frac{1}{T}\exp\left(-\frac{E_A}{RT}\right)dt, \quad (2)$$

where, E_A is the activation energy of the sintering process, D_0 is the diffusion constant, ρ is the density of the sample, and parameter n has the value 3 (for volume diffusion) or 4 (for grain boundary diffusion). The relationship between the right-hand side of Eq. (2) (denoted θ) and density ρ is called MSC. The MSC is unique for a given powder prepared and shaped by the same technology. For a practical construction of MSC a few dilatometric sintering experiments with different thermal history are needed. If the concept of MSC is correct, there must exist one activation energy for which the functions $\rho = f(\theta)$ calculated for all thermal histories converge onto a single (master) curve. In practice, the construction of MSC needs repeated numerical calculations, which are user-unfriendly. Therefore, we developed simple software that significantly simplifies the creation of MSC.[18]

The concept of MSC was originally designed on the assumption that one diffusion mechanism dominates the whole sintering process, and that the microstructure evolution (in particular the grain size) is only a function of the reached density irrespective of the heating schedule used. Contrary to this assumptions, the concept of Two-Step Sintering (TSS)[19,20] claims that with an appropriate choice of the heating profile it is possible to decrease the grain size of sintered samples compared to the conventional Single Step Sintering (SSS = CRH + dwell). TSS consists in heating the sample in two steps. In the first step the sample is heated to a temperature guaranteeing the suppression of subcritical pores (usually at relative densities higher than 80% t.d.), then cooled down several tens of degrees and held at this lower temperature for an extended time, usually a few hours. Lowering the sintering temperature leads to the suppression of grain growth and the prolongation of the dwell at lower temperature and provides enough heating energy for promoting full densification. The TSS concept has so far been tested in many ceramic systems but with different success. For example, in case of yttria the grain size was decreased by a factor of 2.3,[19] in case of alumina by a factor of 1.3[21] or 1.25,[22] in case of t-ZrO_2 by a factor 2.5[23] or 1.1,[22] in case of c-ZrO_2 by a factor of 7[24] or 2[22] and in case of $SrTiO_3$ by a factor of 1.6.[25] Although the efficiency of TSS is different for different materials, its general validity would imply that the original MSC concept cannot be used in the case of TSS. Recently, various authors have shown that sintering activation energy is not constant for the whole sintering process, and in most cases the activation energy in the final sintering stage is lower than that in the early stages.[26–28]

The main goal of this work is to modify the MSC concept into two-stage master sintering curve concept suitable for describing the TSS process. This achievement would contribute to the explanation of the different efficiency of the TSS process experimentally observed in different materials.

2. Experimental

2.1. Materials

Four types of commercially available ceramic powders were used. The details of these powders are given in Table 1. The particle size D_{BET} was calculated from the specific surface area data established in case of alumina powder by nitrogen absorption (BET method, ChemBet 3000, Quantachrome, USA) while in the case of zirconia powders the data were provided by the producer. The theoretical densities used for calculating the average particle size as well as for calculating the relative densities were 3.99 g cm^{-3} for TAI, 6.08 g cm^{-3} for Z3Y, and 5.99 g cm^{-3} for Z8Y and Z8YSB (see Table 1 for the meaning of abbreviations).

2.2. Preparation of ceramic green bodies

Discs of 30 mm in diameter and ca. 5 mm in height were prepared from the above powders by cold isostatic pressing (CIP). Pressing was carried out in an isostatic press (Autoclave Engineering, Inc., USA) at a pressure of 300 MPa with a dwell time of 5 min. The CIPed samples were pre-sintered at 800 °C/1 h, then cut and ground to the shape of prisms of ca. 4 mm × 4 mm × 15 mm.

2.3. Sintering of ceramic bodies and constructing the MSC

All samples were sintered in a high-temperature dilatometer (L70/1700, Linseis, Germany). A proper evaluation of dilatometric measurements and the creation of the densification curves were performed by a methodology described elsewhere.[29]

To construct MSC, heating rates of 2, 5, 10, and 20 °C/min were used. Various combinations of used heating rates and dwell times are summarized in Table 2. In the case of TSS, the temperatures of the first and the second step were chosen according to our previous experiments with these powders.[22] The calculation of MSC was performed with the help of an automatic procedure[18] which uses a newly proposed criterion, called Mean Perpendicular Curves Distance (MPCD), for estimating the best overlap of individual curves.

Table 1
Specification of ceramic materials used.

Powder	Producer	Grade	Abbreviation	D_{BET} (nm)
Al_2O_3	Taimei Chemicals, Japan	Taimicron TM-DAR	TAI	100
ZrO_2 (+3 mol% Y_2O_3)	Tosoh Corporation, Japan	TZ-3YB	Z3Y	60
ZrO_2 (+8 mol% Y_2O_3)	Tosoh Corporation, Japan	TZ-8Y	Z8Y	70
ZrO_2 (+8 mol% Y_2O_3)	Tosoh Corporation, Japan	TZ-8YSB	Z8YSB	140

Table 2
Heating schedules used and final densities obtained.

Material	Heating rate (°C/min)	SSS (°C/min)	TSS (°C/°C/h)	ρ_{rel} (%t.d.)	*s*/*n* (%t.d./–)
TAI	2	1500/0		99.67	0.07/12
	5	1500/0		99.63	0.10/09
	10	1500/0		99.59	0.10/09
	20	1500/0		99.59	0.14/12
	5		1328/1228/15	99.22	0.07/12
Z3Y	2	1500/0		99.92	0.10/12
	5	1500/0		99.92	0.09/15
	10	1500/20		99.99	0.04/12
	20	1500/20		99.92	0.11/09
	5		1350/1300/10	99.51	0.16/12
	5		1330/1275/15	99.23	0.07/12
Z8Y	2	1500/0		99.62	0.06/09
	5	1500/0		99.54	0.05/09
	10	1500/10		99.63	0.04/09
	20	1500/60		99.72	0.10/09
	5		1330/1270/15	99.83	0.08/09
Z8YSB	2	1500/0		98.81	0.07/12
	5	1500/0		98.08	0.05/12
	10	1500/0		97.27	0.07/12
	20	1500/0		96.41	0.08/12
	5		1440/1340/10	99.26	0.09/12
	5		1440/1325/10	99.25	0.06/09

Note: *s* is standard deviation, *n* is number of measurements.

The final density of samples after sintering was measured by the Archimedes method with distilled water as the liquid medium (EN623-2). At least 9 measurements were performed for each sample.

2.4. Calculation of sintering activation energy from CRH experiments

For comparison, the activation energy of the sintering process was also calculated using a different approach. Wang and Raj[30] expressed the densification rate by the following equation (3):

$$\frac{d\rho}{dt} = A\frac{e^{-E_A/RT}}{T}\frac{f(\rho)}{G^n}, \tag{3}$$

where,

$$A = \frac{C\gamma V^{2/3}}{R} \tag{4}$$

In Eqs. (3) and (4) C is a constant, V is the molar volume, and $f(\rho)$ is a function of density alone. Other variables have the same meaning as in Eqs. (1) and (2). By modifying Eq. (3) we obtain:

$$\ln\left(T\frac{d\rho}{dT}\frac{dT}{dt}\right) = -\frac{E_A}{RT} + \ln(f(\rho)) + \ln A - n\ln G. \tag{5}$$

At a constant value of ρ and G the plot of the left side of Eq. (5) in dependence on $1/T$ would be a line whose slope gives the value of E_A. The assumption of no grain growth (G = const.) means that this model can be applied only in the early and intermediate stage of sintering; therefore we compared the densification rates ($d\rho/dt$) at the constant value of relative density 70% t.d. for all used heating rates (dT/dt). This density is definitely inside the intermediate stage of sintering, where grain growth is limited.[13,31] For these calculations we utilized sets of experimental data which were previously used for the construction of MSCs.

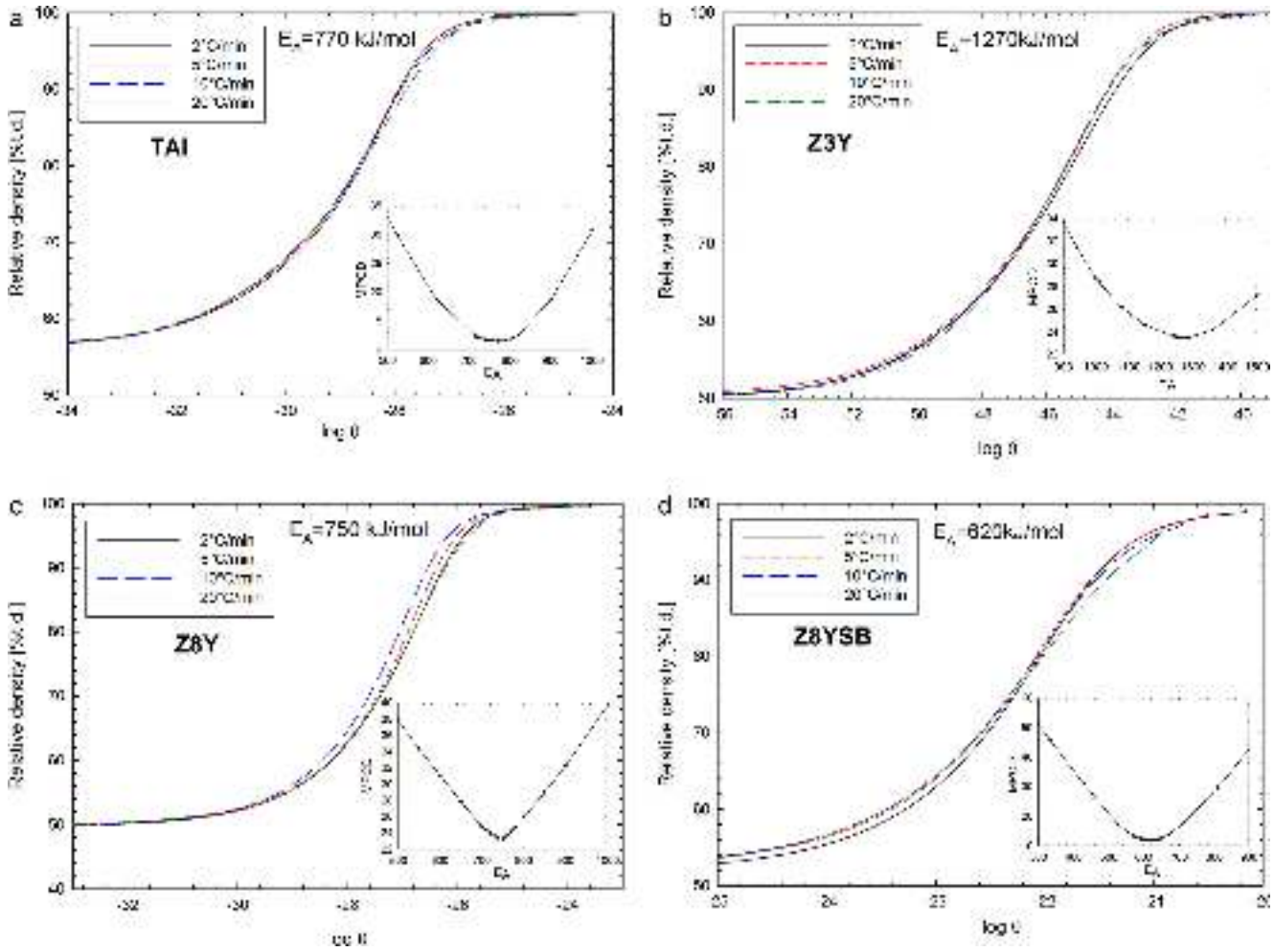

Fig. 1. (a) MSC and MPCD (inset) of TAI calculated from SSS experiments. (b) MSC and MPCD (inset) of Z3Y calculated from SSS experiments. (c) MSC and MPCD (inset) of TZ8Y calculated from SSS experiments. (d) MSC and MPCD (inset) of Z8YSB calculated from SSS experiments.

3. Results and discussion

3.1. Activation energy of sintering process calculated from MSC concept

Table 2 shows the heating schedules of all SSS experiments as well as the final densities of the TAI, Z3Y, Z8Y, and Z8YSB samples. It can be seen that all materials were sintered to a final relative density higher than 99%t.d. Since the sintering was performed in the high-temperature dilatometer, it was possible to construct MSCs of all materials (see Fig. 1(a)–(d)). The Mean Perpendicular Curves Distance as a function of activation energy (insets of Fig. 1(a)–(d)) contained in all cases a single minimum, and the established activation energies were 770, 1270, 750 and 620 kJ/mol for TAI, Z3Y, Z8Y and Z8YSB, respectively. The E_A established from the MSC concept is commonly referred to as apparent activation energy for the mechanism that controls sintering.[32] The published values of sintering activation energies vary very strongly (Al_2O_3: 342–1064 kJ/mol[33,34]; t-ZrO_2 310–935 kJ/mol[26]; c-ZrO_2 94–680 kJ/mol).[27,35] This could be caused by the different experimental methods, level of impurities, temperature range, and also by the model applied. Therefore we tried to verify acquired activation energies also using a different approach.

3.2. Activation energy of sintering process calculated from CRH experiments

The MSCs presented in the previous paragraph were established from SSS experiments, implying that each material was heated using several constant heating rates. These measurements can therefore be used also for the calculation of activation energy from the densification rate (see Section 2.4). The dependence of the natural logarithm of the product of temperature T, densification rate $d\rho/dt$ and heating rate dT/dt (all taken at a relative density of 70%t.d.) on $1/T$ is given in Fig. 2. It can be seen that the dependence is (according to the model) linear, and the activation energies of sintering calculated from the line slopes were 825 kJ/mol for TAI, 1220 kJ/mol for Z3Y, 750 kJ/mol for Z8Y, and 620 kJ/mol for Z8YSB. These calculated activation energies are in good agreement with the activation energies calculated from the MSC concept (see also Table 3).

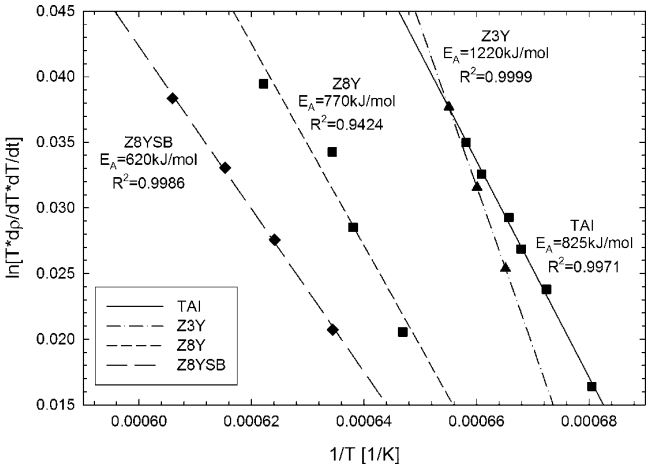

Fig. 2. Sintering activation energies of TAI, Z3Y, Z8Y and Z8YSB established at a relative density of 70%t.d. from CRH experiments.

Table 3
Summary of activation energies obtained in this work and efficiency of TSS.

Material	E_{A1} (kJ/mol)	E_{A2} (kJ/mol)	E_{A3} (kJ/mol)	G_{SSS}/G_{TSS}
TAI	825	770	570	1.25[22]
Z3Y	1220	1270	650	1.1[22]
Z8Y	770	750	460	2.1[a]
Z8YSB	620	620	430	2.0[22]

Note: E_{A1}: activation energy established from densification rate at 70%t.d.
E_{A2}: activation energy established by MSC in low-temperature region.
E_{A3}: activation energy established by MSC in high-temperature region.
G_{SSS}/G_{TSS}: efficiency of TSS (ratio of grain sizes after SSS and TSS).
[a] Unpublished results

3.3. MSC applied to TSS experiments

As the next step, we incorporated TSS heating profiles into MSCs created from SSS experiments. It was tested whether the TSS regimes will fall into the same (master) curve. It can be seen from Fig. 3(a)–(d) that the TSS regimes had the same progression during the first step of TSS, but they showed considerable deflection during the second step of TSS.

These observations revealed that the original MSC concept cannot be used directly for describing the TSS experimental results. This is not surprising because the results published so far have shown that TSS leads to a refined microstructure (in comparison with the conventional SSS). Obviously, for the TSS process one of the basic assumptions of the MSC concept is not fulfilled, namely the assumption that for a given compact the resulting grain size is the function of density alone, irrespective of the heating profile used.

Since MSC is a very useful tool, e.g. for sintering prediction,[18,36,37] it is desirable to modify the MSC concept such that it can describe also TSS. One possible way how to modify MSC was proposed by Robertson et al.[38]. They suggest that the MSC equation should be modified by taking into account the grain growth (6):

$$\delta = \frac{1}{G}\int_0^t \frac{1}{T}\exp\left(-\frac{E_A}{RT}\right)\,dt, \quad (6)$$

where, δ is the modified θ, and G is the grain size.

Literature data show that TSS regimes are favorable for obtaining a smaller grain size in comparison with the constant heating rate schedule, i.e. smaller values of G will change δ to higher values. However, in this work we obtained lower θ values using the TSS regime (see Fig. 3(a)–(d)). In addition, our previous results with the same powders[22] showed that the difference in final microstructure (including grain sizes) varied with the used powder. The efficiency (defined as G_{SSS}/G_{TSS}) of TSS was 1.1, 1.25, 2.1 and 2.0 for Z3Y, TAI, Z8Y and Z8YSB, respectively (see Table 3). According to these results, we expected that a significant deviation might be observed only in the case of Z8Y and Z8YSB, but it appears in all the studied materials.

Another way of upgrading the MSC concept is to accept the experimental evidence that there might be more than one diffusion mechanism in action during the whole sintering process, i.e. different sintering mechanisms may be active in different sintering stages. Song at al.[27] proposed a solution in dividing MSC into high-density and low-density regions. Kiani et al.[39] separated the MSC of stainless steel even into three parts. In these two attempts to split MSC the fitting of experimental data by a numerical sigmoidal function was used.[40] In this work we tried to divide the θ function into two separate parts (with different activation energies) according the following formula (7):

$$\theta = \int_0^{t<t_1} \frac{1}{T}\exp\left(-\frac{E_{A1}}{RT}\right)\,dt + \int_{t_1}^{t} \frac{1}{T}\exp\left(-\frac{E_{A2}}{RT}\right)\,dt, \quad (7)$$

where t_1 is the time when the second step of TSS is applied.

With this model (referred to as two-stage master sintering curve and abbreviated to TS-MSC henceforth) we re-evaluated the results of our experiments performed with the TAI, Z3Y, Z8Y and Z8YSB ceramics. While the activation energies in the low-temperature region remained practically unchanged, the application of the TS-MSC concept in the final sintering stage ($t > t_1$) revealed a significant decrease of sintering activation energies for all investigated materials (see Fig. 4(a)–(d)). A summary of the activation energies obtained in this work is given in Table 3.

The decrease of sintering activation energy during sintering was already presented in the literature by Bernard-Granger and Guizard,[26] who divided the densification of t-ZrO_2 into low-density and high-density regions. They suggested that below 70%t.d. the appearance of point defects was limited, and therefore the sintering activation energy was quite high – 935 kJ/mol. When density increased above 90%t.d, the activation energy decreased to 310 kJ/mol. They referred this decrease of activation energy to grain boundary diffusion of Zr^{4+}. In this work we obtained at high-density region sintering activation energy of t-ZrO_2 650 kJ/mol which is similar to reported activation energy of grain boundary diffusion for t-ZrO_2 ranging from 610 to 650 kJ/mol.[41,42]

In case of c-ZrO_2 analogous decrease of activation energies during sintering was observed by Song et al.[27] They worked with same powder as it was used in this work (Z8Y). They separated the MSC curve into two parts: with activation energies 730 kJ/mol at density range 50–60%t.d. and 580 kJ/mol at densities 60–92%t.d. They attributed high activation energy

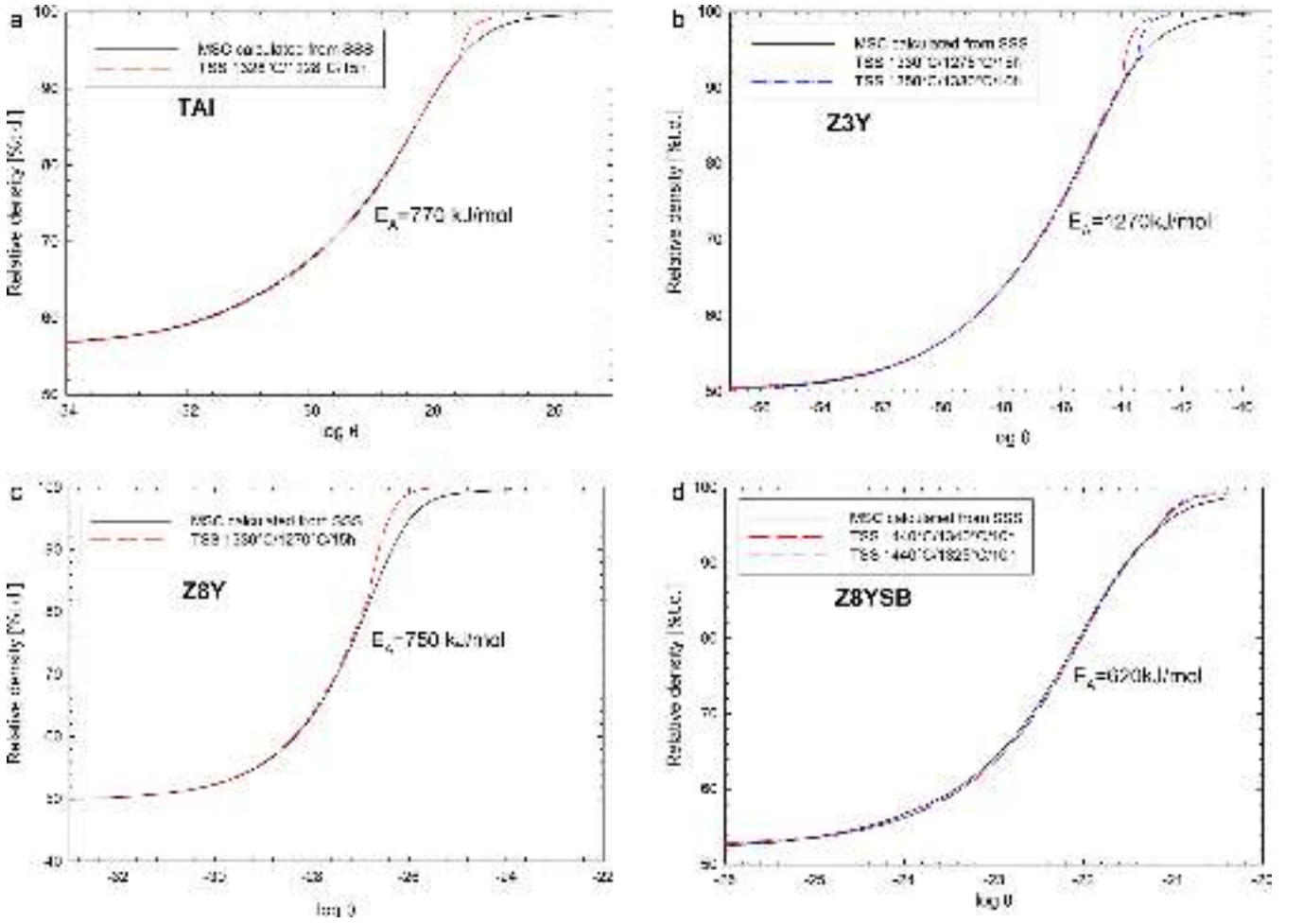

Fig. 3. (a) MSC of TAI constructed from SSS and TSS experiments. (b) MSC of Z3Y constructed from SSS and TSS experiments. (c) MSC of Z8Y constructed from SSS and TSS experiments. (d) MSC of Z8YSB constructed from SSS and TSS experiments.

established in low-density region to the effect of surface diffusion and/or limited point defect formation. Their determined activation energy in this region is comparable with our estimated value 750 kJ/mol. Activation energy established in our work for high density region (460 kJ/mol) is the same as it was reported by Taylor et al. for lattice diffusion in c-ZrO_2.[43]

It seems to be that the higher sintering activation energy in low-density region is a consequence of surface diffusion acting at low temperatures and hindering the densification. This problem can be overcome with using of external mechanical energy (so-called pressure-assisted sintering). We observed big drop of sintering activation energy of t-ZrO_2 at low densities in case of SPS sintering. This will be the topic of the following paper.

It is interesting that all SSS regimes exhibited good overlap of MSCs in the final sintering stage with higher as well as lower activation energy (see Fig. 5). This indicates small sensitivity of MSC to the value of activation energy at high densities. The necessity of using a lower sintering activation energy in the final sintering stage was revealed here using the TSS heating profile, which is quite different from conventional SSS profile. The lower activation energy during sintering in the final stage of sintering is in good agreement with the TSS concept. The authors of TSS assume[19] that even after a temperature decrease in the second sintering step, the densification mechanism (e.g. grain boundary diffusion) remains active. In this regard, a low sintering activation energy enables densification even at low temperatures. The problem can occur when full density is needed. Many researchers[20–23] did not achieve with TSS such high densities as with SSS even after dwell times in the order of tens of hours. The low temperature in the final sintering stage did not probably allow the elimination of remaining supercritical pores without grain growth.

As mentioned above, the same ceramic materials (shaped by exactly the same technology) as in this research has recently been studied from the point of view of TSS efficiency. It was found that the highest efficiency of TSS was reached with both c-ZrO_2 samples and the lowest with t-ZrO_2 (see Table 3). It is interesting that the efficiency of TSS decreased with increasing sintering activation energy in the final sintering stage (see Fig. 6). The literature review shows the activation energy of grain growth to be in the range of 420–690 kJ/mol[44,45] for alumina, 540–584 kJ/mol[46,47] for t-ZrO_2 and 252–400 kJ/mol[48,49] for c-ZrO_2. These values are similar to the activation energy of the final stage of sintering, and therefore sintering can proceed but the grain growth is inhibited (the conditions of so-called "kinetic window"[19,21,50]). It should be noted that the literature values of

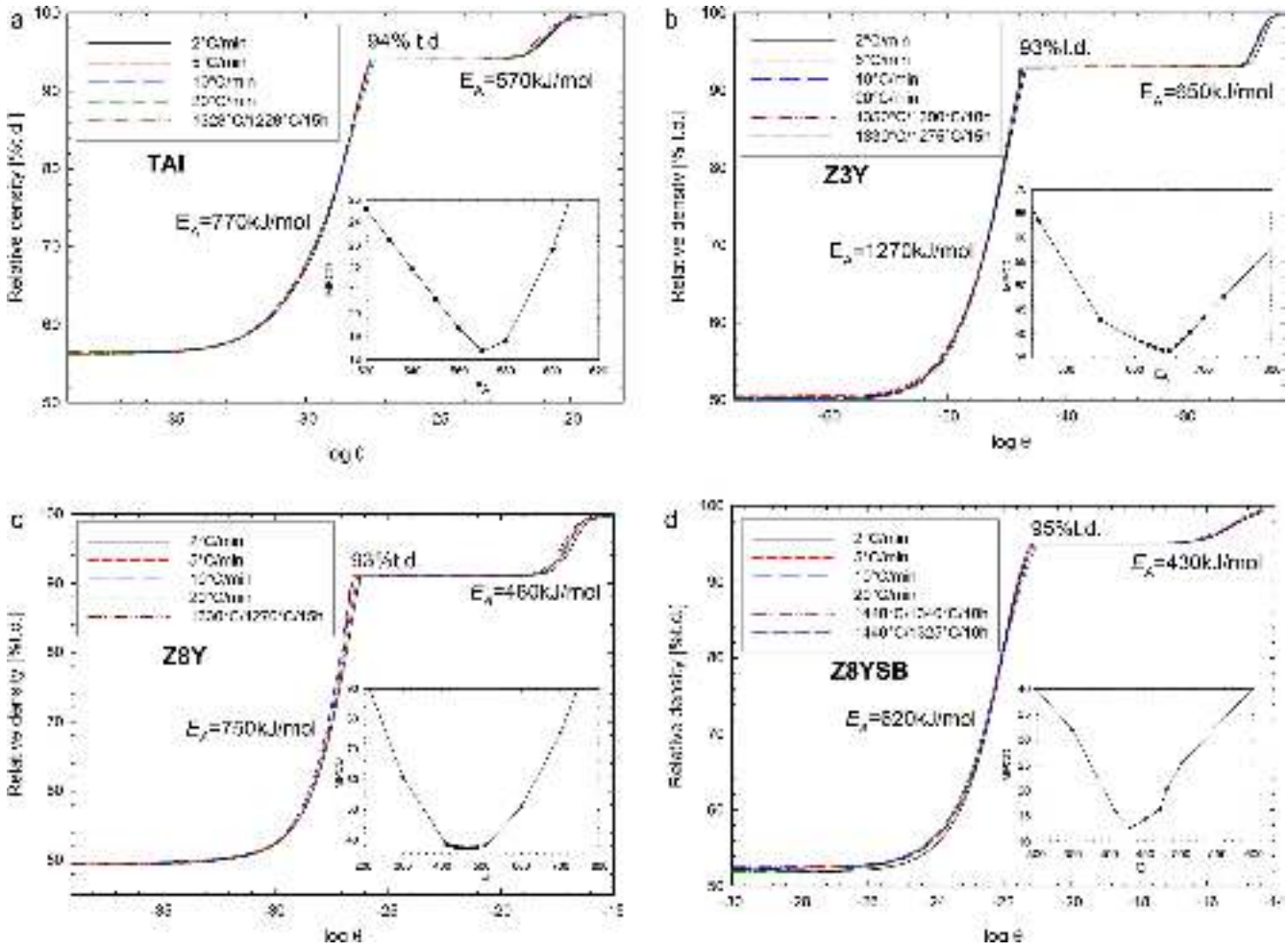

Fig. 4. (a) TS-MSC and MPCD (inset) of TAI calculated from SSS and TSS experiments. (b) TS-MSC and MPCD (inset) of Z3Y calculated from SSS and TSS experiments. (c) TS-MSC and MPCD (inset) of Z8Y calculated from SSS and TSS experiments. (d) TS-MSC and MPCD (inset) of Z8YSB calculated from SSS and TSS experiments.

activation energy of grain growth were measured in the temperature range 1400–1650 °C, while the second step of TSS was performed in this work at temperatures of 1228–1340 °C (see Table 1).

The results of this research can contribute to the better understanding of the processes occurring during Two-Step Sintering. The better description of the sintering with two-stage Master Sintering Curve will also allow the valuable

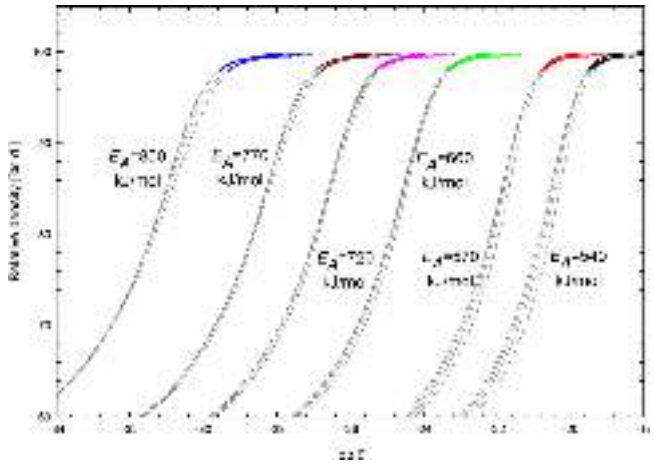

Fig. 5. Small sensitivity of MSC in the final sintering stage on the value of activation energy for SSS heating regimes for TAI.

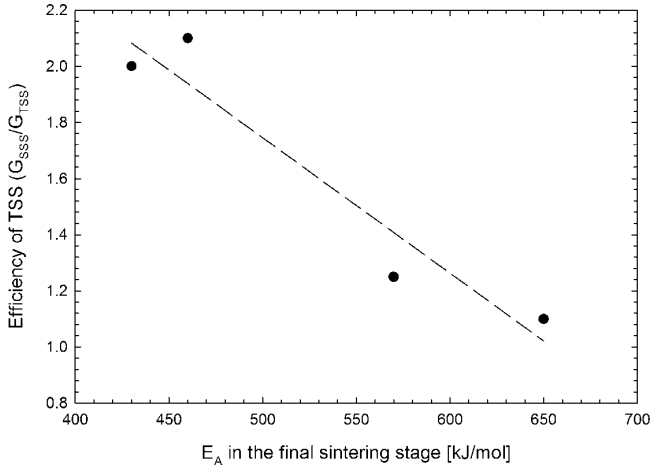

Fig. 6. The dependence of TSS efficiency on sintering activation energy in the final sintering stage.

prediction of Two-Step Sintering. This will be the goal of our next work.

4. Conclusion

The Master Sintering Curve was successfully constructed for t-ZrO_2, c-ZrO_2 as well as for Al_2O_3 sintered by Single Step Sintering. The calculated activation energies were 770 kJ/mol for Al_2O_3, 1270 kJ/mol for t-ZrO_2, 620 kJ/mol and 750 kJ/mol for c-ZrO_2 ceramics. These values were in good agreement with the sintering activation energies calculated from densification rates in the intermediate sintering stage. The application of MSC for samples sintered by Two Step Sintering showed the necessity to split MSC into a low-density part with the same sintering activation energy as was calculated for the SSS experiments, and a high-density part with a lower activation energy. An increase in TSS efficiency with decreasing of sintering activation energy in the final stage of sintering was observed.

Acknowledgement

The authors gratefully acknowledge the funding provided by the European Regional Development Fund through a project CEITEC (CZ.1.05/1.1.00/02.0068) and by the Swedish Research Council through the Grant No. 621-2008-5730.

References

1. Lange FF. Transformation Toughening.3. Experimental-Observations in the ZrO_2–Y_2O_3 System. *J Mater Sci* 1982;**17**:240–6.
2. Park CO, Fergus JW, Miura N, Park J, Choi A. Solid-state electrochemical gas sensors. *Ionics* 2009;**15**:261–84.
3. Maskell WC. Progress in the development of zirconia gas sensors. *Solid State Ionics* 2000;**134**:43–50.
4. Takahashi H, Takeguchi T, Yamamoto N, Ueda W. Ni cermet solid oxide fuel cell anodes prepared from nanoparticle Y(2)O(3)–CeO(2)–ZrO(2) solid solutions. *Solid State Ionics* 2011;**185**:52–7.
5. Cronin JS, Wilson JR, Barnett SA. Impact of pore microstructure evolution on polarization resistance of Ni-Yttria-stabilized zirconia fuel cell anodes. *J Power Sources* 2011;**196**:2640–3.
6. Fitting HJ, Meyza X, Guerret-Piecourt C, Dutriez C, Touzin M, Goeuriot D, et al. Selfconsistent electrical charging in insulators. *J Eur Ceram Soc* 2005;**25**:2799–803.
7. Hannouche D, Zaoui A, Zadegan F, Sedel L, Nizard R. Thirty years of experience with alumina-on-alumina bearings in total hip arthroplasty. *Int Orthop* 2011;**35**:207–13.
8. Krell A, Klimke J, Hutzler T. Transparent compact ceramics: inherent physical issues. *Opt Mater* 2009;**31**:1144–50.
9. Krell A, Blank P. Grain-size dependence of hardness in dense submicrometer alumina. *J Am Ceram Soc* 1995;**78**:1118–20.
10. Krell A, Blank P. The influence of shaping method on the grain size dependence of strength in dense submicrometre alumina. *J Eur Ceram Soc* 1996;**16**:1189–200.
11. Krell A, Klaffke D. Effects of grain size and humidity on fretting wear in fine-grained alumina, Al_2O_3/TiC, and zirconia. *J Am Ceram Soc* 1996;**79**:1139–46.
12. Apetz R, Van Bruggen MPB. Transparent alumina: a light-scattering model. *J Am Ceram Soc* 2003;**86**:480–6.
13. Mayo MJ. Processing of nanocrystalline ceramics from ultrafine particles. *Int Mater Rev* 1996;**41**:85–115.
14. Maca K, Simonikova S. Effect of sintering schedule on grain size of oxide ceramics. *J Mater Sci* 2005;**40**:5581–9.
15. Su HH, Johnson DL. Master sintering curve: a practical approach to sintering. *J Am Ceram Soc* 1996;**79**:3211–7.
16. Hansen JD, Rusin RP, Teng MH, Johnson DL. Combined-stage sintering model. *J Am Ceram Soc* 1992;**75**:1129–35.
17. An KJ, Han MK, Kim HJ. The pressure-assisted master sintering surface of metallic powder mixture. *Mater Trans* 2010;**51**:822–5.
18. Pouchly V, Maca K. Master sintering curve – a practical approach to its construction. *Sci Sinter* 2010;**42**:25–32.
19. Chen IW, Wang XH. Sintering dense nanocrystalline ceramics without final-stage grain growth. *Nature* 2000;**404**:168–71.
20. Galusek D, Ghillanyova K, Sedlacek J, Kozankova J, Sajgalik P. The influence of additives on microstrucutre of sub-micron alumina ceramics prepared by two-stage sintering. *J Eur Ceram Soc* 2012;**32**:1965–70.
21. Bodisova K, Sajgalik P, Galusek D, Svancarek P. Two-stage sintering of alumina with submicrometer grain size. *J Am Ceram Soc* 2007;**90**:330–2.
22. Maca K, Pouchly V, Zalud P. Two-step sintering of oxide ceramics with various crystal structures. *J Eur Ceram Soc* 2010;**30**:583–9.
23. Mazaheri M, Simchi A, Golestani-Fard F. Densification and grain growth of nanocrystalline 3Y-TZP during two-step sintering. *J Eur Ceram Soc* 2008;**28**:2933–9.
24. Mazaheri M, Valefi M, Hesabi ZR, Sadrnezhaad SK. Two-step sintering of nanocrystalline 8Y(2)O(3) stabilized ZrO(2) synthesized by glycine nitrate process. *Ceram Int* 2009;**35**:13–20.
25. Maca K, Pouchly V, Shen ZJ. Two-step sintering and spark plasma sintering of Al_2O_3, ZrO_2 and $SrTiO_3$ ceramics. *Integr Ferroelectr* 2008;**99**:114–24.
26. Bernard-Granger G, Guizard C. Apparent activation energy for the densification of a commercially available granulated zirconia powder. *J Am Ceram Soc* 2007;**90**:1246–50.
27. Song XC, Lu J, Zhang TS, Ma J. Two-stage master sintering curve approach to sintering kinetics of undoped and Al(2)O(3)-doped 8 Mol% yttria-stabilized cubic zirconia. *J Am Ceram Soc* 2011;**94**:1053–9.
28. Shao WQ, Chen SO, Li D, Cao HS, Zhang YC, Zhang SS. Apparent activation energy for densification of alpha-Al(2)O(3) powder at constant heating-rate sintering. *B Mater Sci* 2008;**31**:903–6.
29. Maca K, Pouchly V, Boccaccini AR. Sintering densification curve – a practical approach for its construction from dilatometric shrinkage data. *Sci Sinter* 2008;**40**:117–22.
30. Wang JD, Raj R. Estimate of the activation-energies for boundary diffusion from rate-controlled sintering of pure alumina, and alumina doped with zirconia or titania. *J Am Ceram Soc* 1990;**73**:1172–5.
31. Kanters J, Eisele U, Rodel J. Effect of initial grain size on sintering trajectories. *Acta Mater* 2000;**48**:1239–46.
32. Bernard-Granger G, Addad A, Fantozzi G, Bonnefont G, Guizard C, Vernat D. Spark plasma sintering of a commercially available granulated zirconia powder: comparison with hot-pressing. *Acta Mater* 2010;**58**:3390–9.
33. He ZM, Ma J. Constitutive modeling of alumina sintering: grain-size effect on dominant densification mechanism. *Comp Mater Sci* 2005;**32**:196–202.
34. Shao WQ, Chen SO, Li D, Cao HS, Zhang YC, Zhang SS. Prediction of densification and microstructure evolution for alpha-Al(2)O(3) during pressureless sintering at low heating rates based on the master sintering curve theory. *Sci Sinter* 2008;**40**:251–61.
35. Dahl P, Kaus I, Zhao Z, Johnsson M, Nygren M, Wiik K, et al. Densification and properties of zirconia prepared by three different sintering techniques. *Ceram Int* 2007;**33**:1603–10.
36. Pouchly V, Maca K. Master sintering curves of two different alumina powder compacts. *Proc Appl Ceram* 2009;**3**:177–80.
37. Li D, Chen S, Shao WQ, Ge XH, Zhang YH, Zhang SS. Densification evolution of TiO_2 ceramics during sintering based on the master sintering curve theory. *Mater Lett* 2008;**62**:849–51.
38. Robertson IM, Schaffer GB. Refinement of master densification curves for sintering of titanium. *Metall Mater Trans A* 2010;**41A**:2949–58.
39. Kiani S, Pan J, Yeomans JA. A new scheme of finding the master sintering curve. *J Am Ceram Soc* 2006;**89**:3393–6.
40. Blaine DC, Park SJ, German RM. Linearization of master sintering curve. *J Am Ceram Soc* 2009;**92**:1403–9.
41. Matsui K, Ohmichi N, Ohgai M, Enomoto N, Hojo J. Sintering kinetics at constant rates of heating: effect of Al_2O_3 on the initial sintering stage of fine zirconia powder. *J Am Ceram Soc* 2005;**88**:3346–52.

42. Wang JD, Raj R. Activation-energy for the sintering of 2-phase alumina zirconia ceramics. *J Am Ceram Soc* 1991;**74**:1959–63.
43. Taylor MA, Kilo M, Borchardt G, Weber S, Scherrer H. Zr-96 diffusion in polycrystalline scandia stabilized zirconia. *J Eur Ceram Soc* 2005;**25**:1591–5.
44. Wang CM, Chan HM, Harmer MP. Effect of Nd_2O_3 doping on the densification and abnormal grain growth behavior of high-purity alumina. *J Am Ceram Soc* 2004;**87**:378–83.
45. Voytovych R, Maclaren I, Gulgun MA, Cannon RM, Ruhle M. The effect of yttrium on densification and grain growth in alpha-alumina. *Acta Mater* 2002;**50**:3453–63.
46. Chaim R. Activation energy and grain growth in nanocrystalline Y-TZP ceramics. *Mat Sci Eng A – Struct* 2008;**486**:439–46.
47. Zhao J, Ikuhara Y, Sakuma T. Grain growth of silica-added zirconia annealed in the cubic/tetragonal two-phase region. *J Am Ceram Soc* 1998;**81**: 2087–92.
48. Quach DV, Avila-Paredes H, Kim S, Martin M, Munir ZA. Pressure effects and grain growth kinetics in the consolidation of nanostructured fully stabilized zirconia by pulsed electric current sintering. *Acta Mater* 2010;**58**:5022–30.
49. Sharif AA, Imamura PH, Mitchell TE, Mecartney ML. Control of grain growth using intergranular silicate phases in cubic yttria stabilized zirconia. *Acta Mater* 1998;**46**:3863–72.
50. Koruza J, Malic B, Kosec M. Microstructure evolution during sintering of sodium niobate. *J Am Ceram Soc* 2011;**94**:4174–8.

Vaclav Pouchly is a postdoc in a group of Advanced Ceramic Materials at the Central European Institute of Technology, Brno University of Technology in Czech Republic under his mentor Karel Maca. In 2012 he received his doctoral degree in material sciences at Brno University of Technology in Czech Republic where he also got in 2009 master degree. He published 5 impact papers with 23 citations (*h*-index 3).

Karel Maca is a senior researcher in a group of Advanced Ceramic Materials at the Central European Institute of Technology, Brno University of Technology in Czech Republic. He received his master degree in physics of Solid State at Masaryk University in Czech Republic. In 1997 he received doctoral degree in physical and material engineering at Brno University of Technology in Czech Republic. In 2011 he became a full professor at Brno University of Technology. During the last 10 years he devoted his research namely to study of sintering behaviour and sintering kinetics of ceramic materials. He is author or co-author of 29 publications with 200 citations (*h*-index 10).

Zhijian Shen is a senior researcher and project leader at the Arrhenius Laboratory in Stockholm University in Sweden. He received his undergraduate education in Ceramic Engineering between 1978 and 1982 in Wuhan University of Technology and PhD in Materials Physics and Chemistry from Zhejiang University of China in 1990. He worked as a lecturer in Tongji University and associate professor in Zhejiang University before moving from China to Sweden in 1993. Since then he has worked in the same institute for almost 20 years, during which he has devoted his main research efforts to developing novel processing concepts for synthesizing new inorganic matter and for producing ceramics and ceramic composites with tailored microstructures and integrated properties. He was promoted as docent in 2001 and professor in 2007. He held between 2007 and 2011 a Nobel Biocare Chair of Materials Innovation and worked very closely with the industrial partner Nobel Biocare on developing advanced ceramics for dentistry. He is author or co-author of more than 200 publications with more than 2500 citations (h-index 27) and holds 10 patents.

Available online at www.sciencedirect.com

ScienceDirect

Journal of the European Ceramic Society 34 (2014) 4363–4372

www.elsevier.com/locate/jeurceramsoc

Densification of fine-grained alumina ceramics doped by magnesia, yttria and zirconia evaluated by two different sintering models

Karel Maca [a,*], Václav Pouchlý [a], Katarína Bodišová [b], Peter Švančárek [c], Dušan Galusek [c]

[a] *Brno University of Technology, CEITEC BUT, Brno, Czech Republic*
[b] *Faculty of Food and Chemical Technology, Slovak Technical University, Bratislava, Slovakia*
[c] *Joint Glass Centre of the IIC SAS, TnU AD, and FChFT STU, Trenčín, Slovakia*

Received 25 February 2014; received in revised form 12 June 2014; accepted 25 June 2014
Available online 17 July 2014

Abstract

The influence of various dopants (500 ppm MgO and Y_2O_3; 250 ppm ZrO_2) on sintering of fine-grained alumina ceramics was evaluated by high-temperature dilatometry. The apparent activation energy of sintering was estimated with the help of Master Sintering Curve and a model proposed by Wang and Raj. The densification kinetics was controlled by at least two mechanisms operating at low (higher activation energy) and high (lower activation energy) densities. Good agreement between the activation energies calculated with both models was observed for low as well as for high densities. The lowest value of activation energy exhibited undoped alumina; the addition of MgO resulted in slight increase of the activation energy. Y_2O_3 and ZrO_2 significantly inhibited the densification, which was reflected in the higher sintering activation energies. The low activation energies in the final sintering step indicates the importance of proper choice of sintering temperature, namely in the two-step sintering process.

Keywords: Sintering; Alumina; Activation energy

1. Introduction

Microstructure refinement in advanced ceramic materials is frequently associated with improved mechanical properties, especially hardness,[1] flexural strength[2,3] and wear resistance.[4] Moreover, it often provides additional functionalities, such as transparency in the visible wavelength range, as was also documented for polycrystalline alumina with submicron grain size.[5,6] A range of densification techniques including pressure assisted processes such as hot pressing,[7] hot isostatic pressing,[8] spark plasma sintering[9–11] or pressure-less techniques such as microwave assisted sintering[12] and two-step sintering (TSS)[13–15] were therefore applied with the aim to prepare fully dense polycrystalline alumina, and at the same time to suppress or completely eliminate grain growth in the final stage of sintering. Among them, the two-step sintering[16] is of particular interest due to its simplicity and the possibility of achieving complete densification at relatively low temperatures without application of pressure; its capacity has been demonstrated for a range of various systems.[17–23] Only few works dealing with the two-step sintering of alumina report on some refinement of microstructure in comparison to conventionally sintered reference materials.[14,24]

The addition of various metal oxides at ppm level, which are known to alter the behaviour of alumina during its solid state sintering, represents another opportunity for microstructure refinement. The effect is often associated with the change in the activation energy of both the grain boundary diffusion and the grain boundary motion, and hence also densification and grain growth. The effect of yttria, zirconia, and magnesia on microstructure refinement during the two-step sintering[25] and spark plasma sintering followed by hot isostatic pressing

* Corresponding author. Tel.: +420 54114 3344.
E-mail addresses: maca@fme.vutbr.cz, karel.maca@ceitec.vutbr.cz (K. Maca).

http://dx.doi.org/10.1016/j.jeurceramsoc.2014.06.030
0955-2219/

of doped polycrystalline alumina with submicron grains[26] was demonstrated.

In conventional sintering, MgO is considered to be the most frequently used and most efficient grain growth suppressor. The effect of magnesia is often attributed to solute drag (or pinning) mechanisms; it is proposed that MgO reduces the grain boundary mobility as a solute in the corundum crystal or segregated preferentially in the grain boundaries.[27] On the other hand, Jo et al.[28] attribute the effect of magnesia to change in the interface structure of alumina grains. Atomically smooth faces of alumina crystals became rough when heated in MgO-containing atmosphere. Then grain growth is not controlled by interface reaction but by diffusion, and the number of grains that can grow increases to such an extent that they impinge on each other. The roughening of atomically smooth surfaces also explains the enhanced densification rate. Diffusion in a system with disordered grain boundaries is expected to be easier, with corresponding increase in surface and grain boundary diffusion rates.[28]

Another group of dopants is represented by other metal oxides such as yttria and zirconia. Both these dopants have limited solubility in alumina and therefore they segregate at grain boundaries. This can significantly hinder diffusion and therefore also densification and grain growth.

Since various dopants influence the sintering behaviour in a different way, some quantification of their influence on sintering kinetics is desirable. One of the promising and practical approaches describing sintering behaviour during the whole sintering process is the Master Sintering Curve (MSC). The MSC was derived by Su and Johnson.[29] Into the sintering model by Hansen et al.[30] they introduced two assumptions: (1) the microstructure evolution (grain size and shape) is function only of density and not on thermal history and (2) the sintering is controlled by only one dominating diffusion mechanism. After a few rearrangements and mathematical operations they obtained Eq. (1):

$$\frac{k}{\gamma\Omega\delta D_0}\int_{\rho_0}^{\rho}\frac{(G(\rho))^n}{3\rho\Gamma(\rho)}d\rho = \int_0^t \frac{1}{T}\exp\left(-\frac{E_A}{RT}\right)dt, \quad (1)$$

where k is the Boltzmann constant, γ is the surface energy, Ω is the atomic volume, δ is the grain boundary thickness, D_0 is the diffusion constant, ρ is the density of the sample, G is the mean grain size, the value of parameter n is 3 (for volume diffusion) or 4 (for grain boundary diffusion), Γ represents the scaling parameter that relates various geometric features as the driving force for sintering and the mean diffusion distance to the grain size, t is the time, T is the absolute temperature, E_A is the activation energy of sintering process and R is the gas constant. MSC is a function of density plotted vs. the logarithm of the right side of the Eq. (1) (usually denoted as Θ). In practice, the MSC is empirically derived from the data obtained from dilatometry measurements at different heating rates (and/or various sintering temperatures) by fitting all data with different E_A values, until they converge onto a single (master) curve.

Till now, the MSC has been constructed for many materials mainly including ceramic oxides (Al_2O_3,[29,31] ZrO_2,[31,32] TiO_2,[33] and $BaTiO_3$[34]), and metals (stainless steel, molybdenum, and tungsten[35]). Many attempts have been made to refine the basic MSC model in order to suit some particular requirements. An and Han[36] extended the MSC model to pressure-assisted sintering. Enneti et al. extended the applicability of the MSC to field-assisted sintering.[37,38] An et al.[39] constructed sintering diagrams from MSC for easy prediction of sintering behaviour at certain temperatures, Raether and Horn[40] compared the MSC and kinetics diagrams. Kiani et al.[41] and Blaine et al.[35] simplified the MSC model by describing it by the finite elements method and by linearization, respectively. Robertson and Schaffer[42] extended the basic MSC model by introducing grain growth during sintering. Diantonio et al.[43] applied the MSC for decomposition of organics and Wang and Teng[44] scaled up their work by formulating the MSC theory for all processes described by Arrhenius type equations. Song et al.[45] and Pouchly et al.[46] assumed that the diffusion mechanism during sintering could change, which resulted in a two-stage MSC.

The change in the activation energy during the sintering process was also observed if a different model by Wang and Raj was used.[47] This model combines two different equations describing the shrinkage during sintering. After rearrangements, Eq. (2) was obtained:

$$\ln\left(T\frac{d\rho}{dT}\frac{dT}{dt}\right) = -\frac{E_A}{RT} + \ln(f(\rho)) + \ln A - n\ln G, \quad (2)$$

where A is a constant defined elsewhere,[47] and G is the grain size. At different heating rates dT/dt and at a constant value of ρ the plot of the left side of Eq. (2) against the reciprocal temperature $1/T$ would be a straight line with the slope which gives the value of E_A. It should be noted that this is valid only if the grain size remains constant during sintering or, at least if the grain size is only a function of density (i.e. independent of heating schedule).[48]

The goal of this work is to describe the sintering behaviour of both doped and undoped aluminas by dilatometry. Two different models (Wang and Raj model and MSC) were used to describe sintering kinetics. The first is used to reveal possible changes of densification mechanisms associated with change of activation energy during densification and the second one to verify the obtained values.

2. Experimental

2.1. Materials

High purity commercial submicron alumina powder Taimicron TM-DAR (Taimei Chemicals Co., Ltd., Tokyo, Japan) was used in all experiments. The characteristics of the powder, as given by the producer, are as follows: purity 99.99%, the mean particle size 150 nm. The dopants (500 ppm (mole) of Mg, Y or 250 ppm of Zr with respect to Al_2O_3) were added by mixing 100 g of the alumina powder with calculated amounts of suitable precursors $Mg(NO_3)_2{\cdot}6H_2O$ (p.a., Lachema Brno,

Czech Republic), zirconium acetate (p.a., Lachema Brno, Czech Republic), and $Y(NO_3)_3 \cdot 6H_2O$ (99.8% purity, Sigma–Aldrich), dissolved in isopropanol. Zirconia was added in lower amount than the other two dopants because zirconia secondary phase in the form of discrete particles was already observed at 500 ppm addition.[25,49] The presence of second phase is undesirable in term of prospective application for preparation of fine-grained transparent alumina, and introduces another parameter influencing densification kinetics, i.e. grain boundary pinning. The mixture was homogenized by ball milling with high purity alumina milling balls for 20 h in a polyethylene jar. Ammonia solution was added to precipitate the respective hydroxides, the mixtures were further homogenized for 4 h to complete the hydrolysis, and the solvent was removed in a vacuum evaporator. The powders were crushed with pestle in agate mortar, sieved through a 100 μm polyethylene sieve, calcined for 1 h at 800 °C in air to convert hydroxides to the respective oxides, and sieved again to obtain a reasonably free flowing powder. The specimens containing MgO, Y_2O_3 and ZrO_2 are denoted AM, AY, and AZ, respectively. The reference alumina powder (denoted as A) was treated in the same way (including milling in isopropanol, calcination, and sieving) to ensure similarity with the doped powders.

In order to avoid calcination, which was found to impair densification,[50] the MgO-doped sample denoted as AMS was prepared also by mixing the alumina powder with $MgAl_2O_4$ spinel (Baikalox S30CR, Baikowski, France). The specific surface area of the spinel powder, as provided by the producer, was 30 $m^2\,g^{-1}$ (BET), which corresponds to the mean particle size of ca 60 nm.[51] The solvent was removed in the vacuum evaporator and dried powder was sieved through 100 and 40 μm polyethylene sieves.

Untreated alumina powder (denoted as AA) was used as the reference.

2.2. Methods

Green pellets with a diameter of 25 and 5 mm thick were prepared by uniaxial pressing at 100 MPa in a steel die, followed by cold isostatic pressing at 250 MPa.

The pellets were cut and ground to the shape of prisms of ca. 4 mm × 4 mm × 15 mm for dilatometry experiments (L70/1700, Linseis, Germany), or ca. 8 mm × 10 mm × 10 mm for sintering in a superkanthal resistance furnace (K1700/1, Heraeus, Germany). The sintering in the dilatometer was carried out at four different heating rates 2, 5, 10 and 20 °C/min up to the maximum temperature of sintering. The recorded temperature–shrinkage curves were converted to densification curves by a procedure described elsewhere.[52] The used heating schedules are summarized in Table 1.

The final relative densities of samples were determined on the basis of Archimedes' principle (EN 623-2) taking 3.99 g cm^{-3} as the theoretical density (t.d.) of all samples and with distilled water as the liquid medium. The microstructure of sintered specimens after all experiments was examined by scanning electron microscopy (JEOL JSM-7600F, Japan). The mean grain size was determined both from polished and thermally etched cross sections as well as from fracture surfaces. The temperature of thermal etching was adjusted in order to ensure delineation of grain boundaries without grain growth, but at the same time to take into account the influence of dopants which, especially in the case of ZrO_2 and Y_2O_3, significantly impaired both densification and grain growth.[25,26] The mean size of alumina matrix grains was determined by the linear intercept method according to the ASTM STP 839 standard, using a correction factor of 1.56.[53] As prescribed by the standard, a minimum of 200 grains were measured for each material, in order to obtain a statistically robust set of data.[54]

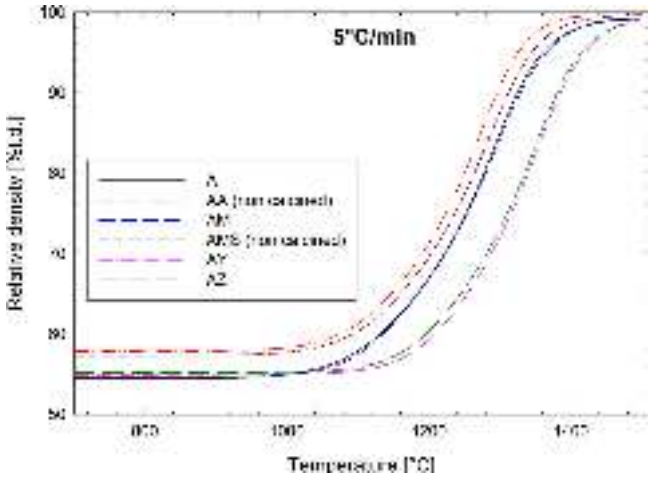

Fig. 1. Densification curves of all doped and undoped alumina.

2.3. Evaluation of the activation energies of sintering

For the construction of MSC, the dilatometric curves recorded at four heating rates 2, 5, 10 and 20 °C/min were used. The values of activation energy of sintering were found by minimizing the mean perpendicular curve distance criterion, which is described elsewhere.[31] Identical heating rates were also used for the determination of the activation energy of sintering with the use of the model by Wang and Raj.

3. Results

3.1. Densification curves

The conditions of the dilatometry experiments green and final relative densities of sintered materials are summarized in Table 1. The green densities of all samples prepared from calcined powders were lower (54.3–55.1%t.d.) than the green densities of all samples prepared from uncalcined powders (57.0–57.7%t.d.), in both cases irrespective of the dopant type. The densification curves recorded at a heating rate of 5 °C/min are shown in Fig. 1. The samples prepared from as-received powders AA and AMS (i.e. those prepared without calcination required to convert hydroxides to respective oxides) reached the highest green and final densities. They also sintered at lower temperatures than their calcined counterparts. Other four powders were calcined at the temperature of 800 °C for 1 h. The

Table 1
The summary of heating schedules and obtained final densities and grain sizes.

Material	Heating rate (°C/min)	Heating schedule (°C/min)	ρ_{green} (%t.d.)	ρ (%t.d.)	*s/n*	G_p (μm)	*s/n*	G_f (μm)	*s/n*
A	2	1500/0	54.7	99.39	0.09/9	3.30	0.70/210	2.14	0.17/200
	5	1500/0	54.4	99.21	0.15/9	2.60	0.50/250	2.06	0.24/210
	10	1500/0	54.7	99.12	0.07/12	1.80	0.40/200	1.77	0.18/220
	20	1500/30	54.3	99.32	0.12/9	3.30	0.80/230	2.16	0.22/260
AA	2	1500/0	57.5	99.40	0.21/9	3.80	0.50/200	3.60	0.82/230
	5	1500/0	57.7	99.60	0.10/12	3.30	0.50/220	2.60	0.63/210
	10	1500/0	57.5	99.40	0.15/9	3.00	0.60/210	2.37	0.39/210
	20	1500/30	57.6	99.46	0.17/12	3.50	0.80/240	2.54	0.53/210
AM	2	1500/0	54.7	99.42	0.24/12	1.30	0.20/230	0.89	0.21/240
	5	1500/0	54.6	99.24	0.21/9	1.10	0.20/200	0.85	0.19/230
	10	1500/0	54.7	99.36	0.10/12	0.95	0.21/210	0.81	0.09/220
	20	1500/0	54.8	99.24	0.27/12	0.76	0.20/210	0.78	0.16/220
AMS	2	1500/0	57.0	99.84	0.11/9	1.30	0.40/260	1.10	0.24/200
	5	1500/0	57.1	99.70	0.10/12	0.95	0.18/200	0.84	0.11/200
	10	1500/0	57.3	99.60	0.04/9	0.91	0.16/210	0.83	0.16/210
	20	1500/30	57.3	99.73	0.16/12	1.40	0.30/250	0.88	0.16/200
AY	2	1500/0	54.8	99.39	0.10/9	1.50	0.40/200	0.94	0.18/230
	5	1500/0	54.7	99.20	0.09/9	1.15	0.18/210	0.77	0.10/230
	10	1500/0	55.1	98.97	0.07/9	1.00	0.20/210	0.80	0.18/200
	20	1500/0	54.7	99.53	0.10/9	2.30	0.60/200	1.80	0.30/210
AZ	2	1500/0	55.1	99.45	0.18/9	1.50	0.40/240	1.48	0.31/250
	5	1500/0	55.1	98.94	0.14/12	1.30	0.30/220	0.97	0.22/200
	10	1500/0	55.0	98.63	0.17/9	0.99	0.19/200	0.87	0.23/210
	20	1500/30	54.0	99.29	0.14/12	1.90	0.40/210	1.69	0.25/200

Note: s is standard deviation, *n* is number of measurements, G_p is mean grain size evaluated from polished surface and G_f is mean grain size evaluated from fracture surface.

calcination influenced both the green densities and the sintering characteristics negatively. The calcination led to formation of aggregates, which impaired densification, as observed in our previous work on sintering of undoped alumina prepared by uniaxial pressing from calcined alumina powders.[50] Application of cold isostatic pressing at markedly higher pressure destroyed the aggregates to a certain extent. However, slower densification of calcined samples reported in this work indicated that aggregates could not be fully eliminated even by isostatic pressing at 250 MPa. Additions of yttria and zirconia had no observable influence on green density, but their densification retarding action was obvious and comparable, despite of different amounts of individual dopants added. This was explained by segregation of the yttrium and zirconium ions into grain boundaries, with resulting inhibition of grain boundary mobility,[25,26] and expected increase of the activation energy of grain boundary diffusion.

3.2. Microstructure evolution

The results of evaluation of the grain size of sintered materials and the sintering trajectories of all studied materials are shown in Fig. 2. The mean grain sizes evaluated from fracture surfaces are in good agreement to those determined by the linear intercept method on polished and thermally etched cross sections. Any differences were well within the range of the statistical deviation of the grain size evaluation. Although this deviation increased with the increasing grain size, we did not observe abnormal grain growth. It should be also noted that significant grain growth occurs at relative densities higher than 98%t.d. for all materials under investigation. The sintering trajectory was fitted according to German model[55] by linearly increasing function up to the relative density of 97–98%, and then by inverse square-root function of the residual porosity. The results show that the model agrees well with the experimental data (Fig. 2).

3.3. Model by Wang and Raj

As mentioned above, virtually no grain growth was observed at relative densities lower than 98%t.d. (see Fig. 2). This facilitated the application of the model by Wang and Raj almost for the whole sintering process. The values of apparent activation energies calculated according to this model for the relative densities ranging from 60 to 95%t.d. are shown in Table 2 and Fig. 3. The values of apparent sintering activation energies changed in the course of sintering, being higher at low densities and lower at high densities. The decrease was observed for all tested compositions. For the A, AA, AM and AMS materials the apparent activation energies of sintering ranged from 720 to 770 kJ/mol at relative densities lower than 75%t.d. For relative densities higher than 85%t.d. the activation energy ranged from 620 to 670 kJ/mol. For the AY and AZ materials the activation energies were higher, ranging from 860 to 890 kJ/mol at the relative densities lower than 75% t.d., and 740–750 kJ/mol for the densities higher than 85%t.d. The higher activation energy of sintering of the materials AY

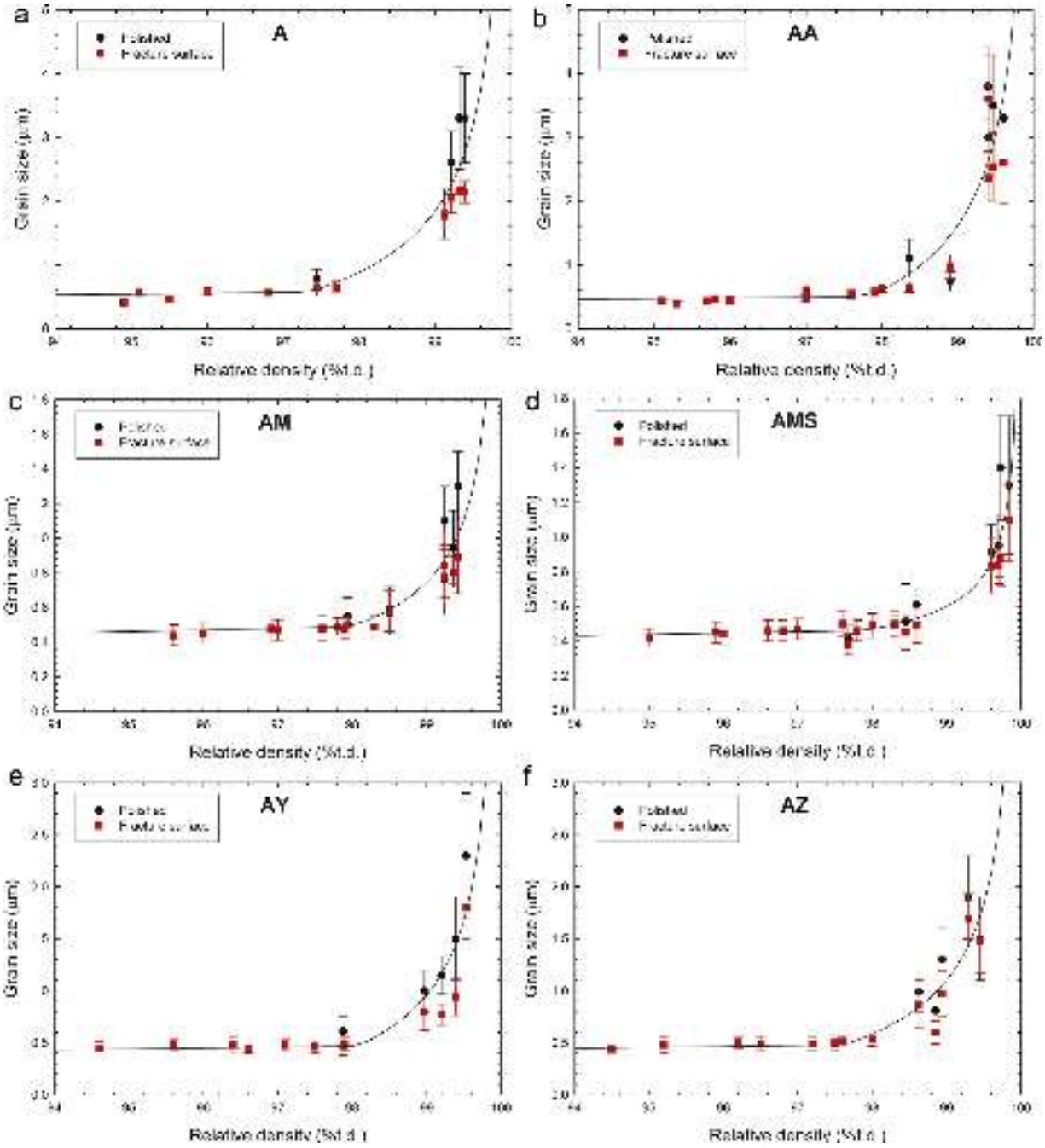

Fig. 2. Sintering trajectories of all doped and undoped aluminas sintered at four different heating rates: (a) calcined alumina (A), (b) non-calcined alumina (AA), (c) calcined alumina doped by 500 ppm MgO (AM), (d) non-calcined alumina doped by 500 ppm $MgAl_2O_4$ (AMS), (e) calcined alumina doped by 500 ppm Y_2O_3 (AY) and (f) calcined alumina doped by 250 ppm ZrO_2 (AZ).

Table 2
Activation energies of all studied materials evaluated by two different methods.

Material	Q_{Wang} $\rho = 60$–75%t.d. (kJ/mol)	Q_{MSC} $\rho < 75\%$t.d. (kJ/mol)	Q_{Wang} $\rho = 85$–95%t.d. (kJ/mol)	Q_{MSC} $\rho > 85\%$t.d. (kJ/mol)
A	760	770	640	630
AA	730	730	620	610
AM	750	760	670	670
AMS	750	760	640	630
AY	890	890	750	760
AZ	860	830	740	750

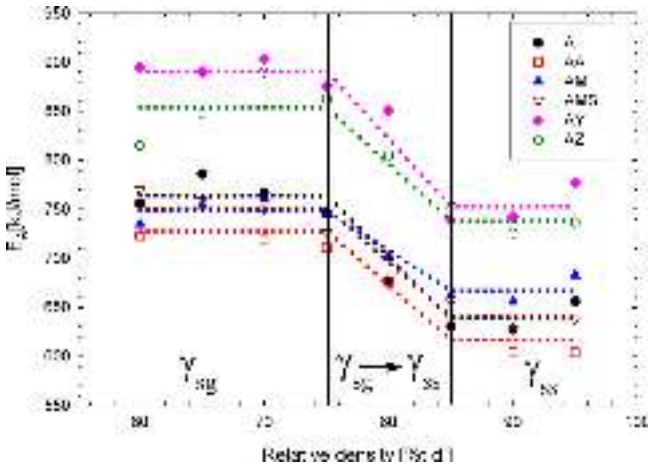

Fig. 3. The activation energy of sintering as a function of relative density determined from the model of Wang and Raj (where: γ_{sg} is the solid–gas surface energy, γ_{ss} is the solid–solid interface energy).

and AZ corresponds to the higher temperatures required for sintering and densifications of these materials (Fig. 1).

3.4. Model of master sintering curve

Based on the results obtained using the model by Wang and Raj, the MSC was also divided into two stages. The separation of MSC into low and high density stages was described by the two-stage MSC model, as already proposed e.g. by Song et al.[45] and Pouchly et al.[46] The results of such separation are shown in Fig. 4. The Mean Perpendicular Curves Distance as a function of activation energy (insets of Fig. 4) contained in all cases a single minimum, thus the activation energy of sintering can be clearly identified for all materials and sintering stages. In excellent agreement with the model by Wang and Raj, the MSC model yielded higher activation energies in the low-density region, with a marked decrease of the activation energies of sintering at the high-density stage. Moreover, the activation energies of sintering determined by the two methods were similar for all the studied materials, and both in low and high density regions (Table 2).

4. Discussion

The MSC model is based on the assumption that microstructure evolution (i.e. grain size and shape) depends only on density and not on thermal history. Fig. 2 shows the sintering trajectories (the grain size dependence on density) for all used heating regimes. It can be seen that all points fall into a single line, documenting that the assumption for construction of the MSC mentioned above is fulfilled for all studied materials in the whole range of relative densities.

Another assumption required for construction of the MSC is that there exists a single diffusion mechanism dominating the whole process of sintering. As can be seen from the analysis based on the Wang and Raj model, this assumption is not valid in this case (Fig. 3).

In this work, the Wang and Raj model was used for the first time up to high densities (95%t.d.). The application of this model also in the final stage of sintering can be justified as follows:

- no relevant grain growth was observed up to 98%t.d. (Fig. 2),
- for all the heating regimes used, there exists a single sintering trajectory for each material, i.e. for the given relative density the grain size is constant irrespective of the heating rate.[56]

Due to the broad interval where the activation energies of sintering were evaluated, three different regions could be distinguished:

- 60–75%t.d.: constant value of the apparent activation energy of sintering (730–890 kJ/mol depending on the doping),
- 75–85%t.d.: transition region with decreasing activation energy of sintering,
- 85–95%t.d.: constant value of the apparent activation energy (620–750 kJ/mol depending on the doping), i.e. lower than the activation energy in the low density region 60–75%t.d.

The results revealed that the MSC should be divided into two regions and the so called two-stage MSC should be constructed. This attitude was already utilized by Song et al. for c-ZrO_2,[45] and by Pouchly et al. for Al_2O_3, t-ZrO_2 and c-ZrO_2.[46] The question naturally arises where to split the MSC. Whereas Song et al. divided their MSC more or less arbitrarily at 60%t.d. (to separate the early and the second stage of sintering),[45] Pouchly et al.[46] used the two-stage MSC model to interpret the results of two-step sintering, and divided the process at the start of the final sintering step.

The results obtained in this work with the use of the model by Wang and Raj show that the transition region, where the activation energies change, lies in the range between 75 and 85%t.d. (Fig. 3). A noticeable decrease in activation energies (calculated from the Wang and Raj model) was also observed by Bernard-Granger and Guizard[56] in the case of t-ZrO_2 in the relative density region between 73 and 91%t.d. According to our results we applied the two-stage MSC in two distinct regions – below 75%t.d. and above 85%t.d. The values of apparent activation energies calculated by the MSC are in excellent agreement with the values acquired by the Wang and Raj model for all studied materials and in both relative density regions (i.e. <75 and >85%t.d.).

The gradual decrease of the apparent activation energy during densification indicates the change in controlling mechanism of densification. In the sintering of alumina, two basic densification mechanisms providing transport of material from the grain boundaries to the necks come into consideration: grain boundary and lattice diffusion. The first one acts along the grain boundaries, the second one through the lattice. According to the published sintering diagrams of alumina,[57,58] it can be expected, considering the grain size and the applied temperatures of sintering, that the grain boundary diffusion dominates almost whole densification process. The lattice diffusion becomes active at very high temperatures especially for fine grained alumina (~2000 °C).[57,58] Therefore some published

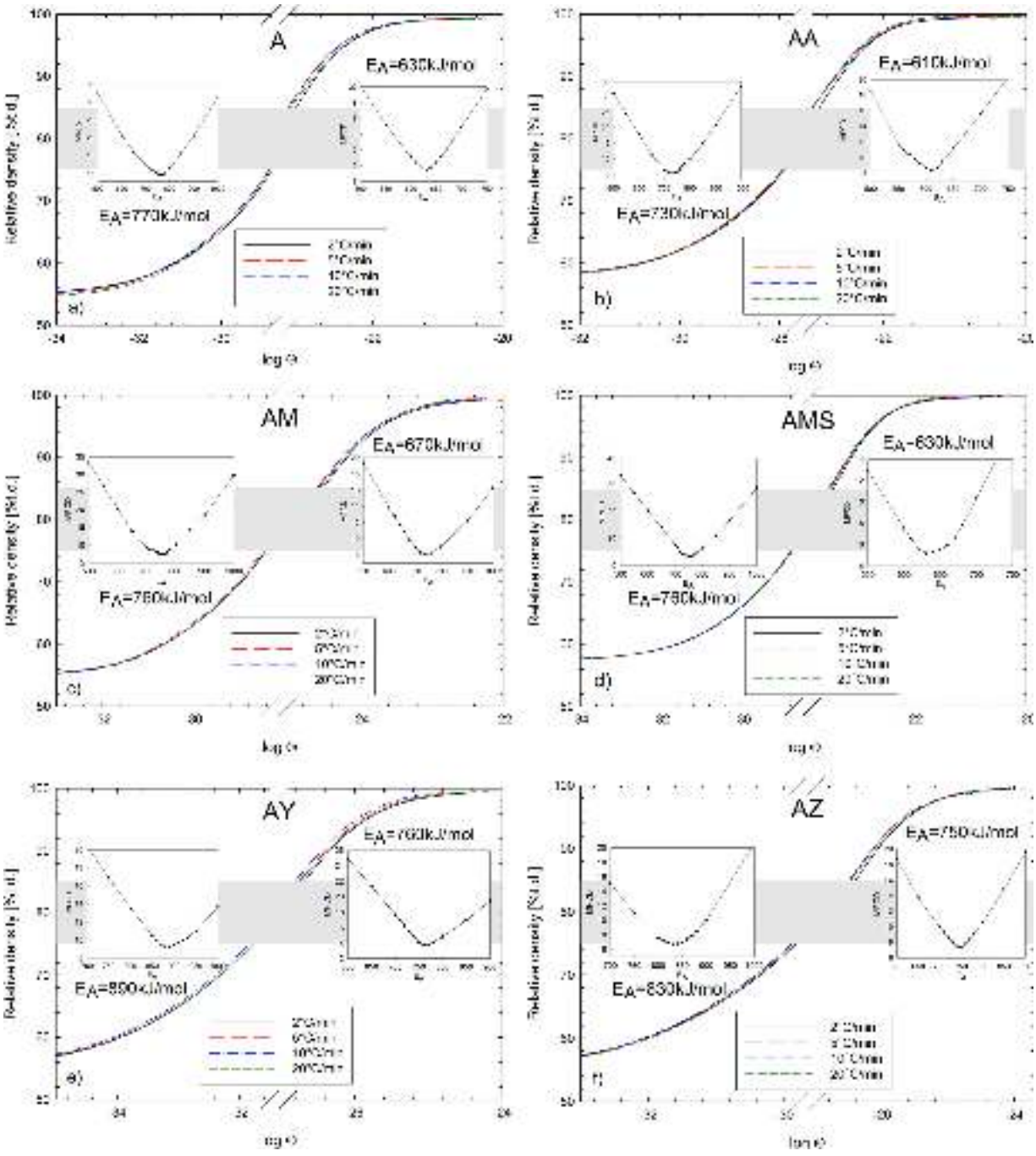

Fig. 4. The two-stage master sintering curves and MPCD (insets) of all used materials (a) calcined alumina (A), (b) non-calcined alumina (AA), (c) calcined alumina doped by 500 ppm MgO (AM), (d) non-calcined alumina doped by 500 ppm $MgAl_2O_4$ (AMS), (e) calcined alumina doped by 500 ppm Y_2O_3 (AY) and (f) calcined alumina doped by 250 ppm ZrO_2 (AZ).

explanations of sintering activation energy decrease due to the mechanism change from grain boundary to lattice diffusion seem to be controversial.[59,60] More probable explanation for enhanced apparent activation energy at the beginning of densification is surface diffusion, which is known to decrease the driving force of densification and therefore to increase the apparent activation energy, yet does not facilitate densification.[45,61] This assumption could be supported also by fact, that apparent activation energy calculated from constant heating rate dilatometric dependences was reported to be increased when lower heating rates were used for calculation.[59] The reason for the observed change of the activation energy is not clear at present: additional experiments have to be carried out to clarify the situation.

However, if we discuss diffusion processes, differences in the effective area, which serves as the source of ions/point defects, as well as the length of diffusion path for mass transport, should be also taken into account. Further possible explanation for the observed gradual decrease in activation energy of sintering at high densities is the change of grains and pores geometry during sintering.[62] In the low-density region, the solid–gas interfaces

contribute significantly to the free energy of the system, and the surface energy γ_{sg} plays an important role.[57] At this stage, grain boundaries represent relatively low fraction of the total surface area of the grains. The grain boundaries are composed of mismatched crystallographic planes of adjoining grains, containing numerous dislocation and point defects. It is well known, that the presence of the defects allows diffusional mass transport to take place; the defects control the rate at which matter is transported and also the rate of densification.[63] Lower specific grain boundary area in the low density region (intermediate stage of sintering) makes the material transport more difficult with correspondingly higher apparent activation energy. In the final sintering stage the total area of grain boundaries increases significantly. The grain boundary diffusion therefore proceeds much easier, which can also contribute to lowering of the apparent activation energies values.

Concerning the influence of dopants, the densification was markedly inhibited especially by the addition of 500 ppm of Y_2O_3 or 250 ppm ZrO_2, which was also reflected in the higher values of the activation energies of sintering, both in low and high density regions (Table 2). Both dopants strongly segregate at alumina-alumina interfaces. Due to its limited solubility in the alumina crystal lattice (~10 atomic ppm) yttria segregates to alumina/alumina interfaces.[64,65] Large yttrium cations segregated at the interfaces block the motion of Al^{3+} and O^{2-} ions along the grain boundaries, which results in reduced grain-boundary diffusivity and decreased densification rate.

On the other hand, the doping by MgO had only minor influence on densification (Fig. 1). The MgO-doped materials were prepared using two different routes. The first one used $Mg(NO_3)_2{\cdot}6H_2O$ as the source of MgO. The procedure included conversion of the nitrate to hydroxide through hydrolysis reaction with ammonia, with final 1 h calcination at 800 °C resulting in decomposition of the hydroxide and formation of MgO (powder AM). The second procedure included simple wet mixing of alumina and $MgAl_2O_4$ spinel powders therefore no calcination was needed (powder AMS). The material AM prepared from the calcined powder had lower green and final density, probably due to the presence of agglomerates.[50] Such materials can contain, after shaping, two different populations of pores – smaller intraagglomerate pores and larger interagglomerate ones.[66] The interagglomerate pores often form the so-called supercritical pores, which can be removed from the body in the final sintering stage only by the growth of surrounding grains. As shown in Table 2, the samples AM and AMS had identical activation energies of sintering in the low-density region. However, in the final stage of sintering the activation energy of the sample AMS prepared without calcination was lower. Higher activation energy determined for the samples prepared from calcined powder could be explained by higher amount of supercritical pores. Moreover, the suppression of grain growth due to magnesia doping (Fig. 2) makes elimination of the supercritical pores even more difficult. This problem was overcome by the alternative way of MgO doping without calcination. Therefore, the focus of our next experimental work will be on finding an alternative way of doping without calcination also for yttria- and zirconia-doped alumina.

5. Conclusions

In order to optimize the effect of various dopants on the microstructure evolution of fine grained alumina ceramics, the densification of pure and MgO, ZrO_2 and Y_2O_3 doped alumina was evaluated by two theoretical models, namely the two-stage Master Sintering Curve and the model by Wang and Raj. The grain growth of both the doped and undoped alumina ceramics was found to be negligible up to relative densities of 98%t.d., which justifies the applicability of the model by Wang and Raj up to the final stage of sintering. As both applied models exhibit similar activation energies, being higher in low-density region (<75%t.d.) and lower in high-density region (>85%t.d.), we can assume that the sintering activation energies established by these approaches are correct.

In all studied cases, the apparent activation energy determined in the low density region was approximately 100 kJ/mol higher than that in the high density stage. The absolute values were influenced by the presence of dopants. Whereas MgO addition affects the densification of alumina only slightly, with a minimal change in the activation energy, marked retarding action of ZrO_2 and Y_2O_3 addition was observed manifesting itself in noticeably higher values of activation energy of sintering. The results of present work are prerequisite for further study dealing with suppression, or complete elimination of grain growth in fine grade aluminas. The very important outcome of our theoretical conclusions is that the low sintering activation energy in the final sintering stage indicates high sensitivity of densification on sintering temperature. Therefore sintering conditions in the final sintering step has to be precisely adjusted in order to ensure complete densification without the grain growth especially in the case of two-step sintering.

Acknowledgements

The authors gratefully acknowledge the funding provided by the European Regional Development Fund through the projects CEITEC (CZ.1.05/1.1.00/02.0068) and "Centre of excellence for ceramics, glass and silicate materials" (ITMS 26220120056) and also by projects EXCELLENT TEAMS (CZ.1.07/2.3.00/30.0005) and CEPLANT (ITMS 22410320043).

References

1. Krell A, Blank P. Grain-size dependence of hardness in dense submicrometer alumina. *J Am Ceram Soc* 1995;**78**:1118–20.
2. Krell A, Blank P. The influence of shaping method on the grain size dependence of strength in dense submicrometre alumina. *J Eur Ceram Soc* 1996;**16**:1189–200.
3. O YT, Koo JB, Hong KJ, Park JS, Shin DC. Effect of grain size on transmittance and mechanical strength of sintered alumina. *Mater Sci Eng A: Struct* 2004;**374**:191–5.
4. Krell A, Klaffke D. Effects of grain size and humidity on fretting wear in fine-grained alumina, Al_2O_3/TiC, and zirconia. *J Am Ceram Soc* 1996;**79**:1139–46.
5. Krell A, Blank P, Ma HW, Hutzler T, Van Bruggen MPB, Apetz R. Transparent sintered corundum with high hardness and strength. *J Am Ceram Soc* 2003;**86**:12–8.

6. Apetz R, Van Bruggen MPB. Transparent alumina: a light-scattering model. *J Am Ceram Soc* 2003;**86**:480–6.
7. Chang S, Doremus RH, Schadler LS, Siegel RW. Hot-pressing of nano-size alumina powder and the resulting mechanical properties. *Int J Appl Ceram Technol* 2004;**1**:172–9.
8. Echeberria J, Tarazona J, He JY, Butler T, Castro F. Sinter-HIP of alpha-alumina powders with sub-micron grain sizes. *J Eur Ceram Soc* 2002;**22**:1801–9.
9. Risbud SH, Shan CH, Mukherjee AK, Kim MJ, Bow JS, Holl RA. Retention of nanostructure in aluminum-oxide by very rapid sintering at 1150-degrees-C. *J Mater Res* 1995;**10**:237–9.
10. Stanciu LA, Kodash VY, Groza JR. Effects of heating rate on densification and grain growth during field-assisted sintering of alpha-Al_2O_3 and $MoSi_2$ powders. *Met Mater Trans A* 2001;**32**:2633–8.
11. Zhou Y, Hirao K, Yamauchi Y, Kanzaki S. Densification and grain growth in pulse electric current sintering of alumina. *J Eur Ceram Soc* 2004;**24**:3465–70.
12. Cheng JP, Agrawal D, Zhang YJ, Roy R. Microwave sintering of transparent alumina. *Mater Lett* 2002;**56**:587–92.
13. Bodisova K, Sajgalik P, Galusek D, Svancarek P. Two-stage sintering of alumina with submicrometer grain size. *J Am Ceram Soc* 2007;**90**: 330–2.
14. Hesabi ZR, Haghighatzadeh A, Mazaheri M, Galusek D, Sadrnezhaad SK. Suppression of grain growth in sub-micrometer alumina via two-step sintering method. *J Eur Ceram Soc* 2009;**29**:1371–7.
15. Maca K, Pouchly V, Zalud P. Two-step sintering of oxide ceramics with various crystal structures. *J Eur Ceram Soc* 2010;**30**:583–9.
16. Chen IW, Wang XH. Sintering dense nanocrystalline ceramics without final-stage grain growth. *Nature* 2000;**404**:168–71.
17. Wang XH, Deng XY, Bai HL, Zhou H, Qu WG, Li LT, et al. Two-step sintering of ceramics with constant grain-size, II: $BaTiO_3$ and Ni–Cu–Zn ferrite. *J Am Ceram Soc* 2006;**89**:438–43.
18. Polotai A, Breece K, Dickey E, Randall C, Ragulya A. A novel approach to sintering nanocrystalline barium titanate ceramics. *J Am Ceram Soc* 2005;**88**:3008–12.
19. Binner J, Annapoorani K, Paul A, Santacruz I, Vaidhyanathan B. Dense nanostructured zirconia by two stage conventional/hybrid microwave sintering. *J Eur Ceram Soc* 2008;**28**:973–7.
20. Mazaheri M, Zahedi AM, Sadrnezhaad SK. Two-step sintering of nanocrystalline ZnO compacts: effect of temperature on densification and grain growth. *J Am Ceram Soc* 2008;**91**:56–63.
21. Huang YH, Jiang DL, Zhang JX, Linz QL. Fabrication of transparent lanthanum-doped yttria ceramics by combination of two-step sintering and vacuum sintering. *J Am Ceram Soc* 2009;**92**:2883–7.
22. Li D, Chen SO, Shao WQ, Wang DC, Li YH, Long YZ, et al. Preparation of dense nanostructured titania ceramic using two step sintering. *Mater Technol* 2010;**25**:42–4.
23. Yang DY, Yoon DY, Kang SJL. Suppression of abnormal grain growth in WC-Co via two-step liquid phase sintering. *J Am Ceram Soc* 2011;**94**:1019–24.
24. Li JG, Ye YP. Densification and grain growth of Al_2O_3 nanoceramics during pressureless sintering. *J Am Ceram Soc* 2006;**89**:139–43.
25. Galusek D, Ghillanyova K, Sedlacek J, Kozankova J, Sajgalik P. The influence of additives on microstructure of sub-micron alumina ceramics prepared by two-stage sintering. *J Eur Ceram Soc* 2012;**32**: 1965–70.
26. Sedlacek J, Michalkova M, Karaman D, Galusek D, Hoffmann M. The influence of minor additives on densification and microstructure of sub-micrometer alumina ceramics prepared by SPS and HIP. *Ceram Trans* 2010;**209**:193–204.
27. Bennison SJ, Harmer MP. Effect of MgO solute on the kinetics of grain-growth in Al_2O_3. *J Am Ceram Soc* 1983;**66**:C90–2.
28. Jo W, Kim DY, Hwang NM. Effect of interface structure on the microstructural evolution of ceramics. *J Am Ceram Soc* 2006;**89**:2369–80.
29. Su HH, Johnson DL. Master sintering curve: a practical approach to sintering. *J Am Ceram Soc* 1996;**79**:3211–7.
30. Hansen JD, Rusin RP, Teng MH, Johnson DL. Combined-stage sintering model. *J Am Ceram Soc* 1992;**75**:1129–35.
31. Pouchly V, Maca K. Master sintering curve – a practical approach to its construction. *Sci Sinter* 2010;**42**:25–32.
32. Mazaheri M, Simchi A, Dourandish M, Golestani-Fard F. Master sintering curves of a nanoscale 3Y-TZP powder compacts. *Ceram Int* 2009;**35**:547–54.
33. Li D, Chen S, Shao WQ, Ge XH, Zhang YH, Zhang SS. Densification evolution of TiO_2 ceramics during sintering based on the master sintering curve theory. *Mater Lett* 2008;**62**:849–51.
34. Nikolic MV, Pavlovic VP, Pavlovic VB, Labus N, Stojanovic B. Application of the master sintering curve theory to non-isothermal sintering of $BaTiO_3$ ceramics. *Mater Sci Forum* 2005;**494**:417–22.
35. Blaine DC, Park SJ, German RM. Linearization of master sintering curve. *J Am Ceram Soc* 2009;**92**:1403–9.
36. An K, Han MK. Microstructural evolution based on the pressure-assisted master sintering surface. *Mater Sci Eng A: Struct* 2005;**391**:66–70.
37. Enneti RK, Bothara MG, Park SJ, Atre SV. Development of master sintering curve for field-assisted sintering of HfB_2–20SiC. *Ceram Int* 2012;**38**:4369–72.
38. Pouchly V, Maca K, Xiong Y, Shen JZ. Master sintering surface – a practical approach to its construction and utilization for spark plasma sintering prediction. *Sci Sinter* 2012;**44**:169–75.
39. An KJ, Han MK, Kim HJ. The pressure-assisted master sintering surface of metallic powder mixture. *Mater Trans* 2010;**51**:822–5.
40. Raether F, Horn PS. Investigation of sintering mechanisms of alumina using kinetic field and master sintering diagrams. *J Eur Ceram Soc* 2009;**29**:2225–34.
41. Kiani S, Pan J, Yeomans JA. A new scheme of finding the master sintering curve. *J Am Ceram Soc* 2006;**89**:3393–6.
42. Robertson IM, Schaffer GB. Refinement of master densification curves for sintering of titanium. *Met Mater Trans A* 2010;**41A**:2949–58.
43. Diantonio CB, Ewsuk KG, Bencoe D. Extension of master sintering curve theory to organic decomposition. *J Am Ceram Soc* 2005;**88**:2722–8.
44. Wang SY, Teng MH. Why a master sintering curve model can be applied to the sintering of nano-sized particles. *J Alloy Compd* 2010;**504**:S336–9.
45. Song XC, Lu J, Zhang TS, Ma J. Two-stage master sintering curve approach to sintering kinetics of undoped and Al(2)O(3)-doped 8 mol% yttria-stabilized cubic zirconia. *J Am Ceram Soc* 2011;**94**:1053–9.
46. Pouchly V, Maca K, Shen Z. Two-stage master sintering curve applied to two-step sintering of oxide ceramics. *J Eur Ceram Soc* 2013;**33**: 2275–83.
47. Wang JD, Raj R. Estimate of the activation-energies for boundary diffusion from rate-controlled sintering of pure alumina, and alumina doped with zirconia or titania. *J Am Ceram Soc* 1990;**73**:1172–5.
48. Bernard-Granger G, Guizard C, Addad A. Sintering of an ultra pure alpha-alumina powder: I. Densification, grain growth and sintering path. *J Mater Sci* 2007;**42**:6316–24.
49. Lallemant L, Roussel N, Fantozzi G, Garnier V, Bonnefont G, Douillard T, et al. Effect of amount of doping agent on sintering, microstructure and optical properties of Zr- and La-doped alumina sintered by SPS. *J Eur Ceram Soc* 2014;**34**:1279–88.
50. Ghillanyova K, Galusek D, Pentrak M, Madejova J, Bertoti I, Szepvolgyi J, et al. The influence of ageing on consolidation and sinterability of a sub-micron alumina powder. *Powder Technol* 2011;**214**:313–21.
51. Maca K, Trunec M, Chmelik R. Processing and properties of fine-grained transparent $MgAl_2O_4$ ceramics. *Ceram Silikaty* 2007;**51**:94–7.
52. Maca K, Pouchly V, Boccaccini AR. Sintering densification curve – a practical approach for its construction from dilatometric shrinkage data. *Sci Sinter* 2008;**40**:117–22.
53. Wurst JC, Nelson JA. Linear intercept technique for measuring grain-size in 2-phase polycrystalline ceramics. *J Am Ceram Soc* 1972;**55**:109.
54. Steele JH, Mccall JL. *Practical Applications of Quantitative Metallography. STP 839*. Philadelphia, PA: ASTM; 1984.
55. German RM. Coarsening in sintering: grain shape distribution, grain size distribution, and grain growth kinetics in solid-pore systems. *Crit Rev Solid State* 2010;**35**:263–305.
56. Bernard-Granger G, Guizard C. Apparent activation energy for the densification of a commercially available granulated zirconia powder. *J Am Ceram Soc* 2007;**90**:1246–50.

57. Kang S-JL. *Sintering, Densification, Grain Growth and Microstructure*. Amsterdam: Elsevier Butterworth-Heinemann; 2005.
58. Sumita S. A historical view of Al_2O_3 sintering with pore elimination. *Int J Soc Mater Eng Resour* 1996;**4**:103–16.
59. Fang TT, Shiue JT, Shiau FS. On the evaluation of the activation energy of sintering. *Mater Chem Phys* 2003;**80**:108–13.
60. Shao WQ, Chen SO, Li D, Cao HS, Zhang YC, Zhang SS. Apparent activation energy for densification of alpha-Al(2)O(3) powder at constant heating-rate sintering. *Bull Mater Sci* 2008;**31**:903–6.
61. Sethi G, Park SJ, Johnson JL, German RM. Linking homogenization and densification in W–Ni–Cu alloys through master sintering curve (MSC) concepts. *Int J Refract Met H* 2009;**27**:688–95.
62. Kellett BJ, Lange FF. Thermodynamics of densification. 1. Sintering of simple particle arrays, equilibrium-configurations, pore stability, and shrinkage. *J Am Ceram Soc* 1989;**72**:725–34.
63. Rahamann MN. *Sintering of Ceramics*. London: Taylor & Francis Group; 2008.
64. Mccune RC, Donlon WT, Ku RC. Yttrium segregation and yag precipitation at surfaces of yttrium-doped alpha-Al_2O_3. *J Am Ceram Soc* 1986;**69**:C196–9.
65. Cawley JD, Halloran JW. Dopant distribution in nominally yttrium-doped sapphire. *J Am Ceram Soc* 1986;**69**:C195–6.
66. Mayo MJ. Processing of nanocrystalline ceramics from ultrafine particles. *Int Mater Rev* 1996;**41**:85–115.

Journal of the European Ceramic Society 36 (2016) 2931–2936

Contents lists available at www.sciencedirect.com

Journal of the European Ceramic Society

journal homepage: www.elsevier.com/locate/jeurceramsoc

Sintering kinetic window for yttria-stabilized cubic zirconia

Vaclav Pouchly[a,1], Karel Maca[a,b,*]

[a] CEITEC, Brno University of Technology, Brno, Czech Republic
[b] Faculty of Mechanical Engineering, Brno University of Technology, Brno, Czech Republic

ARTICLE INFO

Article history:
Received 2 September 2015
Received in revised form
21 December 2015
Accepted 28 December 2015
Available online 12 January 2016

Keywords:
Cubic zirconia
Sintering
Grain growth
Activation energy

ABSTRACT

The influence of two pressure less sintering methods (single-step sintering and two-step sintering) on the final microstructure of cubic ZrO_2 was studied. Two different theoretical models were applied for the evaluation of the activation energies of sintering and grain growth. Consequently, the comparison of established activation energies allowed us to discuss the existence of sintering kinetic window where the grain growth is suppressed, while sintering is still active. The results show the sensitivity of microstructural evolution of c-ZrO_2 to the sintering temperature. The improved microstructure (i.e., the highest density and lowest grain size) of c-ZrO_2 was obtained, when low sintering temperature together with long dwell were applied irrespective of the sintering regime used.

1. Introduction

The preparation of advanced ceramic materials with improved properties is one of the most desirable goal in ceramic processing. Such enhancement is usually achieved with reaching the maximum density of ceramics accompanied by the minimum grain size. These parameters have overwhelming influence on the strength [1], hardness [2], toughness [3] and optical transparency [4,5] of ceramics. However, the increase of relative density of ceramic materials is mostly obtained via high-temperature sintering process. Unfortunately, elevated temperature simultaneously leads also to the grain growth. Chen and Wang [6] published a novel approach called two step sintering (TSS) and by this method they successfully sintered Y_2O_3 to full density without grain growth. TSS consists of two subsequent steps. In the first sintering step the material is heated with a constant heating rate until all pores become subcritical and unstable against shrinkage (75–92% of relative density). In the second step the temperature is decreased by tens, or even hundreds of °C and the sample is further sintered for a period of about tens of hours to full density. The temperature of second step of sintering must be adjusted to the value when the densification still proceeds, but the grain growth is frozen. Sintering without grain growth can be obtained due to the difference between the activation energy of sintering (Q_s) and activation energy of grain growth (Q_{gg}). The temperature interval, where Q_s is lower than Q_{gg} (i.e., sintering is active, while grain growth is limited), is called sintering kinetic window [7,8].

The TSS concept has so far been tested in many ceramic systems with different success rate. The c-ZrO_2 system was chosen for this study due to the highest reduction of grain size in available literature by a factor of 7 [9] or 2 [10,11], while for example TSS of t-ZrO_2 or Al_2O_3 lead to a reduction of the final grain size by a factor of 1.1 [10] or 1.3 [7], respectively. The aim of this work is to evaluate Q_s and Q_{gg} for c-ZrO_2 and to discuss the existence of kinetic window for this material.

2. Theoretical background

2.1. Master sintering curve

For the evaluation of Q_s most often the master sintering curve (MSC) [12] and the model of Wang and Raj [13] are used. MSC was derived by Johnson and co-workers in 90's [12,14] from the physical sintering models and is expressed by the following formula:

$$-\frac{dL}{Ldt} = \frac{\gamma\Omega}{kT}\left(\frac{\Gamma_v D_v}{G^3} + \frac{\Gamma_b \delta D_b}{G^4}\right), \quad (1)$$

where γ is the surface energy, Ω is the atomic volume, k is the Boltzmann constant, T is the thermodynamic temperature, G is the mean grain size, D is the coefficient of diffusion process (v for volume, b

* Corresponding author at: CEITEC, Brno University of Technology, Brno, Czech Republic. Fax: +420 541143202.
E-mail addresses: vaclav.pouchly@ceitec.vutbr.cz (V. Pouchly), maca@fme.vutbr.cz, karel.maca@ceitec.vutbr.cz (K. Maca).
[1] Fax: +420 541143202.

http://dx.doi.org/10.1016/j.jeurceramsoc.2015.12.044
0955-2219/

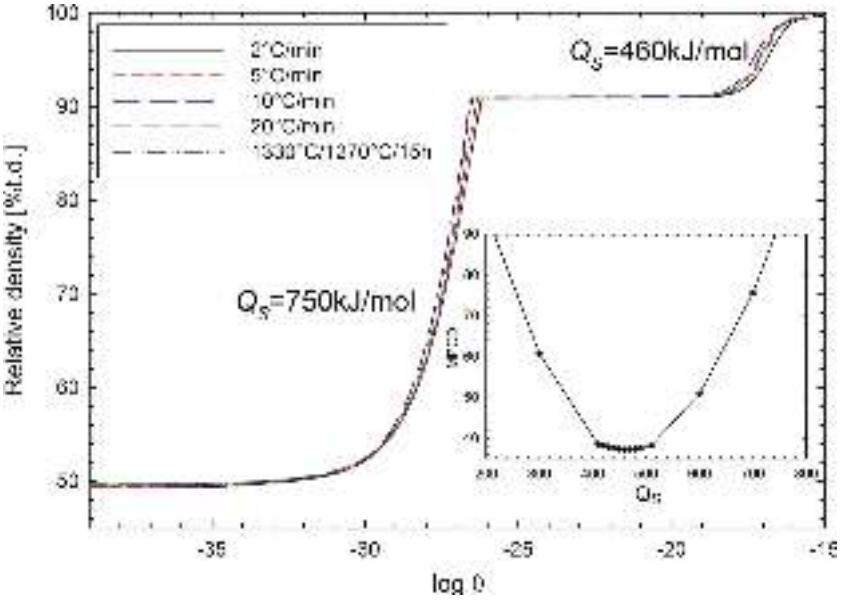

Fig. 1. Two-stage master sintering curve.

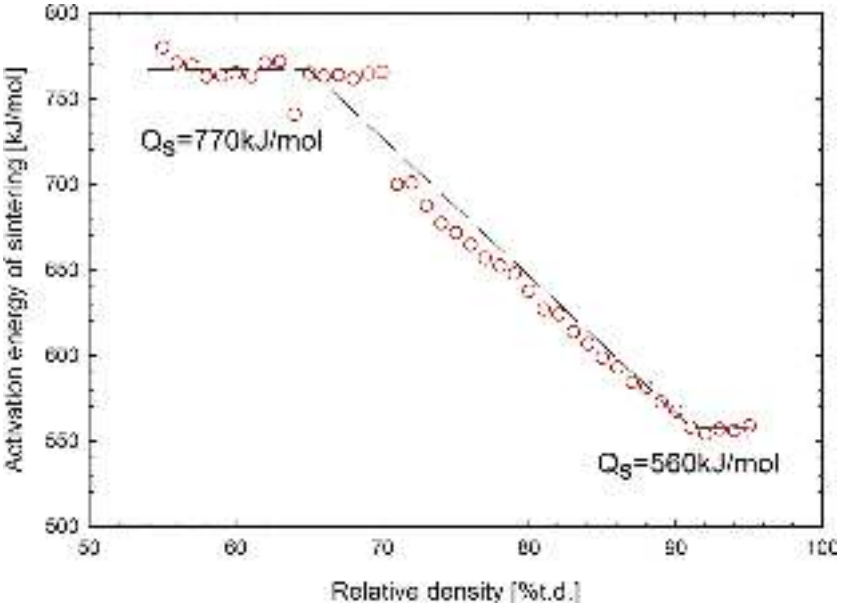

Fig. 2. Activation energy of sintering calculated from the model of Wang and Raj [13].

for boundary diffusion), Γ represents the scaling parameters that relate various geometric features, the driving force for sintering and the mean diffusion distance to the grain size, t is the time, δ is the width of grain boundary and L is the length of the sample.

In Eq. (1) two diffusion mechanisms are involved. If we assume that only one diffusion mechanism dominates the sintering process and the microstructure development (described by G and Γ) is a function of density only (regardless of used heating profile), then Eq. (1) can be rearranged to Eq. (2):

$$\frac{k}{\gamma\Omega\delta D_0}\int_{\rho_0}^{\rho}\frac{(G(\rho))^n}{3\rho\Gamma(\rho)}\mathrm{d}\rho=\int_0^t\frac{1}{T}\exp\left(-\frac{Q_S}{RT}\right)\mathrm{d}t\equiv\Theta, \tag{2}$$

where ρ is the sample density, D_0 is the coefficient of the diffusion process (only one dominant diffusion process is assumed) and n has the value of 3 (for volume diffusion) or 4 (for grain boundary diffusion). The temperature/time dependence of density expressed in Eq. (2) is called master sintering curve (MSC). MSC is unique for a given powder which is shaped by the same technology.

Q_S can be calculated from Eq. (2) by measuring few densification curves with different heating schedules. If the concept of MSC is valid, there should exist only one Q_S for which all curves $\rho_i = f(\Theta_i)$ overlap and create one "master curve" for all heating schedules i.

2.2. The Wang & Raj model

The model of Wang & Raj is based on the model of Young and Cutler [15]. According to their model the densification rate can be expressed by Eq. (3):

$$\frac{\mathrm{d}\rho}{\mathrm{d}t}=A\frac{e^{-Q_S/RT}}{T}\frac{f(\rho)}{G^n}, \tag{3}$$

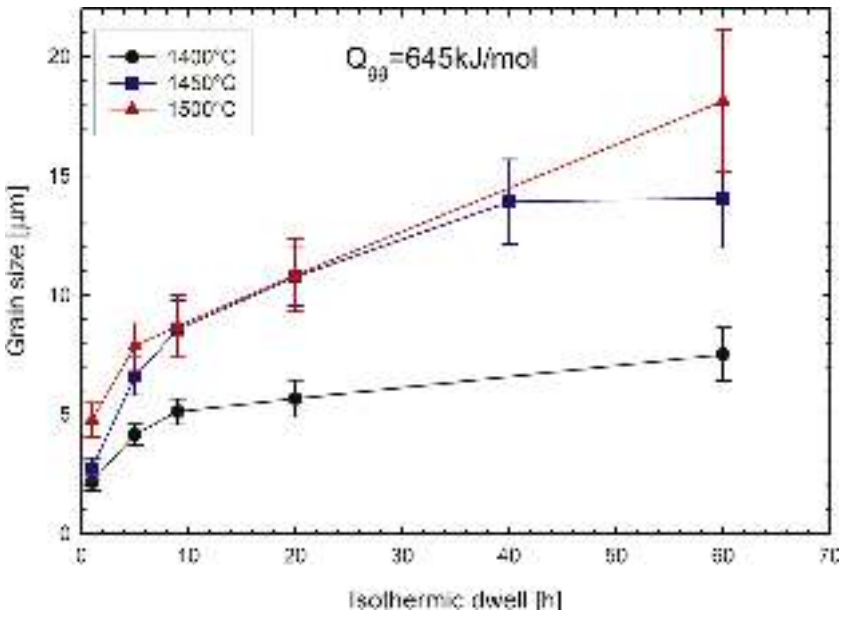

Fig. 3. Average grain size obtained after sintering at isothermal dwell time.

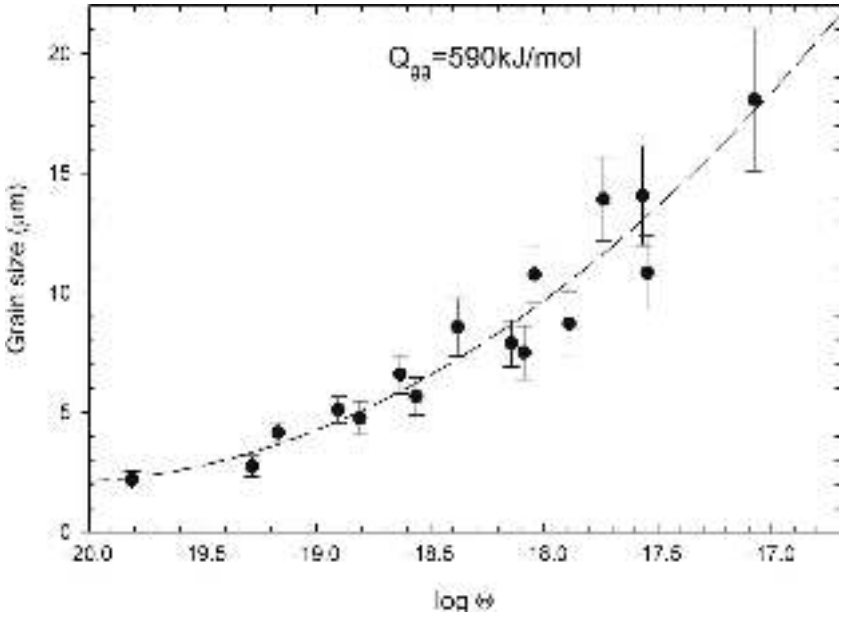

Fig. 4. Grain growth master curve.

where

$$A = \frac{C\gamma V^{2/3}}{R}, \tag{4}$$

and C is a constant, V is molar volume and $f(\rho)$ is a function of density only. The densification rate can be also expressed as:

$$\frac{d\rho}{dt} = \frac{d\rho}{dT}\frac{dT}{dt}. \tag{5}$$

Combining and taking a logarithm of Eqs. (3) and (5), we obtain Eq. (6):

$$\ln\left(T\frac{d\rho}{dT}\frac{dT}{dt}\right) = -\frac{Q_s}{RT} + \ln(f(\rho)) + \ln A - n\ln G. \tag{6}$$

If the left-hand side of the Eq. (6) is plotted against $1/T$, the slope of the line determines the activation energy of the sintering. However, the evaluation of Q_s is valid only if no grain growth occurs. Nevertheless, this model can still be applied to the higher densities, where grain growth is inconsiderable [16].

2.3. Grain growth kinetics

The Q_{gg} can be calculated from the grain growth kinetics equation, which is characterized by Eq. (7) [17]:

$$G_t^m - G_0^m = K_0 t \exp\left(-\frac{Q_{gg}}{RT}\right), \tag{7}$$

where G_t is the average grain size, G_0 is the initial grain size, m is the kinetic grain growth exponent (typically between 2 and 4 according to grain growth mechanism [17]) and K_0 is a pre-exponential constant.

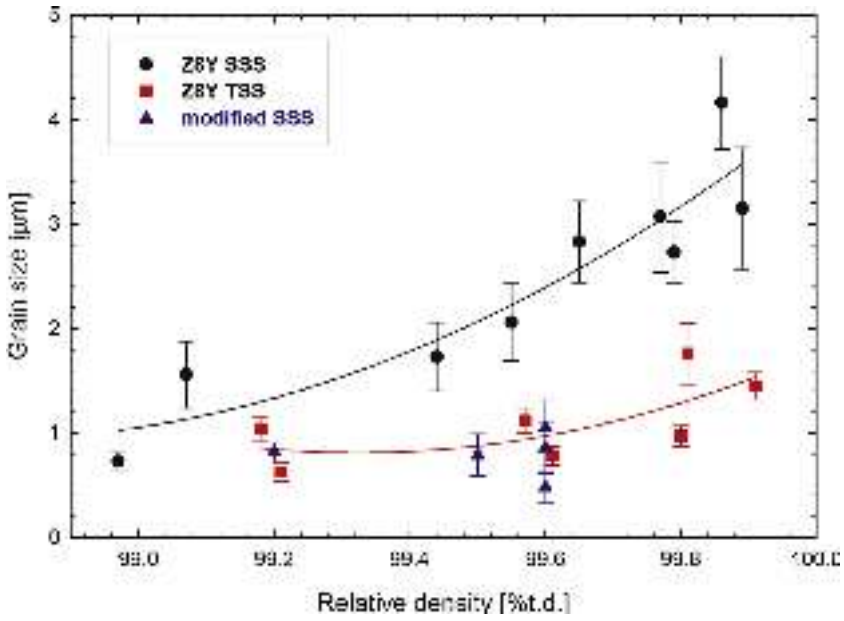

Fig. 5. The sintering trajectory of SSS, TSS and modified SSS heating schedule.

The other approach of calculating Q_{gg}, is a method of grain growth master curve (GGMC) [18]. Similar to MSC theory, the Q_{gg} can be obtained from Eq. (7):

$$f(G) = \int_0^t \exp\left(-\frac{Q_{gg}}{RT}\right) \mathrm{d}t \equiv \Theta_{gg}. \tag{8}$$

The Q_{gg} may be found when all grain sizes G_j for all samples j are located at one curve $f(\Theta_{ggj})$.

3. Experimental

3.1. Materials

ZrO_2 powder with 8 mol.% of Y_2O_3 (TZ8Y grade, Tosoh, Japan) was used for all experiments. The particle size for TZ8Y was estimated as 70 nm (BET method, ChemBet 3000, Quantachrome, USA) with the assumption of unimodal spherical particles and taking 5.99 g cm^{-3} for the theoretical density of c-ZrO_2.

3.2. Preparation of ceramic green bodies

Discs with diameter 30 mm and ~5 mm in height were prepared via cold isostatic pressing (CIP). Pressing was carried out in an isostatic press (Autoclave Engineering, Inc., USA) at a pressure of 300 MPa with a dwell time of 5 min. The CIPed samples were presintered at 800 °C/1 h, than cut and ground into the shape of prisms with dimensions 4 × 4 × 15 mm.

3.3. Sintering of ceramic bodies

TSS and conventional single-step sintering (SSS) experiments were performed in a superkanthal resistance furnace (K1700/1, Heraeus, Germany) with the heating rate of 10 °C/min up to 800 °C and then 5 °C/min up to the sintering temperature. In the case

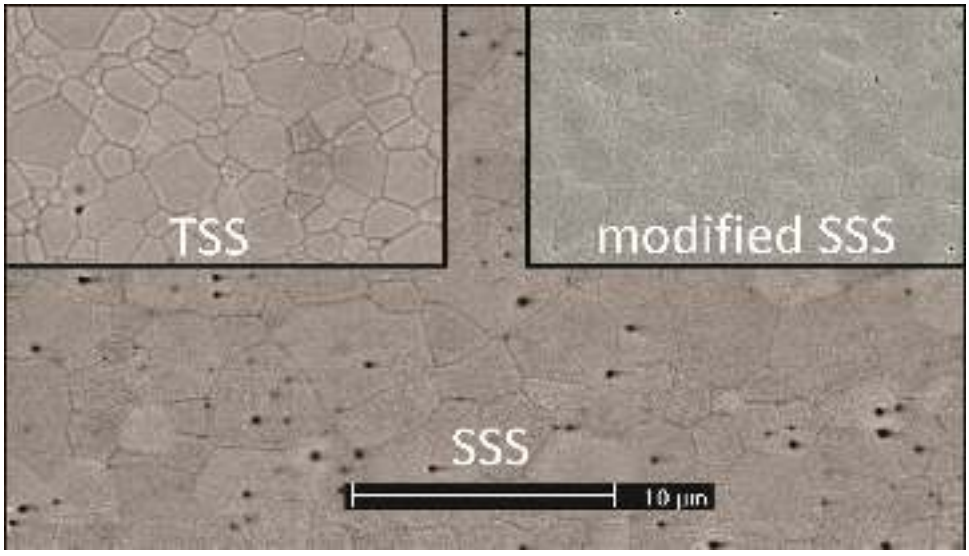

Fig. 6. Microstructure of samples sintered by SSS, TSS and modified SSS (the relative density of all samples was 99.6% of t.d.).

Table 1
Microstructure properties of selected samples sintered by SSS and TSS.

Single-step sintering				Two-step sintering				Reduction factor
Sintering [°C/h]	ρ_{rel} [% t.d.]	D [μm]	s/n [μm/−]	Sintering [°C/ °C/h]	ρ_{rel} [% t.d.]	D [μm]	s/n [μm/−]	D_{SSS}/D_{TSS} [−]
1500/0	99.07	1.56	0.32/25	1330/1270/5	99.21	0.63	0.09/25	2.5
1530/0.17	99.65	2.83	0.39/25	1330/1270/10	99.61	0.78	0.09/25	3.6
1500/2	99.86	3.15	0.58/25	1330/1300/15	99.91	1.45	0.13/25	2.2

Note: s is standard deviation and n is number of measurement.

of TSS, the cooling rate between the first and second step was 60 °C/min.

3.4. Calculation of activation energies

To obtain a data for the calculation of Q_s, the samples were sintered in a high-temperature dilatometer (L70/1700, Linseis, Germany) with a heating rate 2, 5, 10 and 20 °C/min in air atmosphere. The shrinkage curves were recalculated to the densification profiles. The details of such recalculation are described elsewhere [19]. The construction of MSCs were provided by a specialized software Density MSC with the use of Mean Perpendicular Curve Distance as a criterion for finding the optimal Q_s [20]. The calculation of the values of Q_s according to Wang & Raj model is described elsewhere [21]. The EXCEL® was used for the calculation of Eqs. (7) and (8).

3.5. Microstructural characterization of sintered samples

The final relative densities of samples (ρ_{rel}) were determined on the basis of Archimedes' principle (EN 623-2) with distilled water as a liquid media. The samples were then ground and polished by standard ceramographic methods and thermally etched to expose the grain boundaries. The microstructure of samples was studied using scanning electron microscopy (Philips XL 30, the Netherlands). The grain size was estimated by the linear intercept method (EN 623-3) using the correlation factor of 1.56.

4. Results

4.1. Effect of two-step sintering on final microstructure

The temperature of the first step of TSS was determined from dilatometric measurements in the temperature range from 1300 to 1360 °C, where the samples can reach the required 75–92% of theoretical density. The temperature of SSS was set with the aim to obtain the same relative densities as with TSS regimes, but the dwell time was limited to max. 2 h. The selected sintering temperatures, dwell times and obtained densities and grain sizes are summarized in Table 1. The results show that for the same relative densities significant reduction of final grain size was obtained by TSS, e.g., for the samples with the highest relative density (99.9% t.d.) it was by the factor of 2.2.

4.2. Determination of the activation energy of sintering

For the evaluation of Q_s the two stage master sintering curve (TS-MSC) was performed [22]. The MSC was split into two regions below and above the temperature of the first step of TSS (1330 °C). The result of constructed TS-MSC is shown in Fig. 1. The value of Q_s was 750 kJ/mol for the low density region and 460 kJ/mol for the high density region.

The results of Q_s calculated from Wang & Raj model are shown in Fig. 2. The obtained Q_s can be divided into three regions. In the low temperature region (up to 70% t.d.), the Q_s is 770 kJ/mol, in the transition region (70–90% t.d.) the Q_s linearly decreases, and in the high density region (90–96% t.d.) the Q_s is 560 kJ/mol.

4.3. Determination of grain growth kinetics

To obtain data for the determination of Q_{gg}, the sintering was carried out at 1400, 1450 and 1500 °C with dwell times 1, 5, 9, 20 and 60 h. The obtained grain sizes after sintering for different temperatures and dwells are shown in Fig. 3. It is evident that the grain growth was fast in the first 5 h of dwell at all temperatures. After 9 h of dwell the grain growth rate decreased.

First the grain growth data were fitted by the grain growth kinetic model (according to Eq. (7)) in order to obtain the grain growth exponent m. The value of $m = 3$ was obtained, which corresponds to grain growth in the presence of solutes [17]. This can be explained by the solution of Y^{3+} ions in ZrO_2 matrix. Using this value of m in Eq. (7) the activation energy Q_{gg} was calculated as 645 kJ/mol.

The grain growth data fitted by the model of grain growth master curve (see Eq. (8)) are shown in Fig. 4. The activation energy Q_{gg} established from GGMC model was 590 kJ/mol.

5. Discussion

The differences in grain sizes after sintering of Z8Y powder by SSS or TSS method are summarized in Table 1 and the results show that smaller grains were obtained by TSS. The decrease of grain size by a factor of 2.2 is comparable with the factor of 2.0 obtained in our previous work for c-ZrO_2 with double particle size (140 nm) [10]. Such decrease of final grain size after TSS indicates that most probably we have found the area of kinetic window. The reason why the TSS method is effective especially for cubic systems [6,9,11] is still not clear. One of the possible explanation can be the existence of faceted boundaries in such symmetric systems [23].

Table 2
Overview of calculated activation energies.

Density region	Q_s (kJ/mol)		Q_{gg} (kJ/mol)	
	Master sintering curve	Wang and Raj model	Grain growth kinetic equation	Grain growth master curve
Low density	750	770	645	590
High density	460	560		

In this work we have tried to describe the existence of kinetic window by the comparison of Q_s and Q_{gg}, which were calculated always by two independent models (Table 2). The results of both applied sintering models indicate that the Q_s in high density region is lower than in low density region. Such decrease of Q_s in a final stage of sintering was already observed by Bernard-Granger and Guizard [24] and by Song et al. [25]. The activation energies of sintering obtained in this work (Table 2) are in good agreement with the values firstly published by Song et al. [25]. In this work we verify these results also by another model (Wang & Raj).

Based on our results we believe that application of TS-MSC better reflects the densification mechanisms than elementary MSC. The Q_s at the lower densities can be influenced by surface diffusion, which is decreasing the driving force of densification [25,26]. On the other hand in the final stage of sintering (high densities) the total area of grain boundaries increases significantly, therefore diffusion processes proceed along shorter diffusion path which can also contribute to the decrease of the Q_s [16]. This hypothesis is fully supported by the results of Q_s evaluated by Wang & Raj model. Moreover, the determined Q_s in the high density region is in agreement with the activation energy of lattice diffusion of Zr ions in c-ZrO_2 [27].

The Q_s evaluated for high density region is lower than Q_{gg}. The observed difference in activation energies corroborates with the existence of kinetic window of this material, since the densification was provided by TSS, but the grain growth was hindered. The sintering and the grain growth mechanisms are both diffusion controlled processes with Arrhenius-type dependency with respect to the temperature. In the diffusion-controlled processes the kinetics is determined by the slowest, rate-limiting step i.e., atoms/ions movement along the fastest diffusion path [28]. To exploit the kinetic window, it should be enough to reduce the sintering temperature to the level, where thermodynamics conditions will not allow grain growth, but will be still sufficient for densification. Based on this knowledge, in our following experiments we sintered TZ8Y green bodies via SSS, but employing lower sintering temperatures and longer dwell times. The sintering temperatures were comparable to the temperatures used for the second step of TSS, however, the dwell times were prolonged up to 60 h to obtain comparative densities as via TSS. The results of these sintering experiments are shown in Figs. 5 and 6.

Using this modified SSS sintering we have achieved same decrease in the final grain sizes as in the case of TSS. Evidently, modified SSS is benefitted from the same kinetic window. These findings do not neglect the benefit of the TSS procedure, but it informs about the decreased temperature at second step of TSS which is more important than entire first step of TSS. The TSS sintering has the advantage to obtain the same microstructures much faster due to the first preheating step, during which the grain growth is still suppressed on the account of the presence of the pores along grain boundaries and the pore pinning effect.

6. Conclusions

Cubic ZrO_2 powder doped with 8 mol.% of Y_2O_3 was sintered via single-step sintering (SSS) and two-step sintering (TSS) techniques. The results show that the final microstructure of c-ZrO_2 is sensitive to the used heating profile. Choosing the heating profiles with lower sintering temperature and longer dwell led to the finer final microstructure of c-ZrO_2 regardless if SSS or TSS were used. These results were supported by finding the sintering kinetic window through the evaluation of the activation energies of sintering by the master sintering curve model and Wang & Raj model. The activation energy of grain growth was determined using the grain growth kinetic model and grain growth master curve model.

Acknowledgements

The authors acknowledge the support of the Grant agency of the Czech Republic under grant no. 15-06390S. This work was realized in CEITEC—Central European Institute of Technology with research infrastructure supported by the project CZ.1.05/1.1.00/02.0068 financed from European Regional Development Fund.

References

[1] A. Krell, P. Blank, The influence of shaping method on the grain size dependence of strength in dense submicrometre alumina, J. Eur. Ceram. Soc. 16 (1996) 1189–1200.
[2] A. Krell, P. Blank, Grain-size dependence of hardness in dense submicrometer alumina, J. Am. Ceram. Soc. 78 (1995) 1118–1120.
[3] A. Kocjan, V. Pouchly, Z.J. Shen, Processing of zirconia nanoceramics from a coarse powder, J. Eur. Ceram. Soc. 35 (2015) 1285–1295.
[4] O.Y.T. Koo JB, K.J. Hong, J.S. Park, D.C. Shin, Effect of grain size on transmittance and mechanical strength of sintered alumina, Mater. Sci. Eng. A: Struct. 374 (2004) 191–195.
[5] R. Apetz, M.P.B. Van Bruggen, Transparent alumina: a light-scattering model, J. Am. Ceram. Soc. 86 (2003) 480–486.
[6] I.W. Chen, X.H. Wang, Sintering dense nanocrystalline ceramics without final-stage grain growth, Nature 404 (2000) 168–171.
[7] K. Bodisova, P. Sajgalik, D. Galusek, P. Svancarek, Two-stage sintering of alumina with submicrometer grain size, J. Am. Ceram. Soc. 90 (2007) 330–332.
[8] D. Galusek, K. Ghillanyova, J. Sedlacek, J. Kozankova, P. Sajgalik, The influence of additives on microstructure of sub-micron alumina ceramics prepared by two-stage sintering, J. Eur. Ceram. Soc. 32 (2012) 1965–1970.
[9] M. Mazaheri, M. Valefi, Z.R. Hesabi, S.K. Sadrnezhaad, Two-step sintering of nanocrystalline $8Y_{(2)}O_{(3)}$ stabilized $ZrO_{(2)}$ synthesized by glycine nitrate process, Ceram. Int. 35 (2009) 13–20.
[10] K. Maca, V. Pouchly, P. Zalud, Two-step sintering of oxide ceramics with various crystal structures, J. Eur. Ceram. Soc. 30 (2010) 583–589.
[11] K. Maca, V. Pouchly, Z.J. Shen, Two-step sintering and spark plasma sintering of Al_2O_3, ZrO_2 and $SrTiO_3$ ceramics, Integr. Ferroelectr. 99 (2008) 114–124.
[12] H.H. Su, D.L. Johnson, Master sintering curve: a practical approach to sintering, J. Am. Ceram. Soc. 79 (1996) 3211–3217.
[13] J.D. Wang, R. Raj, Estimate of the activation-energies for boundary diffusion from rate-controlled sintering of pure alumina, and alumina doped with zirconia or titania, J. Am. Ceram. Soc. 73 (1990) 1172–1175.
[14] J.D. Hansen, R.P. Rusin, M.H. Teng, D.L. Johnson, Combined-stage sintering model, J. Am. Ceram. Soc. 75 (1992) 1129–1135.
[15] W.S. Young, I.B. Cutler, Initial sintering with constant rates of heating, J. Am. Ceram. Soc. 53 (1970) 659–663.
[16] K. Maca, V. Pouchly, K. Bodisova, P. Svancarek, D. Galusek, Densification of fine-grained alumina ceramics doped by magnesia, yttria and zirconia evaluated by two different sintering models, J. Eur. Ceram. Soc. 34 (2014) 4363–4372.
[17] M.J. Mayo, Processing of nanocrystalline ceramics from ultrafine particles, Int. Mater. Rev. 41 (1996) 85–115.
[18] I.M. Robertson, G.B. Schaffer, Refinement of master densification curves for sintering of titanium, Metall. Mater. Trans. A 41A (2010) 2949–2958.
[19] K. Maca, V. Pouchly, A.R. Boccaccini, Sintering densification curve—a practical approach for its construction from dilatometric shrinkage data, Sci. Sinter. 40 (2008) 117–122.
[20] V. Pouchly, K. Maca, Master sintering curve—a practical approach to its construction, Sci. Sinter. 42 (2010) 25–32.
[21] J. Hruby, V. Pouchly, K. Maca, A practical approach for the calculation of the activation energy of the sintering, Sci. Sinter. (2016) (accepted).
[22] V. Pouchly, K. Maca, Z. Shen, Two-stage master sintering curve applied to two-step sintering of oxide ceramics, J. Eur. Ceram. Soc. 33 (2013) 2275–2283.
[23] M.G. Lee, S.Y. Chung, S.J.L. Kang, Boundary faceting-dependent densification in a $BaTiO_3$ model system, Acta Mater. 59 (2011) 692–698.
[24] G. Bernard-Granger, C. Guizard, Apparent activation energy for the densification of a commercially available granulated zirconia powder, J. Am. Ceram. Soc. 90 (2007) 1246–1250.
[25] X.C. Song, J. Lu, T.S. Zhang, J. Ma, Two-stage master sintering curve approach to sintering kinetics of undoped and $Al_{(2)}O_{(3)}$-doped 8 mol% yttria-stabilized cubic zirconia, J. Am. Ceram. Soc. 94 (2011) 1053–1059.
[26] G. Sethi, S.J. Park, J.L. Johnson, R.M. German, Linking homogenization and densification in W–Ni–Cu alloys through master sintering curve (MSC) concepts, Int. J. Refract. Metals Hard Mater. 27 (2009) 688–695.
[27] M.A. Taylor, M. Kilo, G. Borchardt, S. Weber, H. Scherrer, Zr-96 diffusion in polycrystalline scandia stabilized zirconia, J. Eur. Ceram. Soc. 25 (2005) 1591–1595.
[28] S.-J.L. Kang, Sintering, Densification, Grain Growth & Microstructure, Elsevier Butterworth-Heinemann, 2005.

Journal of the European Ceramic Society 37 (2017) 4287–4295

Contents lists available at www.sciencedirect.com

Journal of the European Ceramic Society

journal homepage: www.elsevier.com/locate/jeurceramsoc

Dilatometric study of anisotropic sintering of alumina/zirconia laminates with controlled fracture behaviour

Karel Maca[a,b,*], Vaclav Pouchly[a,b], Daniel Drdlik[a,b], Hynek Hadraba[c], Zdenek Chlup[c]

[a] CEITEC BUT, Brno University of Technology, Purkynova 123, 61669 Brno, Czech Republic
[b] Institute of Materials Science and Engineering, Brno University of Technology, Technicka 2896/2, 61669 Brno, Czech Republic
[c] CEITEC IPM, Institute of Physics of Materials, Academy of Sciences of the Czech Republic, Zizkova 513/22, 61662 Brno, Czech Republic

ARTICLE INFO

Article history:
Received 22 January 2017
Received in revised form 10 April 2017
Accepted 11 April 2017
Available online 23 April 2017

Keywords:
Alumina/zirconia laminate
Sintering shrinkage
Master sintering curve
Crack deflection

ABSTRACT

Al_2O_3 and ZrO_2 monoliths as well as layered Al_2O_3/ZrO_2 composites with a varying layer thickness ratio were prepared by electrophoretic deposition. The sintering shrinkage of these materials in the transversal (perpendicular to the layers, i.e. in the direction of deposition) as well as in the longitudinal (parallel with layers interfaces) direction were monitored using high-temperature dilatometry. The sintering of layered composites exhibited anisotropic behaviour. The detailed study revealed that sintering shrinkage in the longitudinal direction was governed by alumina (material with a higher sintering temperature), whilst in the transversal direction it was accelerated by the directional sintering of zirconia layers. For interpretation of such anisotropic sintering kinetics, the Master Shrinkage Curve model was developed and applied. Crack propagation through laminates with a different alumina/zirconia thickness ratio was described with the help of scanning electron microscopy and confocal laser microscopy.

1. Introduction

Layered ceramic composites (laminates) can be prepared by various techniques like tape casting, slip casting, or electrophoretic deposition (EPD). EPD is an experimentally simple and cheap method enabling the formation of deposits from stable suspensions. EPD is a powerful method for the preparation of ceramic laminates [1,2], but also of monoliths [3] or structural composites such as particle mixed composites and functionally gradient materials [4–6]. In the last decades, ceramic laminates have been one of the main areas of focus for material scientists particularly for their crack deflection behaviour [7,8].

Internal stresses are responsible for unique crack propagation in ceramic laminates [9]. The tension arising during sintering is usually described by the constrained sintering model. Unfortunately, this model is designed for the sintering of one layer on a rigid substrate [10]. However, laminate composites consist of hundreds of individual layers supporting each other. Constrained sintering causes hindering of sintering and very often the generation of cracks, or crack like defects [11,12]. Additionally, internal stresses that are due to a mismatch in the coefficient of thermal expansion (CTE) are generated during cooling as well [11].

The magnitude of residual tensile stress (σ_r) in the ZrO_2 layer can be calculated using the following relation [9,13].

$$\sigma_{rZrO_2} = \frac{(\alpha_{ZrO_2} - \alpha_{Al_2O_3}) \cdot \Delta T \cdot E_{ZrO_2}}{1 - \upsilon_{ZrO_2}} \cdot \left(1 + \frac{d_{ZrO_2}}{d_{Al_2O_3}} \cdot \frac{E_{ZrO_2} \cdot (1 - \upsilon_{Al_2O_3})}{E_{Al_2O_3} \cdot (1 - \upsilon_{ZrO_2})}\right)^{-1}, \quad (1)$$

where d is the layer thickness, α is the coefficient of linear thermal expansion, ΔT is the difference between the sintering and the current temperature, ν is Poisson's ratio, and E is the modulus of elasticity. Stress in the Al_2O_3 phase can be obtained analogously. In contrast with ZrO_2, stress in the alumina layer is compressive. The stresses are directed parallel with the interfaces.

For a better understanding of the fracture properties of ceramic laminates, the detailed study of crack propagation in laminates with various values of internal stresses appears appropriate. It follows from Eq. (1) that internal stresses can be designed by the proper choice of thicknesses ratio of individual layers. To tailor the thicknesses of the layers in the final laminate, the exact control of the deposition kinetics as well as sintering shrinkage is needed. Since the detailed study of deposition kinetics was presented in our previous papers [1,14], the goal of this work is the study of sintering behaviour carried out with the help of high-temperature dilatometry [15].

The concept of Master Sintering Curve (MSC in the following) is a good engineering tool for optimizing and predicting the sintering

* Corresponding author at: CEITEC BUT, Brno University of Technology, Purkynova 123, 61669 Brno, Czech Republic.
E-mail address: karel.maca@ceitec.vutbr.cz (K. Maca).

http://dx.doi.org/10.1016/j.jeurceramsoc.2017.04.030
0955-2219/

process which can also be used for the determination of sintering activation energy [16]. The MSC model was derived under conditions of validity of some geometrical and physical conditions [16] and it is used in the form of relation between density and function Θ (describing the thermal history of the sintering with the help of parameter Q):

$$\frac{k}{\gamma\Omega D_0}\int_{\rho_0}^{\rho}\frac{(G(\rho))^n}{3\rho\Gamma(\rho)}d\rho \equiv f(\rho) = \int_0^t \frac{1}{T}\exp\left(-\frac{Q}{RT}\right)dt \equiv \Theta, \quad (2)$$

where γ is the surface energy, Ω is the atomic volume, k is the Boltzmann constant, R is the gas constant, T is the thermodynamic temperature, G is the mean grain size, D_0 is the coefficient of a diffusion process (only one dominant diffusion process is considered), Γ represents scaling parameters that relate different geometric features as the driving force of sintering and the mean diffusion distance to the grain size, t is the time, ρ is sample density, Q is the activation energy of sintering, and n has a value of 3 (for volume diffusion) or 4 (for grain boundary diffusion).

Not only does the construction of MSC require several sintering experiments performed at different heating schedules, but also time consuming mathematical iteration. Recently, some mathematical approaches enabling the easy construction of MSC from few dilatometric sintering experiments have been published [17,18], shown by the dramatic rise of references being made to MSC in the literature. The basic MSC model has already been modified for many special purposes. An and Han [19,20] extended the MSC model to pressure-assisted sintering and Enneti et al. to field-assisted sintering [20,21]. An et al. [22] and Raether et al. [23] used the MSC model for construction of sintering kinetics diagrams. Di Antonio et al. [24] and Wang et al. [25] showed that MSC can be extended to all Arrhenius type equations. Recently, Song et al. [26] and Pouchly et al. [27] showed that MSC can also be used for the description of sintering behaviour when the change of the controlling sintering mechanism has to be taken into account.

The limitations of the MSC model arise when a more complicated sintering material is examined. For example, in the case of a lamellar composite, the shrinkage is not isotropic [28], and therefore the geometrical assumption of the MSC model is not fulfilled [29]. The densification curve of the sample cannot be calculated from one-dimensional dilatometric shrinkage. Hence, the second goal of this work is modification of the MSC model from density related to shrinkage related. Such a modified MSC can then be applied to lamellar composites with the aim to use the results of such analysis for the description of processes which occur during sintering.

For this study, the Al_2O_3/ZrO_2 laminates prepared by EPD were chosen since the authors have much experience with the preparation of these laminates with strongly bonded layers. Using sintered composites with various layer designs, the crack propagation was demonstrated and discussed.

Table 1
Ceramic powder materials used for electrophoretic deposition.

Material	Manufacturer	Grade	Mean particle size[a] [μm]
Al_2O_3	Malakoff Ind., USA	HP-DBM	0.47
ZrO_2	Tosoh, Japan	TZ-3YS-E	0.14

[a] Values were calculated from specific surface area given by the producer.

2. Experimental

2.1. Electrophoretic deposition

For preparation of ceramic monoliths and laminates, alumina and tetragonal zirconia (stabilized by 3 mol% of Y_2O_3) powders were used. Detailed information about ceramic powders is shown in Table 1. Suspensions contained 15 wt.% of alumina or zirconia, 12.75 wt.% of monochloroacetic acid (99%, Aldrich, Germany) used as a stabilizer and 72.25 wt% of the dispersion medium – 2-propanol (p.a., Onex, Czech Republic).

Electrophoretic deposition was performed in an electrophoretic glass cell with the constant current mode of 5 mA. The distance between stainless steel electrodes with an effective area of 18.2 cm^2 was set to 26 mm. In order to prevent particles from settling on the bottom of the EPD cell, the suspension was repeatedly stirred every 5 min during electrophoretic deposition. The repeated transfer of the deposition electrode from the alumina to the zirconia suspension (and vice versa) enabled the preparation of ceramic laminates with about 100 alternating alumina and zirconia layers with a thickness ratio of 2:1, 1:1, and 1:2 (denoted as Z33, Z50, and Z67, respectively). The precise control of deposition kinetics enabled the preparation of ceramic laminates with well defined thicknesses of individual layers [30]. For comparison, alumina (denoted as A), and zirconia (denoted as Z) monoliths were prepared during 90 min and 140 min long depositions, respectively. A detailed description of all prepared deposits is given in Table 2. All deposits were dried after the deposition for at least 24 h at room temperature. After the drying, the deposits were annealed at 800 °C/1 h in air.

2.2. Sintering of ceramic samples and constructing of the modified MSC

The sintering of the test samples was done in a contact high-temperature dilatometer (L70/1700, Linseis, Germany), where the sample shrinkage was in-situ monitored both in the transversal direction (perpendicular to alumina/zirconia interfaces, i.e. parallel to the direction of deposition) as well as in the longitudinal one (parallel to alumina/zirconia interfaces, i.e. perpendicular to the direction of deposition). Samples were cut from the deposits in the shape of prismatic bars, with a cross-section ca 4 × 4 mm, height ca 10 mm (longitudinal sample) resp. ca 5 mm (transversal sample).

The coefficient of thermal expansion (α) of all the samples was calculated according to Eq. (3):

$$\alpha = \frac{\varepsilon_{room} - \varepsilon_{T\max}}{(T_{room} - T_{\max})\cdot 100}, \quad (3)$$

Table 2
Characteristics of deposited and sintered samples.

Laminate	Al_2O_3/ZrO_2 thickness [μm/μm]	ZrO_2 content [vol%]	Green density [%TD]	Final density [%TD]	Grain size Al_2O_3/ZrO_2 [μm/μm]	Final shrinkage	
						T [%]	L [%]
A	50/0	0	62.0	99.40	1.3/-	17.5	14.2
Z33	50/25	33.3	57.3	99.20	1.6/0.6	22.7	14.9
Z50	50/50	50.0	55.0	99.57	1.2/0.4	24.2	15.4
Z67	25/50	66.7	52.7	98.02	1.6/0.6	27.2	16.1
Z	0/50	100	48.0	99.92	-/0.3	22.4	21.4

Note: T = transversal, L = longitudinal.

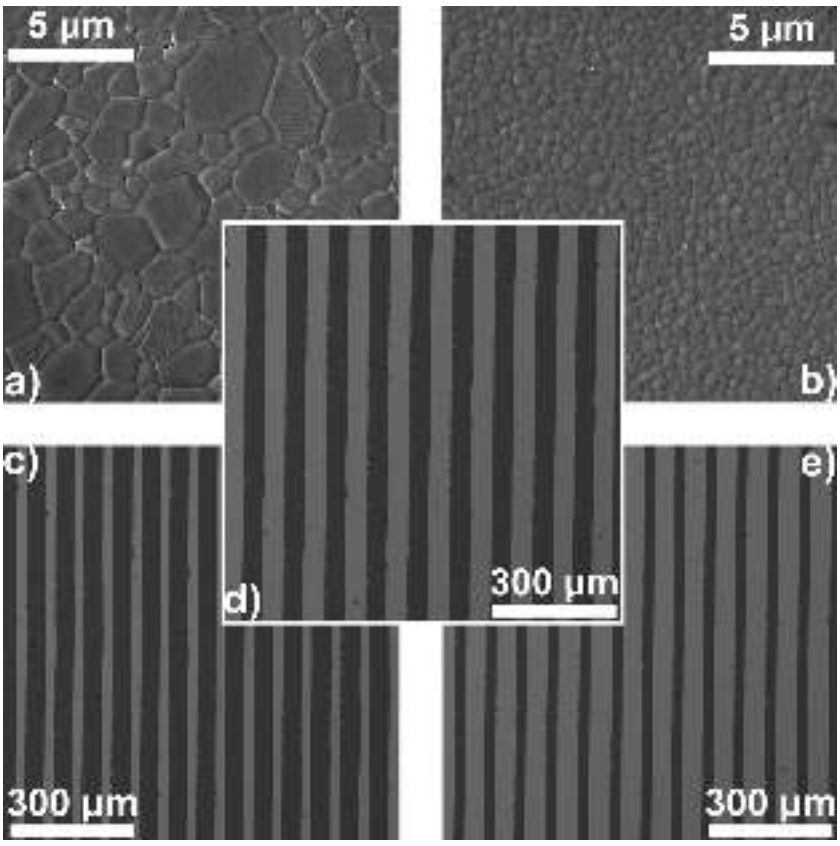

Fig. 1. Microstructure of sintered materials a) A, b) Z, c) Z33 d) Z50 e) Z67. In the case of composites, the bright layers consist of zirconia and the dark ones of alumina.

where ε_{room} is the shrinkage after cooling, ε_{Tmax} is the shrinkage at the end of the dwell, T_{room} is the temperature after cooling, and T_{max} is the temperature at the end of the dwell.

Knowing the values of α, the sample length changes caused by thermal dilatation can be eliminated which leads to so called sintering shrinkage:

$$\varepsilon(t, T) = \varepsilon_{instant}(t, T) - \alpha \cdot 100 \cdot (T - T_{room}), \quad (4)$$

where $\varepsilon_{instant}$ (t,T) is instantaneous measured shrinkage, t is time, and T is actual temperature.

The sintering was performed at 1500 °C and 2 h dwell with a heating rate of 10 °C/min and a cooling rate of 5 °C/min. In order to obtain different heating profiles for MSC construction, samples A, Z50, and Z were also sintered with heating rates of 2, 5, and 20 °C/min. All calculations associated with the modified MSC model were performed with the help of an automatic procedure which uses Mean Perpendicular Curves Distance (MPCD) for estimating the best overlap of individual curves [17]. This procedure was in this work adjusted for analysis of sintering shrinkage. The 95% confidence interval for sintering activation energy Q was established by fitting of MPCD = f(Q) dependence using the weighted nonlinear regression.

2.3. Microstructure of sintered samples

Green as well as final densities of layered monoliths and composites were determined using Archimedes' method (EN 623-2) with distilled water as a liquid media. The theoretical densities (TD) used for the relative densities calculation were 3.99 g cm^{-3} for alumina and 6.08 g cm^{-3} for zirconia. Theoretical densities of laminates were calculated by a rule of mixtures according to the volume fractions of alumina and zirconia. The samples were ground and polished by the standard ceramographic methods and then thermally etched at 1400 °C for 5 min (heating rate of 20 °C/min) to expose the grain boundaries. The microstructure of the samples was examined using scanning electron microscopy (Lyra 3, Tescan, Czech Republic). The grain size was estimated by the linear intercept method (EN 623-3) with a correction factor of 1.56. Minimum of 250 grains were measured at magnifications 15kx and 30kx for alumina and zirconia, respectively.

2.4. Fracture behaviour of laminates

Crack propagation in laminates was observed on the fracture surfaces of fracture toughness experiments using the Single Edge V-Notch Beam (SEVNB in the following) technique. The test samples had a shape of bars with a rectangular cross-section and a starting notch was prepared using a razor blade and subsequent application of diamond paste. The typical notch radius reached by described technique was about 10 µm. Note that notch radius had no influence on subsequent crack propagation. The loading of the samples of nominal dimensions 2×1.6 mm was conducted in a three point bending configuration with the span of 10 mm aiming to have a controlled stress field in the vicinity of the notch. A confocal laser microscope (LEXT OLS 3100, Olympus, Japan) was employed for the fractographic observations, 3D surface reconstruction, and measurements.

3. Results and discussion

3.1. Microstructure properties of sintered materials

Fig. 1 shows the microstructure of sintered ceramic samples A, Z33, Z50, Z66, and Z. The final relative densities of all samples exceeded 98%TD. The interface between individual layers after sintering is smooth and does not contain any extra porosity. In this

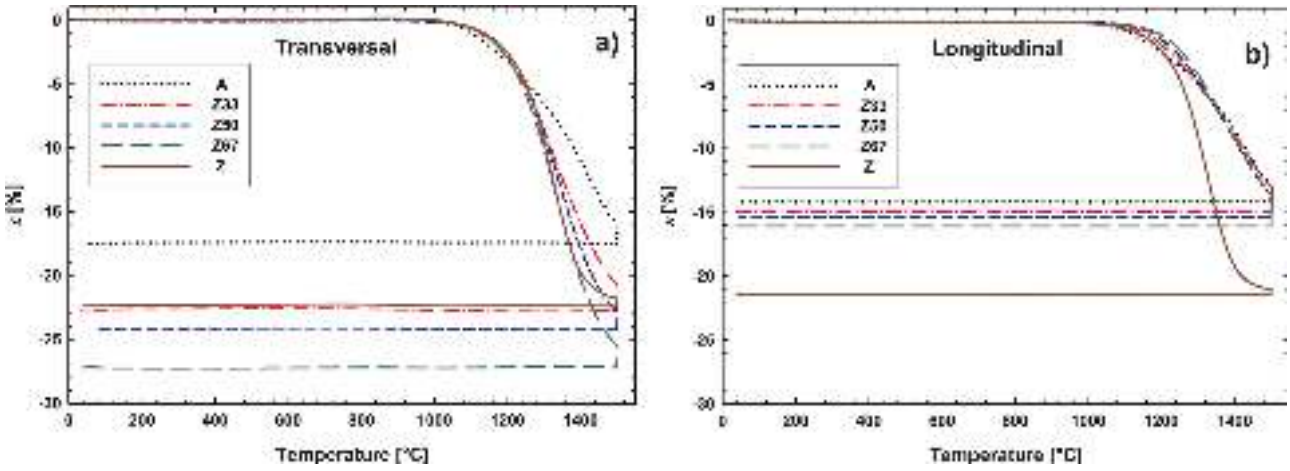

Fig. 2. Sintering shrinkage of all samples in the a) transversal and b) longitudinal direction.

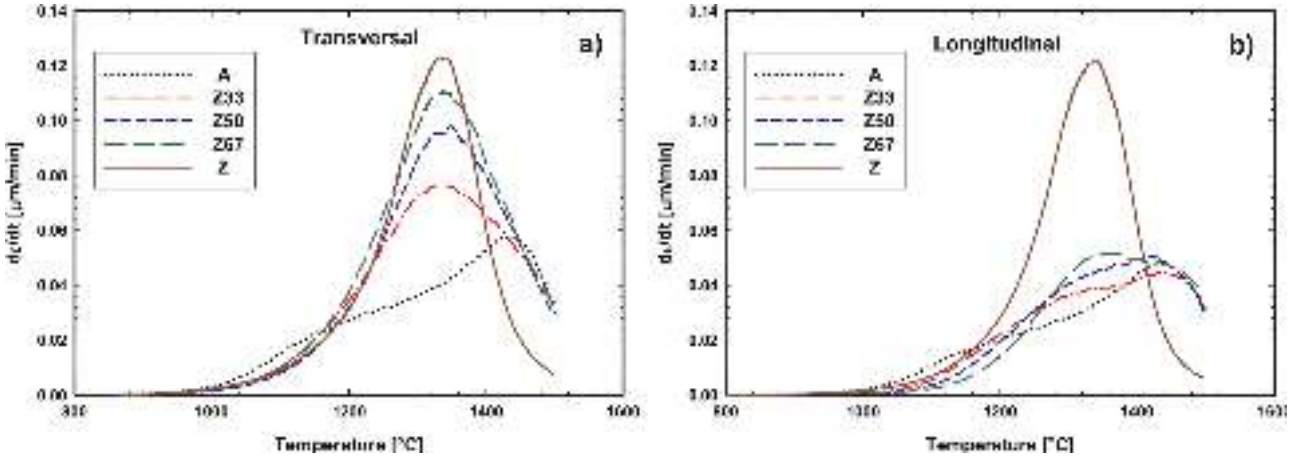

Fig. 3. Sintering shrinkage rate of all samples in the a) transversal and b) longitudinal direction.

regard, EPD was found as the more promising method in preparation of laminate composites than the commonly used methods of tape-casting [31,32], sequential slip casting [33], centrifugal casting [34], or screen printing [35].

Generally, ceramic laminate materials can be separated into two types. The first ones are laminates with weakly bonded layers. Typically, these laminates have fracture behaviour under loading known as delamination. The second types of laminates have interfaces between individual layers strongly bonded resulting in internal stresses. The crack path during loading is, therefore, influenced by tensile or compressive stresses developed during cooling from the sintering temperature. The interfaces between individual layers in presented laminates are flat and strongly bonded.

3.2. Dilatometric analysis of sintering shrinkage

The sintering shrinkage of all deposits, measured in transversal as well as longitudinal directions, is given in Fig. 2. It can be seen that sintering shrinkage of the alumina monolith is smaller than that of the zirconia (refer to Fig. 2a for transversal direction, resp. Fig. 2b for longitudinal). The reason is the lower green density of the zirconia green body (48%TD for zirconia, resp. 62%TD for alumina). The difference of green densities may be caused by particle size and shape, orientation of particles in the electrical field, capillary forces, etc. [36]. Fig. 2a, resp. b, and Table 2 also show different sintering shrinkage in the longitudinal and transversal directions of alumina (difference in the final shrinkage of 3.3%) as well as zirconia (difference in the final shrinkage of 1.0%) monoliths. The possible explanation of sintering shrinkage anisotropy of both monoliths can be preferential packing during the EPD [37]. This hypothesis is strengthened by the fact that shrinkage anisotropy is larger for alumina with oval (anisotropic) initial powder particles.

In the case of shrinkage in the transversal direction (see Fig. 2a), one could expect that laminates shrinkage in this direction will be the superposition of alumina and zirconia shrinkages and after sintering it will reach a value between 17.5% (final transversal shrinkage of alumina monolith) and 22.4% (final transversal shrinkage of zirconia monolith). In reality, the final sintering shrinkage of all three composites was higher: 22.7% for Z33, 24.2% for Z50, and even 27.2% for Z67 (refer to Table 2). To explain this apparent disproportion, we need to heed the sintering shrinkage in the longitudinal direction. As can be seen in Fig. 2b, in this direction the sintering shrinkage of all laminates is very similar to the shrinkage of the alumina monolith, therefore zirconia layers are forced to densify preferentially in the transversal direction [1,32]. This is supported by the observation of an increasing degree of shrinkage anisotropy with an increasing content of zirconia (see Table 2).

The shrinkage rate of both monoliths and their laminate composites is shown in Fig. 3. It is well known [38] that with decreasing particle size the sintering temperature decreases as well. In our case, the maximal shrinkage of zirconia (particle size 140 nm) occurred at ca 1340 °C, whilst that of alumina (particle size 470 nm) was at ca 1410 °C. This fact, together with the strong bond between alumina and zirconia layers, is probably responsible for the high

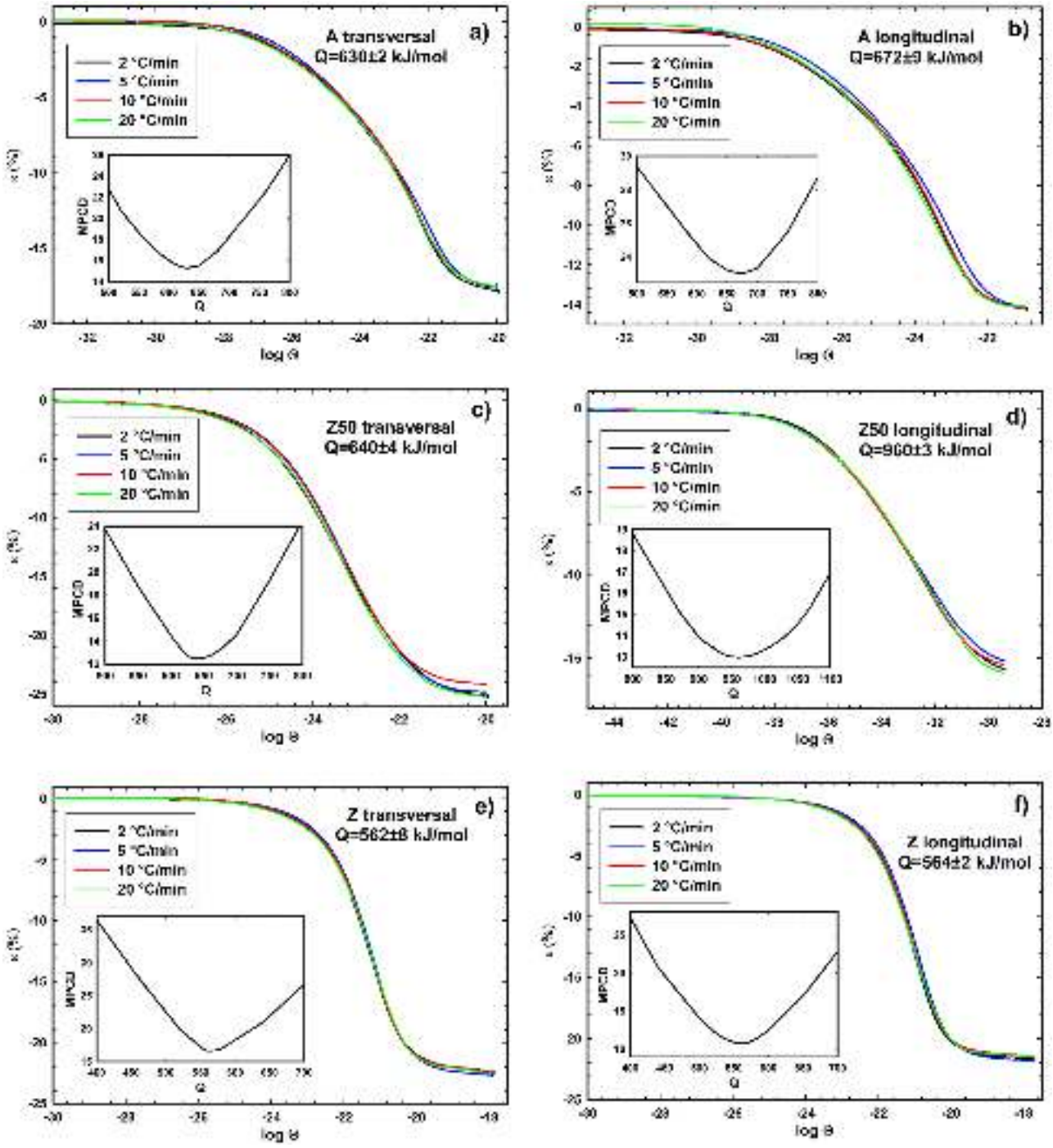

Fig. 4. Master Shrinkage Curves of samples: (a, b) A, (c, d) Z50, and (e, f) Z in the longitudinal and transversal directions.

degree of anisotropy of the laminates. Zirconia layers tend to shrink at temperatures of around 1300 °C, but in the longitudinal direction they are bound at inter-layers by alumina which is still rigid at this temperature. Therefore, zirconia shrinks particularly in the transversal direction. It can be seen in Fig. 3b that the maximal shrinkage rate of laminates in the longitudinal direction is shifted to temperatures of about 1400 °C, which is the temperature appropriate for the sintering of alumina. Therefore, the sintering of the composite in the longitudinal direction is controlled by the material with a higher sintering temperature. As a consequence, the sintering shrinkage of the zirconia layers is smaller in the longitudinal direction than without this constraint. The degree of the sintering anisotropy of the zirconia increased with its increasing volume concentration and it is necessary to take into account this effect when we design a laminate with precise thickness of individual layers.

3.3. Modified Master Sintering Curve – Master Shrinkage Curve

The model of MSC can be used for the calculation of activation energy of sintering, which allows a deeper view into the physical background of the sintering process. However, the results in the previous chapter showed that the sintering of ceramic laminates exhibits a significant degree of anisotropy, so the utilization of MSC in its original form is not possible. The following part shows the

way to modify the MSC model to make it suitable for describing anisotropic sintering.

Hansen and co-workers [39] formulated the model of sintering in the open and closed porosity stage which relates the linear shrinkage rate of a compact to grain boundary and volume diffusion coefficient, surface tension, and microstructure variables

$$-\frac{d\varepsilon}{dt} = \frac{\gamma\Omega}{kT}\left(\frac{\Gamma_v D_v}{G^3} + \frac{\Gamma_b \delta D_b}{G^4}\right), \tag{5}$$

where D_v resp. D_b are the coefficients of volume, resp. grain boundary diffusion, Γ_v, and Γ_b represent scaling parameters that relate different geometric features as the driving force of sintering and the mean diffusion distance to the grain size, and δ is the grain boundary thickness.

Assuming that

- the grain size evolution in the course of sintering is independent of thermal history and it is only a function of density; and
- one sintering mechanism dominates the whole sintering process,

we can rearrange Eqs. (5) to (6)

$$\frac{-k}{\gamma\Omega D_0}\int_0^{\varepsilon_f}\frac{(G(\varepsilon))^n}{\Gamma(\varepsilon)}d\varepsilon = \Theta = \int_0^t \frac{1}{T}\exp\left(-\frac{Q}{RT}\right)dt, \tag{6}$$

which relates microstructural parameters with thermal history of the sample.

The modified Master Sintering Curve (Master Shrinkage Curve) is now defined as a relationship between ε and the right side of Eq. (6). If the concept of Master Shrinkage Curve is correct, there must exist one activation energy Q for which all functions of $\varepsilon = f(\Theta)$ (calculated for all used heating profiles) converge onto a single (master) curve. The criterion of Mean Perpendicular Curve Distance (MPCD) [20] can be used to find the best overlap of individual curves. Both monoliths and one laminate (Z50) were sintered with heating rates of 2, 5, 10, and 20 °C in transversal as well as in longitudinal directions and the constructed Master Shrinkage Curves are shown in Fig. 4.

Fig. 4a–f show a good overlap of individual curves and the MPCD criterion exhibits a single sharp minimum. The values of activation energies established from the Master Shrinkage Curve model can be seen in Fig. 5.

The sintering activation energy established from the MSC concept is commonly interpreted as apparent activation energy for the mechanism that controls sintering [40]. The published values of sintering activation energies vary through the literature very strongly (Al_2O_3: 342–1064 kJ/mol [41–43]; t-ZrO_2 310–1220 kJ/mol [27,44]), which is probably caused by the different processing methods, level of impurities, temperature range, and also by the used models. For this given experimental procedure, the

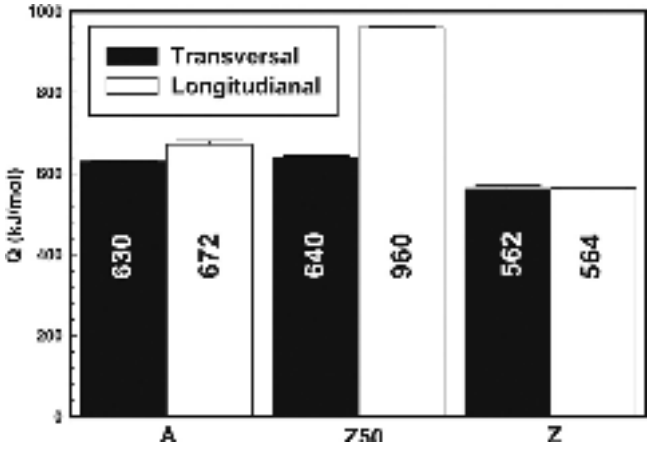

Fig. 5. Activation sintering energies of alumina monolith, Z50 laminate, and zirconia monolith.

activation energies of sintering of alumina and zirconia monoliths are in the range presented by other authors and they do not exhibit either no (for zirconia) or minimal (for alumina) difference between the transversal and the longitudinal direction.

Despite the final longitudinal shrinkage of the Z50 composite being similar to alumina, the sintering of Z50 laminate is characterized by a significant increase of the sintering activation energy in the longitudinal direction. The increase of activation energy of sintering shrinkage was expected due to a constrained sintering [45] which influences the shape of the shrinkage curves (see Fig. 2b). In view of the dilatometric analysis of sintering shrinkage performed within this work, we believe that the increase of sintering activation energy of the composite can be caused by preferential sintering of zirconia in the transversal direction (see Fig. 6) which resulted in the deformation of the originally isotropic pores (see Fig. 7).

3.4. Crack propagation through the laminates with different layer thickness ratio

The crack propagation through laminates with a different alumina/zirconia thickness ratio (namely 2:1, 1:1, and 1:2) was studied by SEM and confocal laser microscopy. SEM microphotographs in the upper part of Fig. 8 show the side surface view of the fracture surface in the central part of the crack propagating from the notch after fracture toughness experiments using the SEVNB technique. The 3D reconstructions of fracture surfaces together with their height profiles showing variations in the crack deflection according to the layer are given in the middle, resp. bottom part of Fig. 8. Note that the darker phase is alumina and the brighter one is a zirconia layer, and that crack propagation direction is along the X-axis. It clearly follows from Fig. 8 that the declination of the crack propagation from its original direction is strongly influenced by the

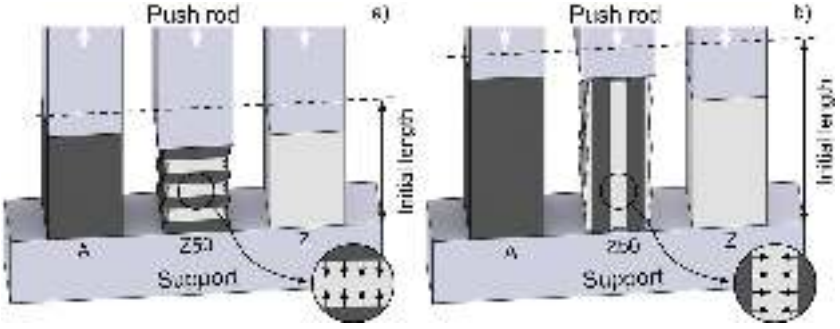

Fig. 6. Scheme of sintering shrinkage in alumina/zirconia laminates in the a) transversal and b) longitudinal direction. Arrows indicate preferential shrinkage.

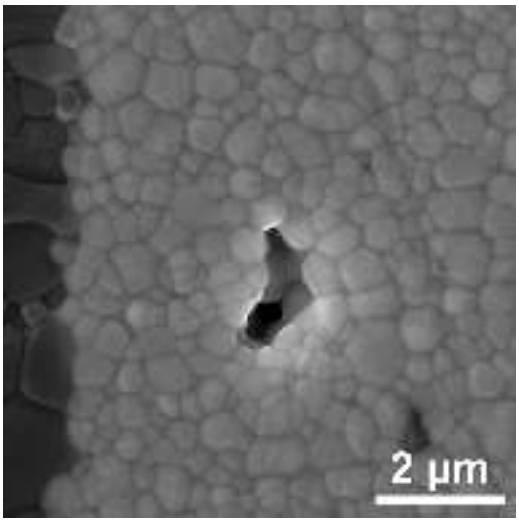

Fig. 7. SEM evidence of elongated pores in zirconia layer.

laminate design (see declination angles in Fig. 8). The highest crack declination was reached in sample Z67 (Fig. 8c), where the crack was deflected by about 550 μm at a distance of 250 μm, whilst in Z33 laminate (Fig. 8a) it was only 30 μm at the same distance. The fracture behaviour of the laminates prepared by the optimised sintering of the EPD green bodies that have strong bonds is influenced by the developed internal stresses within the layers during cooling from the sintering temperature. The stresses retained in the material as a consequence of constrained sintering are negligible compared to previous ones (due to a difference of two orders of magnitude) [11]. The values of internal stresses calculated according to Eq. (1) and given material constants [13,46] are listed in Table 3.

Due to the higher thermal expansion of zirconia [46], tensile stress is present in zirconia layers. It led to the crack propagation inclining to the loading direction (i.e. along the X-axis as is shown in Fig. 8). This behaviour is typical and it can be attributed to the tensile stresses being similar and relatively low for all laminates under investigation. The main difference in the fracture behaviour of laminates under investigation was observed in the alumina layers with substantially different compressive stresses. The deviation of the crack from the loading axis propagating through the alumina layer (see Fig. 8) is the result of a combination of three effects: the difference in the elastic modulus, the tilt of the laminae plane to the loading axis, and the influence of internal compressive stresses. The effect of the elastic modulus can be expected to be the same for all laminates, not being affected by the layer thickness. The effect of

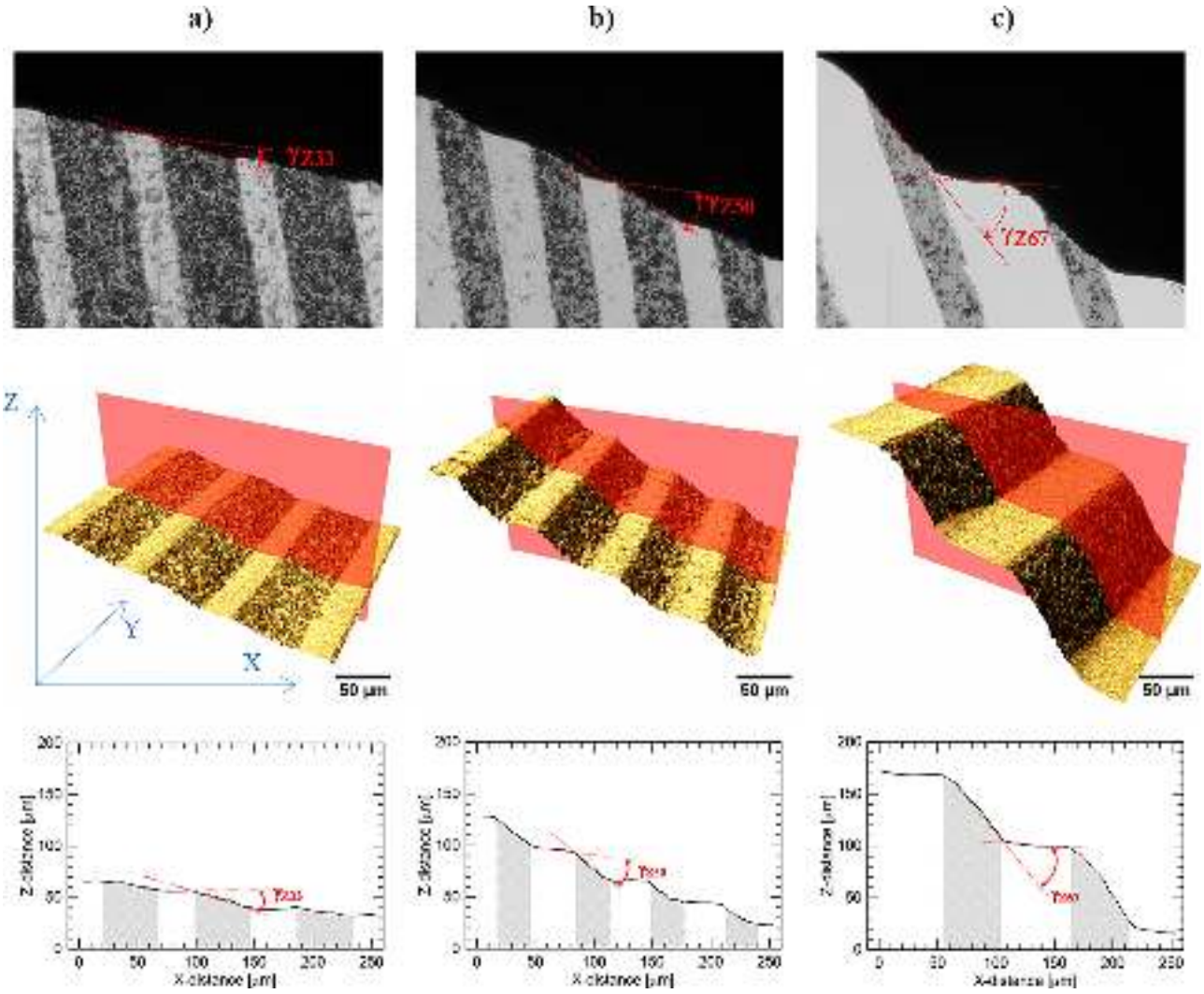

Fig. 8. Fracture surfaces side view (upper line of figures), their confocal microscope image (middle line of figures) and quantitative analysis (bottom line of figures) describing declination angles at alumina/zirconia interfaces for a) Z33, b) Z50), and c) Z67 laminates.

Table 3
Internal stresses developed during cooling down from sintering temperature (A – alumina, Z – zirconia, sign in stress means: minus = compressive; plus = tensile).

Monolith	α [10^{-6} K^{-1}]	E [GPa]	Poisson ratio [–]	Laminate	Nominal internal stress [MPa]	
					layer A	layer Z
A	8.915	380	0.26	Z33	−279	447
Z	10.275	210	0.31	Z50	−440	352
				Z67	−617	247

the laminate tilt predetermining the entering angle of the starting crack from the notch plays an important role, but it is independent of the volume ratio, too. Contrary to that, the effect of the internal compressive stresses affects the declination angle significantly as demonstrated in Fig. 8 and it is dependent only on the materials volume ratio. According to expectation and observation, the higher the compressive stresses are the higher the deviation of the crack from the loading direction.

4. Conclusions

Alumina and zirconia monoliths, as well as their lamellar composites with three different thickness ratios, were prepared by electrophoretic deposition. The detailed dilatometric study of their sintering shrinkage revealed that sintering shrinkage of laminates was constrained in the longitudinal direction (parallel with layers interfaces) by alumina which was densified at higher temperatures than zirconia. As a consequence, sintering shrinkage in the transversal direction (perpendicular to layers) was accelerated by the preferential shrinkage of zirconia in this direction. The model of Master Sintering Curve was modified in order to describe the sintering of anisotropic systems. The enhanced sintering activation energy in the longitudinal direction confirmed the constrained sintering of laminates. The detailed fractographic analysis of crack propagation in laminates with well-defined layer thickness ratios revealed the importance of individual parameters on its declination.

Acknowledgements

The authors acknowledge the support of the Grant agency of the Czech Republic under grant no. 15-06390S. The research has also been financially supported by the Ministry of Education, Youth and Sports of the Czech Republic under the project CEITEC 2020 (LQ1601).

References

[1] H. Hadraba, D. Drdlik, Z. Chlup, K. Maca, I. Dlouhy, et al., Layered ceramic composites via control of electrophoretic deposition kinetics, J. Eur. Ceram. Soc. 33 (2013) 2305–2312.
[2] L. Vandeperre, O. VanDerBiest, W.J. Clegg, Silicon carbide laminates with carbon interlayers by electrophoretic deposition, Key Eng. Mater. 127–131 (1997) 567–573.
[3] D. Drdlik, E. Bartonickova, H. Hadraba, J. Cihlar, Influence of anionic stabilization of alumina particles in 2-propanol medium on the electrophoretic deposition and mechanical properties of deposits, J. Eur. Ceram. Soc. 34 (2014) 3365–3371.
[4] E. Askari, M. Mehrali, I.H.S.C. Metselaar, N.A. Kadri, M.M. Rahman, Fabrication and mechanical properties of Al_2O_3/SiC/ZrO_2 functionally graded material by electrophoretic deposition, J. Mech. Behav. Biomed. 12 (2012) 144–150.
[5] P. Hvizdos, D. Jonsson, M. Anglada, G. Anne, O. Van Der Biest, Mechanical properties and thermal shock behaviour of an alumina/zirconia functionally graded material prepared by electrophoretic deposition, J. Eur. Ceram. Soc. 27 (2007) 1365–1371.
[6] M. Mehrali, H. Wakily, I.H.S.C. Metselaar, Residual stress and mechanical properties of Al_2O_3/ZrO_2 functionally graded material prepared by EPD from 2-butanone based suspension, Adv. Appl. Ceram. 110 (2011) 35–40.
[7] H. Moon, M.G. Pontin, F.F. Lange, Crack interactions in laminar ceramics that exhibit a threshold strength, J. Am. Ceram. Soc. 87 (2004) 1694–1700.
[8] W.A. Cutler, F.W. Zok, F.F. Lange, P.G. Charalambides, Delamination resistance of two hybrid ceramic-composite laminates, J. Am. Ceram. Soc. 80 (1997) 3029–3037.
[9] C. Hillman, Z.G. Suo, F.F. Lange, Cracking of laminates subjected to biaxial tensile stresses, J. Am. Ceram. Soc. 79 (1996) 2127–2133.
[10] Y. Zhao, L.R. Dharani, Theoretical-model for the analysis of a ceramic thin-film sintering on a non-sintering substrate, Thin Solid Films 245 (1994) 109–114.
[11] P.Z. Cai, D.J. Green, G.L. Messing, Constrained densification of alumina/zirconia hybrid laminates. 1. Experimental observations of processing defects, J. Am. Ceram. Soc. 80 (1997) 1929–1939.
[12] R.K. Bordia, R. Raj, Sintering behavior of ceramic films constrained by a rigid substrate, J. Am. Ceram. Soc. 68 (1985) 287–292.
[13] H. Hadraba, J. Klimes, K. Maca, Crack propagation in layered Al_2O_3/ZrO_2 composites prepared by electrophoretic deposition, J. Mater. Sci. 42 (2007) 6404–6411.
[14] K. Maca, H. Hadraba, J. Cihlar, Electrophoretic deposition of alumina and zirconia – I. Single-component systems, Ceram. Int. 30 (2004) 843–852.
[15] K. Maca, V. Pouchly, A.R. Boccaccini, Sintering densification curve – a practical approach for its construction from dilatometric shrinkage data, Sci Sinter. 40 (2008) 117–122.
[16] H.H. Su, D.L. Johnson, Master sintering curve: a practical approach to sintering, J. Am. Ceram. Soc. 79 (1996) 3211–3217.
[17] V. Pouchly, K. Maca, Master sintering curve – a practical approach to its construction, Sci. Sinter. 42 (2010) 25–32.
[18] D.C. Blaine, S.J. Park, R.M. German, Linearization of master sintering curve, J. Am. Ceram. Soc. 92 (2009) 1403–1409.
[19] K. An, M.K. Han, Microstructural evolution based on the pressure-assisted master sintering surface, Mater. Sci. Eng. A—Struct. 391 (2005) 66–70.
[20] V. Pouchly, K. Maca, Y. Xiong, J.Z. Shen, Master sintering surface –A practical approach to its construction and utilization for spark plasma sintering prediction, Sci. Sinter. 44 (2012) 169–175.
[21] R.K. Enneti, M.G. Bothara, S.J. Park, S.V. Atre, Development of master sintering curve for field-assisted sintering of HfB2-20SiC, Ceram. Int. 38 (2012) 4369–4372.
[22] K.J. An, M.K. Han, H.J. Kim, The pressure-Assisted master sintering surface of metallic powder mixture, Mater. Trans. 51 (2010) 822–825.
[23] F. Raether, P.S. Horn, Investigation of sintering mechanisms of alumina using kinetic field and master sintering diagrams, J. Eur. Ceram. Soc. 29 (2009) 2225–2234.
[24] C.B. DiAntonio, K.G. Ewsuk, D. Bencoe, Extension of master sintering curve theory to organic decomposition, J. Am. Ceram. Soc. 88 (2005) 2722–2728.
[25] S.Y. Wang, M.H. Teng, Why a master sintering curve model can be applied to the sintering of nano-sized particles? J. Alloy Compd. 504 (2010) S336–S339.
[26] X.C. Song, J. Lu, T.S. Zhang, J. Ma, Two-stage master sintering curve approach to sintering kinetics of undoped and Al(2)O(3)-doped 8 mol% yttria-stabilized cubic zirconia, J. Am. Ceram. Soc. 94 (2011) 1053–1059.
[27] V. Pouchly, K. Maca, Z. Shen, Two-stage master sintering curve applied to two-step sintering of oxide ceramics, J. Eur. Ceram. Soc. 33 (2013) 2275–2283.
[28] R. Bjork, H.L. Frandsen, N. Pryds, Modeling the microstructural evolution during constrained sintering, J. Am. Ceram. Soc. 98 (2015) 3490–3495.
[29] L.S. Arias-Maya, Free and constrained sintering of 3-mol% yttria stabilised zirconia, Dyna-Colombia 81 (2014) 158–167.
[30] H. Hadraba, D. Drdlik, Z. Chlup, K. Maca, I. Dlouhy, et al., Laminated alumina/zirconia ceramic composites prepared by electrophoretic deposition, J. Eur. Ceram. Soc. 32 (2012) 2053–2056.
[31] J.B. Davis, A. Kristoffersson, E. Carlstrom, W.J. Clegg, Fabrication and crack deflection in ceramic laminates with porous interlayers, J. Am. Ceram. Soc. 83 (2000) 2369–2374.
[32] A.J. Sanchez-Herencia, J. Gurauskis, C. Baudin, Processing of Al_2O_3/Y-TZP laminates from water-based cast tapes, Compos. B—Eng. 37 (2006) 499–508.
[33] J. Requena, R. Moreno, J.S. Moya, Alumina and alumina zirconia multilayer composites obtained by slip casting, J. Am. Ceram. Soc. 72 (1989) 1511–1513.
[34] E. Lucchini, O. Sbaizero, Alumina/zirconia multilayer composites obtained by centrifugal consolidation, J. Eur. Ceram. Soc. 15 (1995) 975–981.
[35] X. Wang, A. Atkinson, Microstructure evolution in thin zirconia films: experimental observation and modelling, Acta Mater. 59 (2011) 2514–2525.
[36] R. Chaim, M. Levin, A. Shlayer, C. Estournes, Sintering and densification of nanocrystalline ceramic oxide powders: a review 2, Adv. Appl. Ceram. 107 (2008) 159–169.
[37] S.K. Yang, W.P. Cai, G.Q. Liu, H.B. Zeng, From nanoparticles to nanoplates: preferential oriented connection of Ag colloids during electrophoretic deposition, J. Phys. Chem. C 113 (2009) 7692–7696.
[38] M.J. Mayo, Processing of nanocrystalline ceramics from ultrafine particles, Int. Mater. Rev. 41 (1996) 85–115.
[39] J.D. Hansen, R.P. Rusin, M.H. Teng, D.L. Johnson, Combined-stage sintering model, J. Am. Ceram. Soc. 75 (1992) 1129–1135.

[40] G. Bernard-Granger, A. Addad, G. Fantozzi, G. Bonnefont, C. Guizard, et al., Spark plasma sintering of a commercially available granulated zirconia powder: comparison with hot-pressing, Acta Mater. 58 (2010) 3390–3399.
[41] Z.M. He, J. Ma, Constitutive modeling of alumina sintering: grain-size effect on dominant densification mechanism, Comput. Mater. Sci. 32 (2005) 196–202.
[42] W.Q. Shao, S.O. Chen, D. Li, H.S. Cao, Y.C. Zhang, et al., Prediction of densification and microstructure evolution for alpha-Al(2)O(3) during pressureless sintering at low heating rates based on the master sintering curve theory, Sci. Sinter. 40 (2008) 251–261.
[43] K. Maca, V. Pouchly, K. Bodisova, P. Svancarek, D. Galusek, Densification of fine-grained alumina ceramics doped by magnesia, yttria and zirconia evaluated by two different sintering models, J. Eur. Ceram. Soc. 34 (2014) 4363–4372.
[44] G. Bernard-Granger, C. Guizard, Apparent activation energy for the densification of a commercially available granulated zirconia powder, J. Am. Ceram. Soc. 90 (2007) 1246–1250.
[45] F.F. Lange, M.M. Hirlinger, Hindrance of grain-growth in Al_2O_3 by ZrO_2 inclusions, J. Am. Ceram. Soc. 67 (1984) 164–168.
[46] M.G. Pontin, M.P. Rao, A.J. Sanchez-Herencia, F.F. Lange, Laminar ceramics utilizing the zirconia tetragonal-to-monoclinic phase transformation to obtain a threshold strength, J. Am. Ceram. Soc. 85 (2002) 3041–3048.

Journal of the European Ceramic Society 39 (2019) 1297–1303

Contents lists available at ScienceDirect

Journal of the European Ceramic Society

journal homepage: www.elsevier.com/locate/jeurceramsoc

Original Article

Improved microstructure of alumina ceramics prepared from DBD plasma activated powders

Václav Pouchlý[a,b,*], Jozef Ráheľ[c], Tomáš Spusta[a,b], Martina Ilčíková[c], David Pavliňák[c], Tomáš Morávek[c], Karel Maca[a,b]

[a] CEITEC BUT, Brno University of Technology, Purkynova 123, 612 00 Brno, Czech Republic
[b] Department of Materials Science and Engineering, Brno University of Technology, Technicka 2, 616 69 Brno, Czech Republic
[c] Department of Physical Electronics - CEPLANT, Masaryk University, Kotlarska 2, 611 37 Brno, Czech Republic

ARTICLE INFO

Keywords:
Alumina
Slip casting
Sintering
Grain size
DBD plasma treatment

ABSTRACT

Submicron Al_2O_3 powders were activated by Diffuse Coplanar Surface Barrier Discharge (DCSBD) plasma. The influence of the plasma treatment on the powder properties and their impact on the microstructure of dry and wet shaped ceramics were investigated. Raman and FTIR analyses of treated powders showed a substantial increase of the powder's surface hydroxylation, surface cleaning, and the presence of adsorbed NO_x originating from the DCSBD. Sintering of the dry shaped plasma treated powders did not influence sintering behavior. On the other hand, the plasma treated powder was able to form stable water suspension without any chemical stabilization aid. Slip cast samples exhibited finer pore size distribution, a higher sinterability, and a finer final microstructure. The grain size of slip casted plasma treated powder was reduced by a factor of 1.7, which facilitated a grain size of 0.68 μm at the relative density of 99.54% t.d. obtained by pressure-less sintering.

1. Introduction

The final properties of ceramic materials are significantly affected by their microstructure. In the case of processing advanced ceramic materials, the refinement of its final microstructure is often approached by employing the particles of submicron or even nanometer sizes [1]. However, there are two main sets of problems to deal with when the fine particles of enormous surface area are employed: (1) their tendency to aggregate/agglomerate [2] and (2) the problem of grain growth control [3]. Only when these two problems are successfully addressed, the materials with excellent mechanical [4] or even optical [5] properties can be fabricated.

During the ceramics processing, even a small change of the powders surface energy can cause a considerable improvement of final properties. The processing steps which are most affected by the change of surface energy are powder synthesis, shaping (especially wet methods), and sintering. The surface energy of powders can be modified by conventional methods like high-energy milling, coating etc. [6]. However, modern technologies of surface modification, such as plasma treatment, are also viable. Plasma treatment technology is widely used for surface cleaning [7], the separation of particles [8], or the coating of particles' surface [9]. One of the first attempts to modify the surface energy by plasma treatment on ceramic materials was made by Ishigaki et al. in 1995 [10]. They modified the surface of the titanium carbide powder with a high-temperature plasma torch. Partial spheridization of TiC particles was accompanied by the formation of chemically active carbon site vacancies. This led to the decrease of sintering temperatures by approximately 100 °C A large body of literature is available on low-pressure, low-temperature (cold) plasma sources, which do not affect the bulk properties of powders [9,11,12]. The most common objective was to improve powders water wettability. On the radio frequency (RF) (13.56 MHz) low-pressure air plasma provided a significant improvement of kaolinite powder water wettability [11]. The stability of TiO_2 particles in water was improved by plasma polymerization of acrylic acid onto the particles surface, using a similar type of RF capacitive coupled reactor [12]. Ultrathin films of pyrrole were deposited on the surfaces of alumina nanoparticles using an inductively coupled RF (13.56 MHz) plasma in [9].

In the last few decades, new low-temperature (cold) plasma sources operated at atmospheric pressure became available. These types of plasma sources overcame the time and cost consuming step of evacuation, thus enabling faster commercialization by reducing the investment and processing costs [13]. Such new plasma sources have already been used for improvement of surface wettability or adhesion

* Corresponding author at: Central European Institute of Technology, Brno University of Technology, Purkynova 123, 612 00 Brno, Czech Republic.
E-mail address: vaclav.pouchly@ceitec.vutbr.cz (V. Pouchlý).

https://doi.org/10.1016/j.jeurceramsoc.2018.11.022
Received 13 July 2018; Received in revised form 6 November 2018; Accepted 11 November 2018
Available online 12 November 2018
0955-2219/

properties of various materials [14] including powders [15,16]. However, the references about their direct use in ceramic technology are rare. The authors in [17] treated Al_2O_3 powder by a coplanar type of dielectric barrier discharge (DBD) operated in ambient air. They found an improved suspension stability of water-based suspension of Al_2O_3 colloidal dispersion and also a finer microstructure of dry shaped samples for treated powder. The same type of plasma treatment had a significant positive effect on the dynamics of electrophoretic deposition (EPD) of submicron alumina powder dispersed in the non-aqueous organic solvent of 2-propanol, accompanied by the slight improvement of the density and mean grain size of the final layered composite [18].

In the presented paper, we are going to analyze the influence of coplanar DBD plasma treatment of alumina powder in its final microstructure. Its influence on both dry and wet shaping ceramics processing methods is going to be investigated, to see if changes in the surface properties of the plasma treatment have an influence on the processing method in these distinct types of shaping methods.

2. Materials and methods

High purity 99.99% commercial alumina powder Taimicron TM-DAR (Taimei Chemicals Co., Ltd., Tokyo, Japan, specific surface area 13.7 $m^2 g^{-1}$, which in case of rounded particles corresponds to the particle size of about 110 nm [19]) was used in all experiments. The 0.25 g doses of powder were sifted through a sieve to create a thin layer on the surface of the discharge ceramics of Diffuse Coplanar Surface Barrier Discharge (DCSBD) plasma generator (Fig. 1). It was activated for a duration of 45 s and removed for further ceramic processing. The thin powder layer had to be covered with a protective alumina plate to prevent any material loss due to the presence of plasma ionic wind [20]. The process was repeated about 160 times until a sufficient amount of treated powder over 40 g was obtained.

The DCSBD electrode system consisted of a pair of coplanar comb-like energizing electrodes with linear strips (teeth) of 1.5 mm width and 1 mm lateral separation, screen-printed on the transformer oil insulated face of 0.635 mm thick 96% Al_2O_3 dielectric plate. The active area of generated plasma was about 8 × 20 cm^2. The system was powered by a 14 kHz sinusoidal high voltage of up to 20 kV peak-to-peak amplitude and input power of 400 W, supplied by an in-house built power generator. Discharge was operated in static (no flow) atmospheric pressure air of absolute humidity within the range of 3–8 gH_2O/m^3. The maximum temperature of the DCSBD dielectric panel was less than 70 °C.

2.1. Shaping

Overview of the shaping methods used and the abbreviation of samples sets are given in Table 1. For the Cold Isostatic Pressing, the alumina powder was poured into a latex cylindrical die and pressed in an isostatic press (Autoclave Engineering Inc., USA) at a pressure of 300 MPa with a dwell time of 5 min. This pressing resulted in a disc of about 30 mm in diameter with a thickness of about 5 mm for treated as well as untreated powders. Suspensions for the slip casting were water based with a powder content of 37.5 vol% to ensure proper ultrasound homogenization. Two different suspensions were prepared. The suspension abbreviated as 'P-SC' was prepared by the mixing of water and about 40 g of plasma activated powder; the suspension abbreviated as 'R-SC' was prepared as received powder with water and 2.2 wt.% of ammonium polymethylmetaclyrate (Darvan C–N, Vanderbilt Minerals, USA). Both suspensions were homogenized using a 160 W ultrasonic probe (Sonopuls HD2200, Bandelin, Germany) for 2 min. Afterwards, about 15 ml of suspensions were slip cast into a plastic mold of 25 mm diameter and 10 mm height with the bottom made of gypsum, to provide proper water drying. The cast suspensions were dried in ambient air for several days. All green bodies (both wet and dry shaped) were cut into rectangular prism shaped samples with the weight of approx. 2 g.

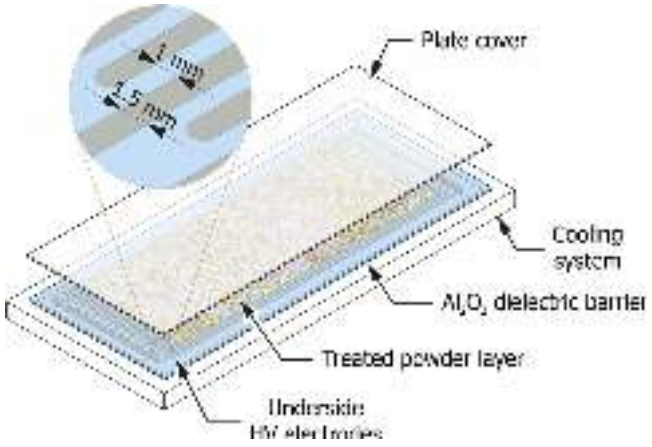

Fig. 1. The schematics of the DCSBD setup for the treatment of alumina powders.

2.2. Sintering

The samples were first sintered in a high temperature dilatometer (L75, Linseis, Germany) up to 1500 °C to estimate the appropriate temperature of the sintering and to compare the sintering behavior of different green bodies. The sintering shrinkages were recalculated to the densification profiles. Details of such recalculation are described elsewhere [21]. The main part of the sintering experiments were carried out in a superkanthal furnace (K 1700/1, Heraeus, Germany) in air atmosphere. Sintering processes were executed incrementally by heating 10 °C/min up to a temperature of 800 °C and heated at a rate of 5 °C/min to different, final temperatures. The cooling rate was set as 25 °C/min.

2.3. Analytical methods

Raman spectra of powders were recorded by LabRAM HR (Horiba Jobin Yvon, France). Spectra were acquired in a continuous scanning mode under a laser excitation wavelength of 532 nm in the range of 100 cm^{-1} to 3000 cm^{-1} with spectral resolution less than 2 cm^{-1}. The laser beam was focused by a 50× objective lens resulting in a spot size of approximately 1 μm in diameter. The acquisition time and the number of circulations were 60 s and 4 times, respectively.

FTIR-DRIFT (diffuse reflectance IR spectroscopy) spectra of powders were measured by FTIR spectrometer Bruker Vertex 80v with a Praying Mantis Diffuse Reflection Accessory (Harris Scientific). Spectra in the range of 4000–400 cm^{-1} were acquired at reduced pressure (2.51 hPa), with the accumulation of 500 scans.

Rheological behavior of the prepared suspensions was measured in the steady shear mode using a rotational rheometer (Hake Mars II, Thermo Scientific, Germany) equipped with a double gap cylinder sensor system. The pore size distribution of green bodies was evaluated by mercury intrusion porosimetry (Pascal 440, Porotec, Germany). The final relative densities were measured by the Archimedes principle (EN 623-2) with distilled water using 3.99 $g.cm^{-3}$ as the theoretical density of alumina. The cross sections of sintered samples were grounded and polished by the standard ceramographics methods and thermally etched. The microstructure of samples was evaluated by scanning electron microscopy (Philips XL30, Netherlands). The grain size was estimated by the linear intercept method (EN-ISO 13 383-1) using a correction factor of 1.56 [22].

Table 1
The list of samples and shaping methods.

Abbreviation	Plasma activation	Homogenization, stabilization	Shaping method
P-CIP	Yes	–	Cold Isostatic Press (300 MPa)
R-CIP	No	–	Cold Isostatic Press (300 MPa)
P-SC	Yes	2 min ultrasound	Slip casting
R-SC	No	2 min ultrasound, Dispersant	Slip casting

3. Results

3.1. Powder surface characterization

Four sets of powder materials were analyzed by DRIFT and Raman IR spectroscopies: as received samples (R), plasma treated samples (P), plasma treated samples which were heated in air up to the temperature of 500 °C for 1 h after the plasma treatment (PTD), and reference samples which were also heated to 500 °C for 1 h (RTD). The motivation for the heat treatment was to resolve the character of adsorbed species, as well as to simulate the state of plasma activated powder surface during elevated temperatures while sintering.

Fig. 2 displays the Raman spectra. Characteristic peaks of Al_2O_3 are situated in the low energy part of the spectra (379, 416, 483, 574, 642, 746 cm^{-1}). Plasma treatment induced a strong peak at 1046 cm^{-1} which was attributed to the δ OH deformation modes [23]. This indicates an enhanced hydroxylation of alumina surface due to the plasma treatment. No other peak has been significantly affected. The heat treatment of PTD samples resulted in complete removal of the 1046 cm^{-1} peak, which is consistent with the expected surface dehydroxylation at elevated temperatures [24].

In line with the Raman measurements, the broad intense FTIR peak at 3200 - 3700 cm^{-1} (see Fig. 3) confirmed a substantial increase of hydroxyl groups due to the plasma treatment [25,26]. Reference (R) spectra also contained a well pronounced peak at 1595 cm^{-1} which was assigned to the deformation vibration of adsorbed free water molecules [27]. Plasma treatment (P) as well as heat treatments (both RTD and PTD) facilitated a removal of this particular peak. In addition to the increased surface hydroxylation, the P samples exhibited a notable peak at 1310 cm^{-1} and less intense peaks with maxima at 1527 cm^{-1} and 1618 cm^{-1}. These peaks were attributed to the adsorbed NO_x molecules [28,29], which are generated by the air DCSBD in an ample amount [30]. This assignment is based also on results from our recent thermogravimetric/mass spectroscopy analysis [14], which identified increased thermal desorption at 300–400 °C $m/z = 30$ and 46 from plasma activated alumina powders, indicating the presence of NO_2. Moreover, the 500 °C heated PTD samples exhibited neither of these peaks, which further supports the thermal desorption hypothesis.

Sample R shows some minor peaks at 2964, 2930, 2850 cm^{-1}.

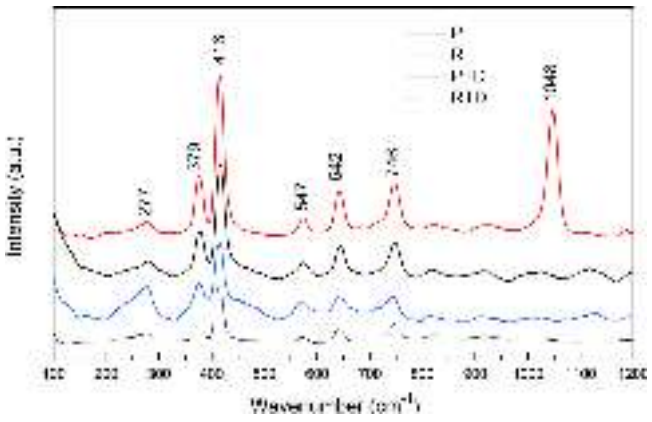

Fig. 2. Raman spectra of alumina powders with various treatment history.

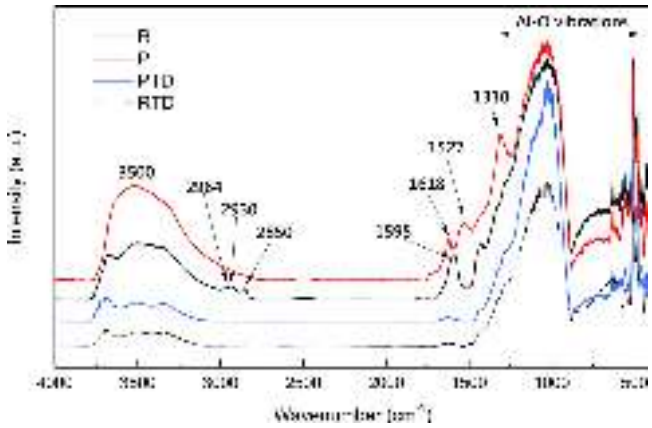

Fig. 3. FTIR/DRIFT infrared spectra of alumina powders with various treatment history.

These were attributed to hydrocarbon contamination, being identified as asymmetric CH_3, asymmetric CH_2, and symmetric CH_2 stretching respectively [27]. Their absence in the P spectrum indicates a plasma mediated surface cleaning. Finally, the bands in the region of 400-1200 cm^{-1} are characteristic for Al_2O_3 and correspond to the Al-O vibrations [31].

3.2. Shaping and sintering

The rheological behavior of P-SC and R-SC suspensions is shown in Fig. 4. The dependence of shear stress on shear rate showed shear thinning, which is typical for slightly agglomerated systems [2]. The almost missing hysteresis for P-SC suspension can be related to good suspension stability [2,32]. Fig. 4b shows that P-SC suspension is less viscous than R-SC suspension for all observed shear rates which can suggest the better dispersion of P-SC suspension (e.g. lower inter-particle forces) [33].

The pore size distribution of green bodies prepared by dry and wet shaping is shown in Fig. 5.

All samples exhibited unimodal narrow pore size distribution, with the most frequent pore size of 26, 26, 17, 22 nm for P-CIP, R-CIP, P-SC, and R-SC respectively. The maximum pore size of green bodies was 29, 29, 22, 28 nm for P-CIP, R-CIP, P-SC, and R-SC, respectively. It is clear that the powder treatment has no significant effect on dry shaped green body microstructure due to an obtaining of the same pore size distribution. However, it plays a crucial role during the wet shaping where the P-SC, as opposed to the R-SC, sample exhibits a considerable decrease of the most frequent pore size as well as of maximum pore size.

The sintering behavior for all sample sets is shown in Fig. 6. For dry shaping (Fig. 6a), the dilatometry curves of both types of powders are overlapping within the whole temperature range, with maximum density reached at 1420 °C. For the wet shaping (Fig. 6b), the sample prepared from activated powder exhibited higher relative density of green body (~64% t.d.) than the sample prepared by the same procedure from the non-activated powder (~58% t.d.). The sintering of both samples started around the same temperature of 1050 °C. Both samples also exhibited a comparable densification rate and the P-SC sample finished its sintering at 1400 °C, while the R-SC sample finished its

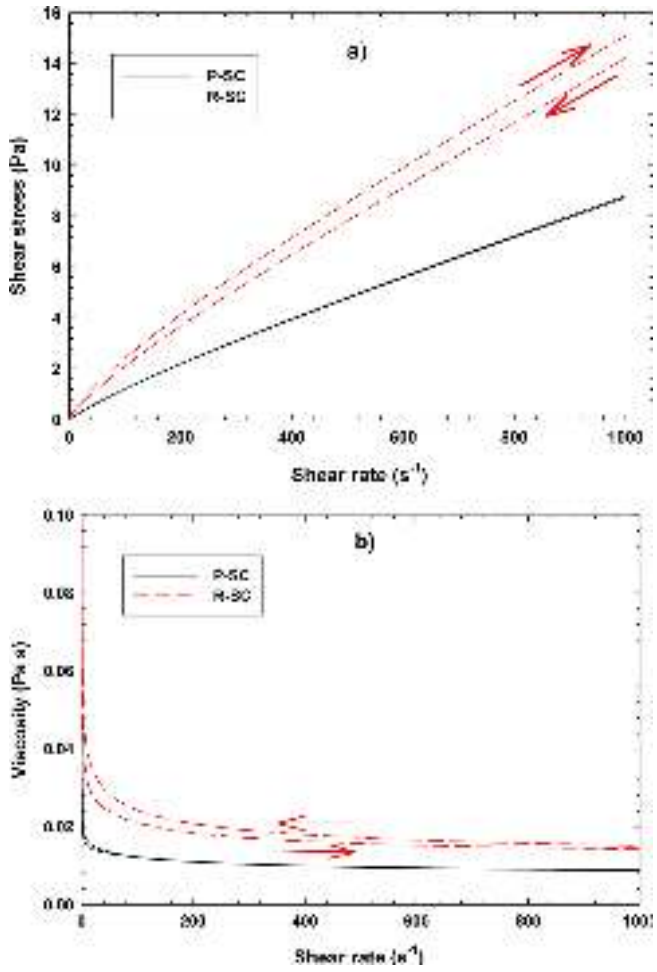

Fig. 4. Rheological behaviour: (a) dependence of shear stress on shear rate; (b) dependence of viscosity on shear rate.

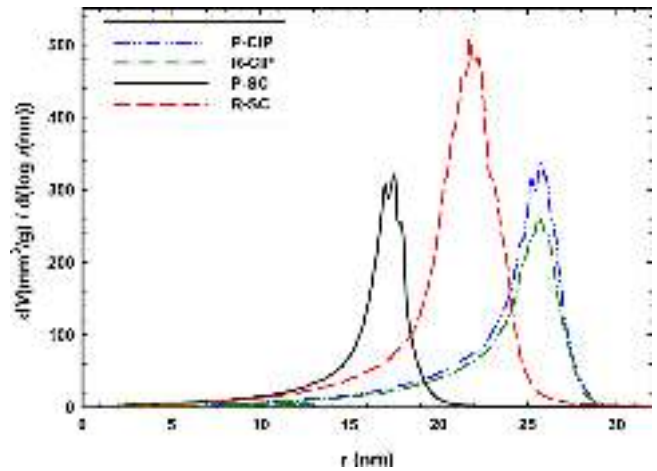

Fig. 5. Pore size distribution of green bodies.

sintering at 1420 °C.

3.3. Microstructure

Table 2 presents relative densities and grain sizes reached for samples prepared by the respective methods. The sintering trajectories for dry and wet shaping are shown in Fig. 7a and b, respectively. For the dry shaping process, the plasma treated sample reached at the density

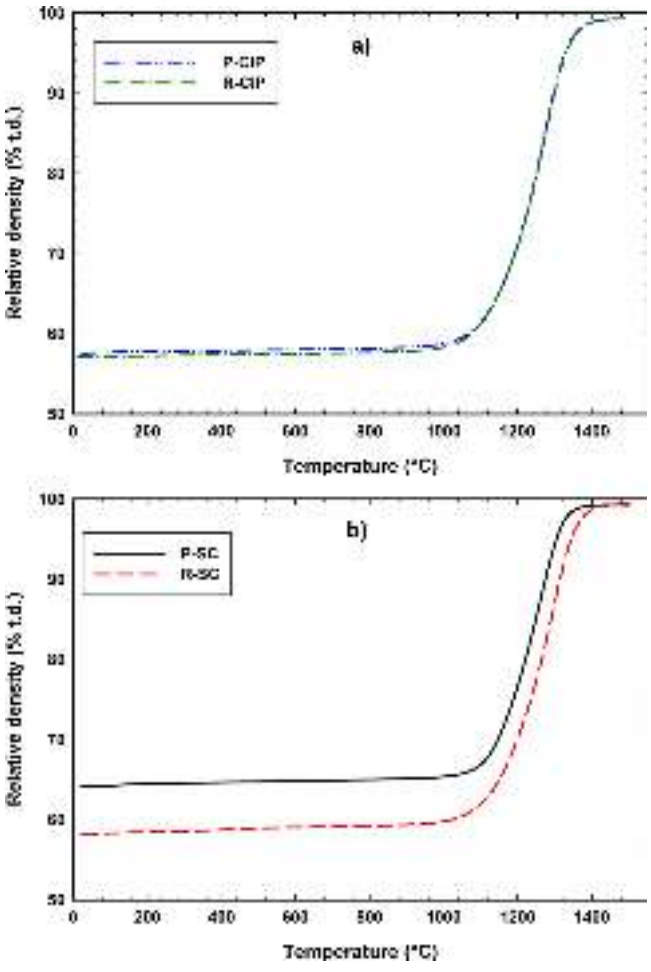

Fig. 6. Densification curves of the (a) dry shaped and (b) wet shaped samples.

Table 2
Comparison of heating schedules, relative densities and grain sizes.

Method	Sintering (°C/min)	ρ_{rel} (% t.d.)	σ/n^* (% t.d./-)	D (μm)	σ/n^* (μm /-)
P-CIP	1410/10	99.44	0.14/9	1.24	0.19/15
R-CIP	1350/45	99.57	0.07/9	1.25	0.28/15
P-SC	1340/0	99.29	0.25/9	0.54	0.06/20
P-SC	1345/0	99.54	0.07/9	0.68	0.10/20
R-SC	1345/0	99.29	0.11/9	0.89	0.12/20
R-SC	1345/10	99.48	0.18/9	1.18	0.17/20

* : σ is the standard deviation and n is the number of measurements.

of 99.44% t.d. a grain size of 1.24 μm, while the reference sample reached at the density of 99.57% t.d. a grain size of 1.25 μm. There is no significant difference between P-CIP or R-CIP samples including their pore size distribution. For the wet shaping, plasma treated powder (P-SC) exhibited at relative densities > 98% t.d. a markedly smaller grain size than the conventionally stabilized powder (R-SC). The obtained grain sizes at relative density of 99.5% t.d. were 0.68 μm and 1.18 μm for P-SC or R-SC respectively. This improvement in grain size corresponds to a factor of 1.7. The microstructure of samples with the density of 99.5% t.d. is shown in Fig. 8.

4. Discussion

Infrared spectroscopy shows clear evidence of an enhanced surface hydration of plasma treated samples. In addition to that, the adsorption of nitric oxide species is likely to take place on the hydroxylated

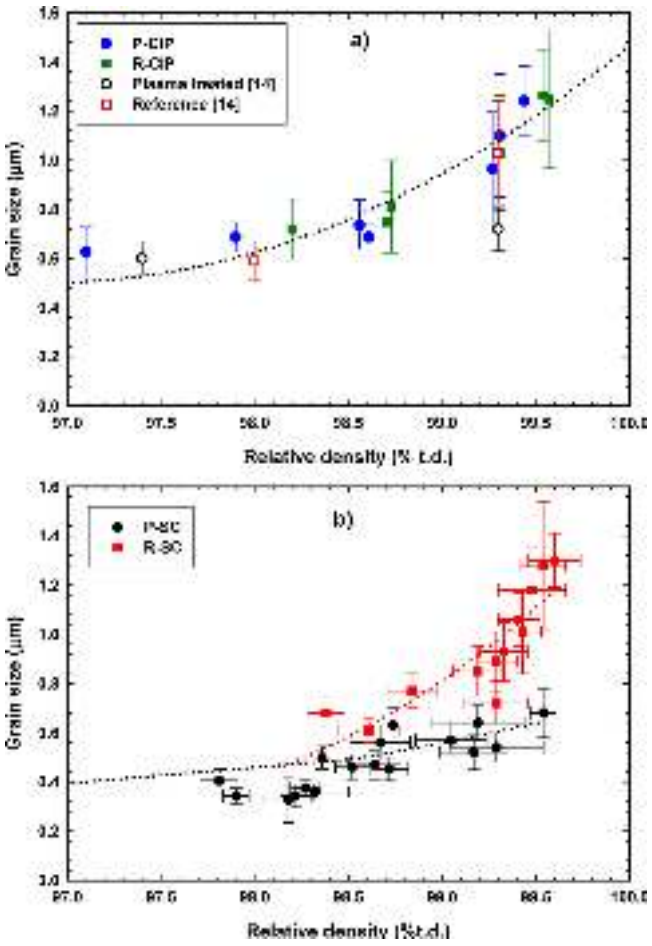

Fig. 7. Sintering trajectory for (a) dry shaping (with data from [14]); (b) wet shaping methods.

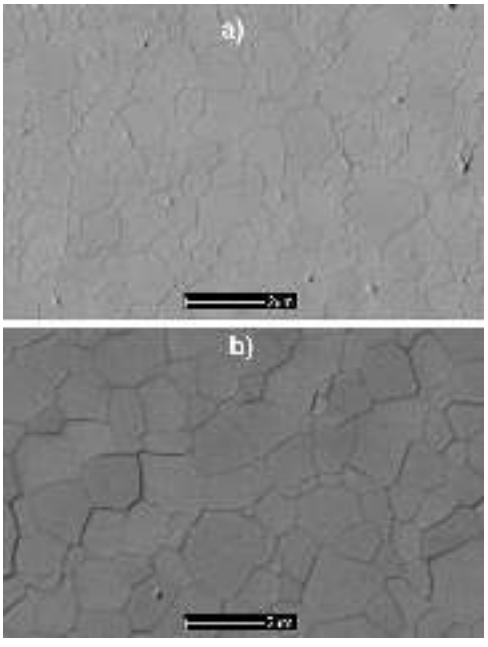

Fig. 8. Microstructure of (a) P-SC sintered at 1345 °C/ 0 min with the density of 99.54% t.d. and (b) R-SC sintered at 1345 °C/ 10 min with the density of 99.48% t.d.

surface. According to [29] gas phase interaction of NO_2 with the alumina surface hydroxyls can lead to the formation of 'sticky' HNO_3 and HONO, which also have strong absorption bands assigned to the O—H vibration at 3600, 3550, and 3450 cm^{-1}. It is therefore reasonable to assume that the increased surface hydration is an outcome of both direct plasma interaction and secondary processes occurring on the surface.

According to the porosimetry (Fig. 5) and dilatometry (Fig. 6a) results the activation of powder had no significant impact on the green body microstructure of dry shaped samples. The results were confirmed by the same sintering trajectory of both (activated and non-activated) dry shaped samples (Fig. 7a). Fig. 6a contains data published previously by Szalay et al. [17]. Although the results of Szalay et al. shows a potential benefit of possible reduction in final grain size even for dry pressed samples, we were not able to replicate such potential. As it can be seen in Fig. 7, Szalay et al obtained at the density of 99.4% t.d. a smaller grain size (0.72 μm) than in our work (1.24 μm); however, the error bars of these two grain size assessments are overlapped. The difference in our two works could therefore be attributed to experimental error, or to subtle changes in technology (i.e. different dry shaping, surface impurities, different TM-DAR batch …).

From the presented data, we can conclude that the DCSBD plasma treatment in ambient air has no significant influence on the sintering of dry shaped Al_2O_3. The dry shaping did not benefit from surface cleaning and/or surface hydroxylation. This is an expected result. The microstructure of a dry shaped green body does not depend on the particle's surface energy, but on the applied mechanical pressure. If there will be some benefit from the surface energy increase, it should be manifested during the sintering. However, the FTIR and Raman results have shown that the plasma treatment is decomposed as early as at temperatures below 500 °C, which is far below the onset of sintering (1050 °C).

On the other hand, in case of the wet shaping methods, the rheological measurements confirmed the improved stability of plasma treated suspensions. The isoelectric point (IEP) for water dispersed alumina powders lays within the pH range of 8–10 [34]. The suspension of plasma treated powder with water possess a pH value of 3, which is in agreement with [17]. In light of our former FTIR analysis, the reduction of pH value would be a natural consequence of HNO_3 release from the plasma treated powders. Moving so distant from the IEP, lower pH is supposed to retain better suspension stability (confirmed by rheological measurements) by a larger amount of surface charge formed on dispersed particles (high positive value of zeta potential). Interestingly enough, plasma treated suspension was even more stable than the suspension R-SC with the commercial stabilizer. One would expect that the water suspension containing both plasma treated powder and dispersant (Darvan C–N) will be even better than the suspension of plasma treated powder alone. However, polyacrylic acid (PAA), the main molecule used in Darvan, is not dissociated at pH 3 and therefore not soluble in water. This leads to the flocculation of the powder despite of the high absorption on an alumina surface [35]. Therefore, we were not able to prepare such a suspension. The other possible combination is the stabilization of the suspensions at pH 3 by commercial acids (without any plasma treatment) which is planned for a future work. However, such initial tests were already done by Szalay et al. with no convincing improvement [17].

Improved suspension stability together with its lower viscosity are the most likely causes of the better green body microstructure. The densification curves of different green bodies confirm the improved microstructure of the P-SC sample shown by faster densification since the full density of the P-SC sample was reached at a ~20 °C lower temperature than the conventionally prepared samples (R-SC). Observed acceleration of the densification dynamics brought a statistically significant reduction of the average grain size by a factor of 1.7 at the density of 99.5% t.d. There is an open question of how much this factor could be affected if a different homogenization procedure would have been used. For a standard slip casting, longer homogenization

times are recommended. It can be speculated that an optimized (although more time consuming) homogenization procedure may deliver an improved green body even for the R-SC samples. Despite this uncertainty, the achieved final P-SC grain size of 0.68 μm at 99.54% t.d. stands up well when compared to other works. For example, with the same powder (TM-DAR) and technology (slip casting followed by conventional pressure-less sintering), Golestani-fard et al. [36] prepared samples with the grain size of 1.5μm (97.8% t.d.), which is much higher than was obtained in this work.

To improve the mechanical and functional properties, many different techniques for the reduction of final grain size were investigated. One of them is the currently popular, though time consuming, 10-hour two-step sintering (TSS) method. For the TM-DAR powder, the TSS studies usually comprise dry shaping followed by the TSS procedure. The achieved grain size varies in different works from 0.5 to 1.4 μm for densities of 98 to 99.4% t.d. respectively [36–40]. The smallest grain size of 0.5 μm [36,38] was obtained at a low density of 98% t.d., which is slightly higher than the results obtained in this work (0.4 μm, see Fig. 7b). At the density of 99.4% t.d., where we obtained the grain size of ~0.6 μm with P-SC powder, Bodisova et al. reached a comparable grain size of 0.65 μm [37], Maca et al. 0.8 μm [39] and Mikoczyova et al. achieved a grain size of over 1 μm [40]. This indicates that our presented approach can bring comparable or even better results than the time consuming TSS method.

The next frequently used techniques for the reduction of final grain size is the decrease of the initial particle size by milling or by buying/preparing the powder with a smaller particle size. For example, Tallon et al. [41] used various commercially available Al_2O_3 powders with particle sizes ranging from 11 to 600 nm. The smallest obtained grain size for the slip casting followed by conventional sintering method was 2.7 μm (44 nm particle size) at a density of 99.5% t.d., which is larger than the grain size obtained in this work.

Other methods for the reduction of final grain size of alumina ceramics comprise advanced shaping methods: e.g. gel-casting [42] or aligning of grains by magnetic field [43]. However, these methods are almost always followed by pressure assisted sintering [44] (to reach transparency) which has not been tested for plasma treated powders yet. Although these advanced techniques were able to obtain an even better final microstructure than in this work, we believe that plasma treatment technology can still offer a timesaving, scalable, chemical-free alternative of preparation of almost dense, fine-grained alumina.

5. Conclusions

Dielectric barrier discharge treatment of submicron Al_2O_3 powder in atmospheric pressure air shows no significant effect on the sintering behavior and final microstructure of dry shaped ceramic samples. The effect of surface modification is already lost below 500 °C and therefore cannot influence the sintering dynamics. However, its effect on the wet chemical processing route is considerable. Stable water suspensions can be created from the plasma activated powder only; without any chemical stabilizer aid. The IR analysis suggests that the effect is related to the increased hydration of Al_2O_3 powder surface associated with the presence of adsorbed nitric oxides. The suspensions exhibit better rheological properties of the slurry and the pore size distribution of a slip casted green body. This contributes to the lower sintering temperature and improved final microstructure for slip casting of activated powder by obtaining the grain size of 0.68 μm at a relative density of 99.54% t.d. In comparison to the slip casting of non-activated powder, this means the decrease of grain size by a factor of 1.7. In this work, DBD plasma treatment can be viewed as a useful and relatively straightforward substitute for some environmentally or technologically problematic dispersion stabilizers. In addition, the proposed adsorption mechanism of the plasma action is determined primarily by plasma-chemical processes occurring in the gas phase, and only secondarily by the powder material composition. It is therefore reasonable to assume that the effect can also be employed for ceramic powders other than Al_2O_3 ceramic powders.

Acknowledgements

This work was supported by the Grant agency of the Czech Republic under grant no. 17-05620S. The CEITEC infrastructure was supported by project LQ1601. The work of the MU team was supported by project CZ.1.05/2.1.00/03.0086 funded by the European Regional Development Fund and project LO1411 (NPU I) funded by the Ministry of Education Youth and Sports of the Czech Republic.

References

[1] P. Bowen, C. Carry, D. Luxembourg, H. Hofmann, Colloidal processing and sintering of nanosized transition aluminas, Powder Technol. 157 (2005) 100–107, https://doi.org/10.1016/j.powtec.2005.05.015.
[2] P. Bowen, C. Carry, From powders to sintered pieces: forming, transformations and sintering of nanostructured ceramic oxides, Powder Technol. 128 (2002) 248–255, https://doi.org/10.1016/S0032-5910(02)00183-3.
[3] F.S. Shiau, T.T. Fang, T.H. Leu, Effects of milling and particle size distribution on the sintering behavior and the evolution of the microstructure in sintering powder compacts, Mater. Chem. Phys. 57 (1998) 33–40, https://doi.org/10.1016/S0254-0584(98)00195-3.
[4] A. Krell, P. Blank, Grain-size dependence of hardness in dense submicrometer alumina, J. Am. Ceram. Soc. 78 (1995) 1118–1120, https://doi.org/10.1111/j.1151-2916.1995.tb08452.x.
[5] D. Drdlik, K. Drdlikova, H. Hadraba, K. Maca, Optical, mechanical and fractographic response of transparent alumina ceramics on erbium doping, J. Eur. Ceram. Soc. 37 (2017) 4265–4270, https://doi.org/10.1016/j.jeurceramsoc.2017.02.043.
[6] S. Filipovic, N. Obradovic, J. Krstic, M. Scepanovic, V. Pavlovic, et al., Structural characterization and electrical properties of sintered magnesium-titanate ceramics, J. Alloys. Compd. 555 (2013) 39–44, https://doi.org/10.1016/j.jallcom.2012.12.040.
[7] J.H. Tsai, I.C. Cheng, C.C. Hsu, J.Z. Chen, DC-pulse atmospheric-pressure plasma jet and dielectric barrier discharge surface treatments on fluorine-doped tin oxide for perovskite solar cell application, J. Phys. D Appl. Phys. 51 (2018), https://doi.org/10.1088/1361-6463/aa9df8.
[8] A. Nadjem, M. Kachi, F. Bekkara, K. Medles, T. Zeghloul, et al., Triboelectrification of granular insulating materials as affected by dielectric barrier discharge (DBD) treatment, J. Electrostat. 86 (2017) 18–23, https://doi.org/10.1016/j.elstat.2016.12.017.
[9] D.L. Shi, S.X. Wang, W.J. van Ooij, L.M. Wang, J.G. Zhao, et al., Uniform deposition of ultrathin polymer films on the surfaces of Al2O3 nanoparticles by a plasma treatment, Appl. Phys. Lett. 78 (2001) 1243–1245, https://doi.org/10.1063/1.1352700.
[10] T. Ishigaki, T. Sato, Y. Moriyoshi, M.I. Boulos, Influence of plasma modification of titanium carbide powder on its sintering properties, J. Mater. Sci. Lett. 14 (1995) 1694–1697, https://doi.org/10.1007/Bf00422678.
[11] L. Lapcik, B. Lapcikova, I. Krasny, I. Kupska, R.W. Greenwood, et al., Effect of low temperature air plasma treatment on wetting and flow properties of kaolinite powders, Plasma Chem Plasma P. 32 (2012) 845–858, https://doi.org/10.1007/s11090-012-9374-z.
[12] A. Solis-Gomez, M.G. Neira-Velazquez, J. Morales, M.A. Sanchez-Castillo, E. Perez, Improving stability of TiO2 particles in water by RF-plasma polymerization of poly (acrylic acid) on the particle surface, Colloids Surf. A Physicochem. Eng. Asp. 451 (2014) 66–74, https://doi.org/10.1016/j.colsurfa.2014.03.021.
[13] R. Brandenburg, Dielectric barrier discharges: progress on plasma sources and on the understanding of regimes and single filaments, Plasma Sources Sci. Technol. 26 (2017), https://doi.org/10.1088/1361-6595/aa6426.
[14] V. Fiore, G. Di Bella, T. Scalici, A. Valenza, Effect of plasma treatment on mechanical and thermal properties of marble Powder/Epoxy composites, Adv. Manuf. Polym. Compos. Sci. 39 (2018) 309–317, https://doi.org/10.1002/pc.23937.
[15] M.G. Trulli, N. Claes, J. Pype, S. Bals, K. Baert, et al., Deposition of aminosilane coatings on porous Al2O3 microspheres by means of dielectric barrier discharges, Plasma Process. Polym. 14 (2017), https://doi.org/10.1002/ppap.201600211.
[16] V.O. Kollath, S. Put, S. Mullens, A. Vanhulsel, J. Luyten, et al., Atmospheric pressure plasma as an activation step for improving protein adsorption on hydroxyapatite powder, Plasma Process. Polym. 12 (2015) 594–601, https://doi.org/10.1002/ppap.201400092.
[17] Z. Szalay, K. Bodisova, H. Palkova, P. Svancarek, P. Durina, et al., Atmospheric pressure air plasma treated alumina powder for ceramic sintering, Ceram. Int. 40 (2014) https://doi.org/12737-43.
[18] D. Drdlik, T. Moravek, J. Rahel, M. Stupavska, J. Cihlar, et al., Electrophoretic deposition of plasma activated sub-micron alumina powder, Ceram. Int. 44 (2018) 9789–9793, https://doi.org/10.1016/j.ceramint.2018.02.215.
[19] A. Aimable, P. Bowen, Nanopowder metrology and nanoparticle size measurement - Towards the development and testing of protocols, Process. Appl. Ceram. 4 (2010) 157–166, https://doi.org/10.2298/PAC1003157A.
[20] T. Moravek, P.F. Ambrico, M. Ambrico, L. Schiavulli, J. Rahel, Parametric study of plasma-mediated thermoluminescence produced by Al2O3 sub-micron powders, J.

Phys. D Appl. Phys. 50 (2017), https://doi.org/10.1016/10.1088/1361-6463/aa82e1.
[21] K. Maca, V. Pouchly, A.R. Boccaccini, Sintering densification curve - a practical approach for its construction from dilatometric shrinkage data, Sci. Sinter. 40 (2008) 117–122, https://doi.org/10.2298/SOS0802117M.
[22] J.C. Wurst, J.A. Nelson, Linear intercept technique for measuring grain-size in 2-Phase polycrystalline ceramics, J. Am. Ceram. Soc. 55 (1972) 109, https://doi.org/10.1111/j.1151-2916.1972.tb11224.x.
[23] R.L. Frost, D.L. Wain, W.N. Martens, B.J. Reddy, Vibrational spectroscopy of selected minerals of the rosasite group, Spectrochim. Acta A 66 (2007) 1068–1074, https://doi.org/10.1016/j.saa.2006.04.042.
[24] T. Shirai, J.W. Li, K. Matsumaru, C. Ishizaki, K. Ishizaki, Surface hydration states of commercial high purity alpha-Al2O3 powders evaluated by temperature programmed desorption mass spectrometry and diffuse reflectance infrared Fourier transform spectroscopy, Adsorp. Sci. Technol. 6 (2005) 123–128, https://doi.org/10.1016/j.stam.2004.11.003.
[25] C.M. Koretsky, D.A. Sverjensky, J.W. Salisbury, D.M. DAria, Detection of surface hydroxyl species on quartz, gamma-alumina, and feldspars using diffuse reflectance infrared spectroscopy, Geochim. Cosmochim. Acta 61 (1997) 2193–2210, https://doi.org/10.1016/S0016-7037(97)00056-2.
[26] M. Digne, P. Sautet, P. Raybaud, P. Euzen, H. Toulhoat, Hydroxyl groups on gamma-alumina surfaces: a DFT study, J. Catal. 211 (2002) 1–5, https://doi.org/10.1006/jcat.2002.3741.
[27] L.H. Little, Infrared Spectra of Adsobed Species, Academic Press Inc., London, 1966.
[28] H.H. Ingelsten, A. Hellman, H. Kannisto, H. Gronbeck, Experimental and theoretical characterization of NOx species on Ag/alpha-Al2O3, J. Mol. Catal. A-Chem. 314 (2009) 102–109, https://doi.org/10.1016/j.molcata.2009.08.022.
[29] C. Borensen, U. Kirchner, V. Scheer, R. Vogt, R. Zellner, Mechanism and kinetics of the reactions of NO2 or HNO3 with alumina as a mineral dust model compound, J. Phys. Chem. A 104 (2000) 5036–5045, https://doi.org/10.1021/jp994170d.
[30] J. Cech, A. Brablec, M. Cernak, N. Puac, N. Selakovic, et al., Mass spectrometry of diffuse coplanar surface barrier discharge: influence of discharge frequency and oxygen content in N-2/O-2 mixture, Eur. Phys. J. D 71 (2017), https://doi.org/10.1140/epjd/e2016-70607-5.
[31] S. Hosseini, A.A. Niaei, D. Salari, Production of γ-Al2O3 from Kaolin, Open J. Phys. Chem. 1 (2011) 23–27 https://doi.org/0.4236/ojpc.2011.12004.
[32] D. Deng, V. Boyko, S.M. Pancera, N. Nestle, T. Tadros, Rheology investigations on the influence of addition sodium polyacrylate to calcium carbonate suspensions, Colloids Surf. A Physicochem. Eng. Asp. 372 (2010) 9–14, https://doi.org/10.1016/j.colsurfa.2010.09.001.
[33] M. Stuer, P. Bowen, Yield stress modelling of doped alumina suspensions for applications in freeze granulation: towards dry pressed transparent ceramics, Adv. Appl. Ceram. 111 (2012) 254–261, https://doi.org/10.1179/1743676111y.0000000061.
[34] G.V. Franks, Y. Gan, Charging behavior at the alumina-water interface and implications for ceramic processing, J. Am. Ceram. Soc. 90 (2007) 3373–3388, https://doi.org/10.1111/j.1551-2916.2007.02013.x.
[35] Z.C. Chen, T.A. Ring, J. Lemaitre, Stabilization and processing of aqueous Batio3 suspension with polyacrylic-acid, J. Am. Ceram. Soc. 75 (1992) 3201–3208, https://doi.org/10.1111/j.1151-2916.1992.tb04412.x.
[36] F. Golestani-fard, M. Mazaheri, M. Aminzare, T. Ebadzadeh, Microstructural evolution of a commercial ultrafine alumina powder densified by different methods, J. Eur. Ceram. Soc. 31 (2011) 2593–2599, https://doi.org/10.1016/j.jeurceramsoc.2010.12.022.
[37] K. Bodisova, D. Galusek, P. Svancarek, V. Pouchly, K. Maca, Grain growth suppression in alumina via doping and two-step sintering, Ceram. Int. 41 (2015) 11975–11983, https://doi.org/10.1016/j.ceramint.2015.05.162.
[38] Z.R. Hesabi, A. Haghighatzadeh, M. Mazaheri, D. Galusek, S.K. Sadrnezhaad, Suppression of grain growth in sub-micrometer alumina via two-step sintering method, J. Eur. Ceram. Soc. 29 (2009) 1371–1377, https://doi.org/10.1016/j.jeurceramsoc.2008.08.027.
[39] K. Maca, V. Pouchly, P. Zalud, Two-Step Sintering of oxide ceramics with various crystal structures, J. Eur. Ceram. Soc. 30 (2010) 583–589, https://doi.org/10.1016/j.jeurceramsoc.2009.06.008.
[40] M. Mikoczyová, D. Galusek, Influence of forming method and sintering process on densifi cation and fi nal microstructure of submicrometre alumina ceramics, Proc. Appl. Ceram. 2 (2008) 13–17, https://doi.org/10.2298/PAC0801013M.
[41] C. Tallon, M. Limacher, G.V. Franks, Effect of particle size on the shaping of ceramics by slip casting, J. Eur. Ceram. Soc. 30 (2010) 2819–2826, https://doi.org/10.1016/j.jeurceramsoc.2010.03.019.
[42] D. Nuzhnyy, J. Petzelt, F. Borodavka, P. Vanek, D. Simek, et al., Efective infrared reflectivity and dielectric function of polycrystalline alumina ceramics, Phys. Status Solidi B 254 (2017), https://doi.org/10.1002/pssb.201600607.
[43] T. Ashikaga, B.N. Kim, H. Kiyono, T.S. Suzuki, Effect of crystallographic orientation on transparency of alumina prepared using magnetic alignment and SPS, J. Eur. Ceram. Soc. 38 (2018) 2735–2741, https://doi.org/10.1016/j.jeurceramsoc.2018.02.006.
[44] B.N. Kim, K. Hiraga, S. Grasso, K. Morita, H. Yoshida, et al., High-pressure spark plasma sintering of MgO-doped transparent alumina, J. Ceram. Soc. Jpn. 120 (2012) 116–118, https://doi.org/10.2109/jcersj2.120.116.